Materials Matter
https://www.sciltp.com/journals/mm

Review

Crystallographic Symmetry—Governed Oxygen-Defect Chemistry in Perovskite Oxides for Electrocatalytic Water Splitting

Linai Zhou [1,†], Jiamu Feng [1,†], Kean Zhu [1,†], Lingfeng Gao [1,*], Weilin Xu [1], Hui Wang [2,*] and Jun Wan [1,*]

1 State Key Laboratory of New Textile Materials and Advanced Processing, Hubei Key Laboratory of Biomass Fibers and Eco-Dyeing & Finishing, Wuhan Textile University, Wuhan 430200, China
2 School of Materials Science and Engineering, Nanyang Technological University, 50 Nanyang Avenue, Singapore 639798, Singapore
* Correspondence: lfgao@wtu.edu.cn (L.G.); huiwang04@outlook.com (H.W.); wanj@wtu.edu.cn (J.W.)
† These authors contributed equally to this work.

How To Cite: Zhou, L.; Feng, J.; Zhu, K.; et al. Crystallographic Symmetry—Governed Oxygen-Defect Chemistry in Perovskite Oxides for Electrocatalytic Water Splitting. *Materials Matter* **2026**, *1*(1), 1.

Received: 11 December 2025
Revised: 30 December 2025
Accepted: 8 January 2026
Published: 20 January 2026

Abstract: Electrocatalytic water splitting is a key technology for sustainable hydrogen production, yet the sluggish kinetics of the oxygen evolution reaction (OER) and hydrogen evolution reaction (HER) hinder its efficiency. Perovskite oxides (ABO_3) have emerged as promising catalysts owing to their tunable crystal structures, chemical stability, and abundant active sites. While the crystal phase of perovskite oxides is crucial in determining catalytic activity, charge transport, and reaction energetics, the complex interplay between phase transitions, lattice distortions, oxygen vacancy distribution, and electronic structure remains underexplored. This review systematically examines the structural variations across six primary crystal phases of perovskite oxides, including cubic, hexagonal, tetragonal, orthorhombic, rhombohedral, monoclinic, and their effects on catalytic performance. It explores how lattice symmetry, oxygen vacancy distribution, and electronic properties influence reaction pathways and catalytic efficiency in water splitting. Additionally, the review discusses the role of phase transitions, coordination environment adjustments, and defect engineering in optimizing electrocatalytic behavior. Perovskite oxides are categorized by their A-site and B-site metal ion compositions, providing a comprehensive analysis of how these structural variations influence electrocatalytic mechanisms. The insights gained from this review offer crucial guidance for advancing the design of high-performance perovskite oxide catalysts for sustainable water electrolysis.

Keywords: perovskite oxides; crystal phase engineering; cation modulation; electronic orbital configuration; electrocatalytic water splitting

1. Introduction

Electrocatalytic water splitting is a promising method for sustainable hydrogen production, but its efficiency is constrained by the sluggish kinetics of both the oxygen evolution reaction (OER) and hydrogen evolution reaction (HER) [1,2]. The OER involves a complex four-electron transfer and typically requires high overpotentials, while HER is limited by water dissociation, especially in alkaline media, reducing overall reaction rates [3–5]. Therefore, developing highly active, stable, and earth-abundant catalysts for both reactions is crucial to improving the economic feasibility of water electrolysis [6,7]. Perovskite oxides (ABO_3) are regarded as promising catalysts for electrocatalytic water splitting due to their tunable crystal structures, versatile redox properties, and

Copyright: © 2026 by the authors. This is an open access article under the terms and conditions of the Creative Commons Attribution (CC BY) license (https://creativecommons.org/licenses/by/4.0/).
Publisher's Note: Scilight stays neutral with regard to jurisdictional claims in published maps and institutional affiliations.

excellent electrochemical stability [8–10]. The A-site cations influence lattice distortions, charge compensation, and oxygen vacancy formation, which in turn affect surface electronic properties and interfacial stability [11–13]. The B-site transition metals' d-orbital occupancy dictates redox activity and reaction selectivity [14–16]. Furthermore, perovskite oxides can be further optimized through B-site valence tuning, A/B-site co-doping, defect engineering, and heterostructure design [17–19]. Although studies have explored the role of cationic composition, oxygen vacancy distribution, and electronic structure in catalytic performance, the relationship between crystal phase and catalytic activity remains underexplored [20–22]. Variations in crystallinity directly impact electronic structures, oxygen species adsorption, and charge transfer pathways, yet their contributions to performance are not fully understood [23–25]. Additionally, structural evolution, phase stability, and surface reconstruction during water splitting have yet to be fully addressed, particularly in relation to phase transitions under operational conditions and their effects on long-term catalytic stability [26–28]. Thus, understanding the correlation between crystal phase and catalytic behavior is essential for optimizing perovskite oxides in water electrolysis [29–31].

Perovskite oxides exhibit distinctive catalytic behaviors based on their unique crystal structures, which directly influence their electrocatalytic performance. Analyzing perovskite oxides through the six primary crystal structures (cubic, hexagonal, tetragonal, orthorhombic, rhombohedral, and monoclinic) reveals significant differences in lattice symmetry, electronic structure, and oxygen vacancy characteristics. These structural variations govern the material's reactivity and stability during electrocatalytic water splitting. Cubic perovskites, characterized by high symmetry, typically exhibit uniform electronic distribution and low lattice energy, which facilitates efficient electron and ion transport while minimizing energy dissipation, thereby enhancing reaction rates and catalytic stability [32–34]. In contrast, hexagonal and tetragonal perovskites, with their more pronounced lattice distortions, generate additional oxygen vacancies and defect sites at the surface [35–37]. These active sites promote the adsorption, migration, and desorption of oxygen species, thus significantly improving the OER activity and selectivity [38]. Orthorhombic and rhombohedral perovskites, with varying oxidation states at the B-site metal ions, induce local electronic reorganization, optimizing the reaction pathways for oxygen species, which further enhances catalytic performance [39–41]. However, while existing studies have demonstrated the potential of different crystal phases in perovskite oxides for electrocatalytic water splitting, the underlying mechanisms that govern the relationship between crystal structure and catalytic performance remain underexplored. Most current research focuses on the impact of crystal phases on surface reactivity and charge transfer; however, the role of crystal structure in modulating oxygen vacancy distribution, electron transport pathways, and the adsorption-desorption processes of oxygen species is not yet fully understood [42–44]. Specifically, the influence of lattice distortion in various crystal phases on catalytic efficiency and how these phases modulate the reactions at the catalyst surface to enhance water splitting efficiency remains inadequately addressed. Furthermore, perovskite oxides may undergo phase transitions during electrochemical water splitting, which significantly affects their long-term stability and catalytic activity. Therefore, it is essential to conduct more comprehensive studies to understand the crystal phase-dependent structural-performance relationships, revealing the mechanisms by which crystal phase transitions impact catalytic efficiency and stability. Such insights will provide critical guidance for the design and optimization of perovskite oxides in electrocatalytic applications.

This review provides a comprehensive analysis of the influence of crystal phase structures on the electrocatalytic performance of perovskite oxides for water splitting. Perovskite oxides are systematically categorized into six distinct crystal phases: cubic, hexagonal, tetragonal, orthorhombic, rhombohedral, and monoclinic. The unique structural features of these phases, including lattice symmetry, oxygen vacancy distribution, and electronic properties, are analyzed in relation to their catalytic behavior (Figure 1). In contrast to previous reviews that focus on single-phase systems or specific material types, this review emphasizes the interaction between crystal phase, electronic structure, and catalytic performance, highlighting their effects on reaction kinetics, intermediate adsorption, and charge transport. Furthermore, the role of phase transitions, coordination environment modifications, and defects in optimizing electrocatalytic activity is explored, stressing the importance of phase-engineering strategies for enhancing catalytic efficiency. This review categorizes perovskite oxides based on the specific types of A-site and B-site metal ions used, offering an in-depth analysis of the influence of these classifications on reaction pathways and mechanisms in electrocatalytic water splitting, drawing from current research cases. The review primarily focuses on structural perspectives, providing a systematic framework for designing high-performance perovskite oxide catalysts for sustainable water electrolysis and outlining key research directions in this field.

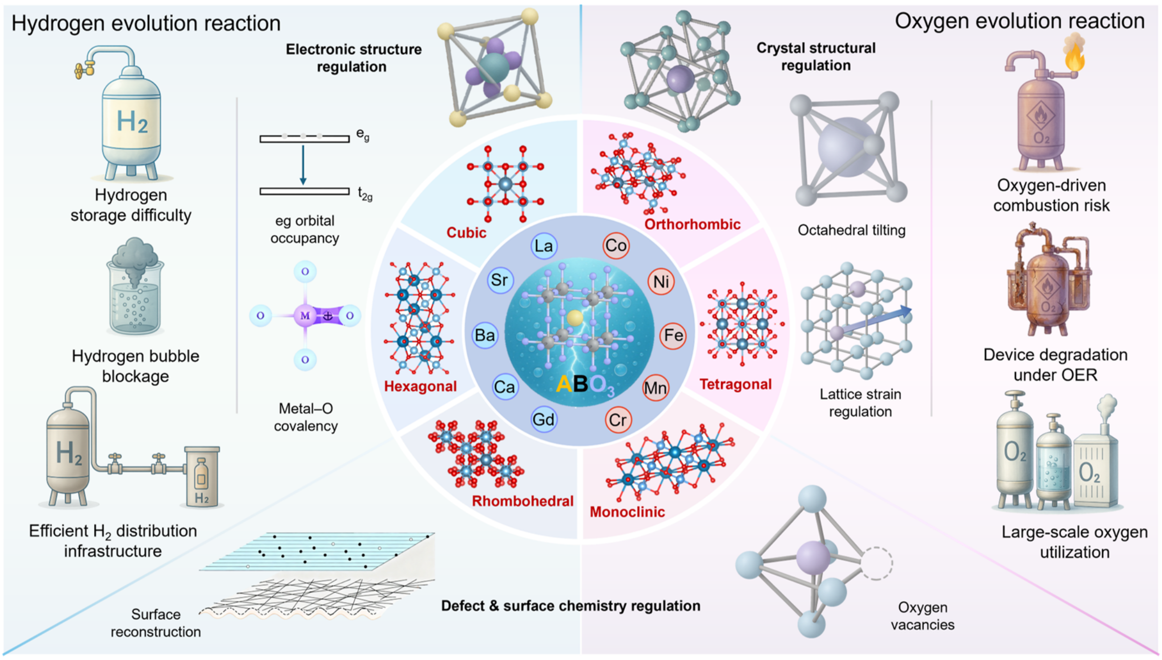

Figure 1. Schematic representation of structural and phase-dependent characteristics of perovskite oxides in electrocatalytic water splitting.

2. Fundamental Principles and Structural Characteristics of Perovskite Oxides for Electrocatalytic Water Splitting

Perovskite oxides play a critical role in electrocatalytic water splitting due to their distinctive electronic structures, chemical stability, and abundant active sites, making them ideal candidates for efficient catalysts. The crystalline phases of perovskite oxides not only govern charge transport, oxygen vacancy formation, and interfacial reaction kinetics but also significantly influence their long-term stability and catalytic efficiency [45,46]. Therefore, gaining a deep understanding of the fundamental catalytic mechanisms and structural characteristics of perovskite oxides is crucial for enhancing their catalytic performance [47,48]. This section first explores the fundamental catalytic mechanisms and advantages of perovskite oxides in water splitting, followed by a systematic examination of their six major crystalline phases. Finally, a comprehensive review and analysis of existing studies will provide insights into the structure-performance relationships, offering valuable guidance for the rational design of perovskite oxide electrocatalysts.

2.1. Fundamental Electrocatalytic Mechanisms and the Advantages of Perovskite Oxides for Water Splitting

Perovskite oxides (ABO_3) exhibit exceptional advantages in electrocatalytic water splitting due to their unique crystal structure, tunable electronic properties, and precise control over defects and surface reconstruction during the catalytic process (Figure 2) [49–51]. The inherent stability and flexibility of the perovskite crystal structure enable it to maintain chemical robustness under high potential conditions, which is critical for OER. The A-site metal (such as rare earth metals like La and Pr) enhances the catalyst’s performance by modulating the electron distribution in the crystal lattice, improving its thermal stability [52–54]. In contrast, the B-site metal (such as Fe, Ni, and Co) plays a pivotal role in catalytic activity, particularly in OER, where transition metals at the B-site facilitate the adsorption, activation, and cleavage of O–O bonds due to their abundant d-electron states. Studies have shown that the oxidation states of B-site metals, particularly higher oxidation states such as Fe^{3+} and Ni^{3+}, significantly influence the catalytic activity by promoting the oxygen evolution process and reducing the required overpotentials [55–57].

Another major advantage of perovskite oxides lies in their ability to modulate defects. Oxygen vacancies and lattice distortions not only improve the material’s conductivity but also substantially enhance catalytic activity [58]. The introduction of oxygen vacancies is typically achieved by adjusting the oxidation states of B-site metals, and these vacancies act as active sites to facilitate the adsorption and transformation of reaction intermediates, thereby improving catalytic efficiency [58–60]. Research indicates that oxygen vacancies can effectively promote the adsorption of reactants and the conversion of intermediates, lowering the overpotentials in the OER process. Meanwhile, lattice distortions in perovskite oxides help modify their surface electronic structure, further optimizing catalytic performance [61]. Moderate lattice distortions expose more active sites on the catalyst surface, thus increasing the effective area for catalytic reactions and enhancing activity in water splitting [62,63].

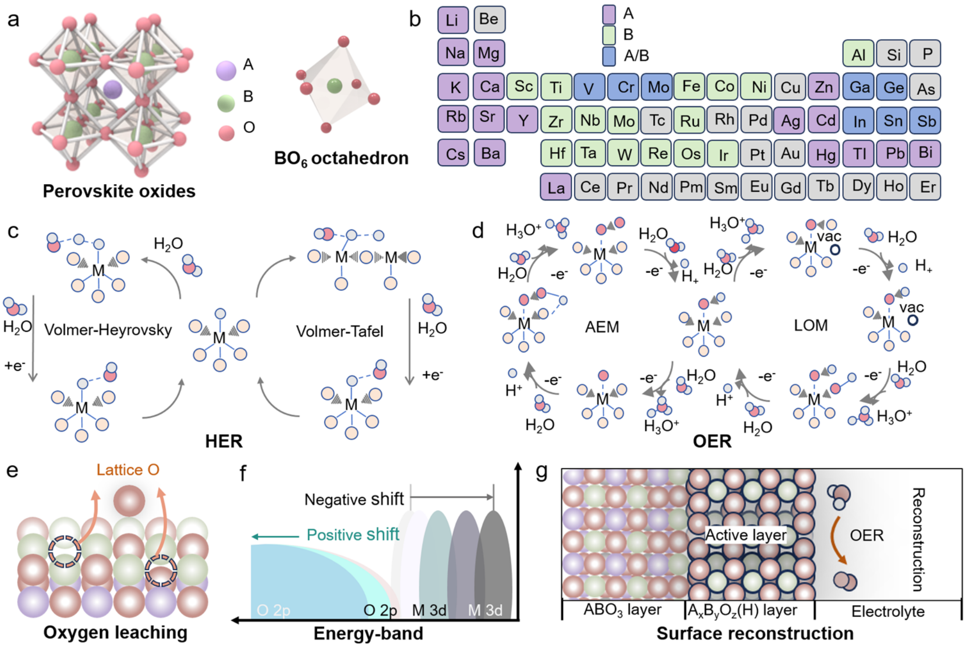

Figure 2. Fundamental electrocatalytic mechanisms and structural advantages of perovskite oxides for water splitting. (**a**) Structure of perovskite oxides, showing A-site cations (purple), B-site cations (green), and oxygen anions (red), together with the BO_6 octahedral unit; (**b**) Elemental map of possible A- and B-site cations in perovskite oxides; (**c**) HER pathways, including Volmer–Heyrovsky and Volmer–Tafel mechanisms; (**d**) Adsorption and reaction pathways during OER, illustrating AEM and LOM routes; (**e**) Oxygen-leaching process and its influence on O-2p and metal-3d orbital interactions; (**f**) Energy-band shifts associated with oxygen leaching, highlighting positive and negative level shifts; (**g**) Surface reconstruction under OER conditions, showing the evolution from the ABO_3 lattice to the active reconstructed layer.

Surface reconstruction during catalytic reactions is another key factor contributing to the superior performance of perovskite oxides in electrocatalytic water splitting [64–66]. Under high potential conditions, particularly during the OER, the surface of perovskite oxides undergoes dynamic reconstruction, where A-site metal ions and oxygen ions migrate, leading to structural changes on the catalyst surface [67–69]. This process not only exposes more active sites but also improves the catalyst's stability during prolonged reactions [17,70]. Surface reconstruction, facilitated by A-site metal migration or oxygen ion exchange, optimizes reaction pathways, reduces energy barriers, and enhances overall catalytic efficiency in water splitting [71–73].

Although the catalytically active surface of perovskite oxides under OER conditions generally evolves into an amorphous or poorly crystalline oxyhydroxide layer, the initial bulk crystal phase and lattice symmetry critically govern the reconstruction pathway and its dynamic features. Different crystallographic phases impose distinct metal oxygen bond strengths, lattice strain distributions, and oxygen vacancy energetics, which collectively determine the kinetics of surface reconstruction, the thickness of the reconstructed layer, and the extent of bulk participation in the transformation. Low symmetry or strongly distorted perovskite phases, characterized by pronounced octahedral tilting and weaker average M-O bonds, typically exhibit faster reconstruction kinetics and form thicker oxyhydroxide layers due to lower energetic barriers for bond breaking and oxygen exchange. Beyond kinetics, the initial crystal phase also influences the reversibility and long term stability of the reconstructed surface. Perovskites with moderate symmetry reduction and controlled defect concentrations may undergo quasi reversible surface transformations, where the oxyhydroxide layer forms under anodic polarization and partially reverts upon potential relaxation, preserving bulk structural integrity. In contrast, excessively distorted or defect rich phases are prone to irreversible reconstruction, leading to deep lattice amorphization, cation leaching, and gradual performance degradation under prolonged operation. These insights highlight that surface reconstruction is not merely a superficial phenomenon, but a bulk surface coupled process, in which the initial crystallographic symmetry directly links the operando active structure to long term catalytic stability.

Finally, the electronic structure of perovskite oxides plays a crucial role in their electrocatalytic water splitting performance [74–76]. The conductivity of perovskite oxides is influenced by the oxidation state of the B-site metals and the density of d-electrons in the lattice [77,78]. By selecting appropriate metal ions and tuning their redox behavior, the electronic structure can be optimized to improve electrocatalytic efficiency. The electronic structure of perovskite oxides can be further manipulated through careful selection of A- and B-site metals, enabling enhanced electron transport and material exchange processes during catalytic reactions [79,80]. Thus, by tuning the electronic structure, defect characteristics, and surface reconstruction properties of perovskite oxides, their performance in water splitting reactions can be significantly enhanced.

2.2. Structural Classification of Perovskite Oxides

Structural descriptors such as “lattice distortion” and “local distortion” are employed in a crystallographic context to describe specific deviations from ideal perovskite symmetry, including octahedral tilting, variations in bond angles and bond lengths, and defect induced local relaxation. Beyond merely characterizing geometric deviations, these descriptors provide quantitative insight into the spatial distribution of distortions across different length scales, from local coordination environments to long range lattice arrangements. Their precise definitions ensure consistency with conventional crystallographic terminology and allow for systematic comparison across different perovskite compositions and structural variants. Moreover, understanding these distortions is critical for linking structural features to functional properties, as variations in lattice geometry can directly influence electronic structure, ion migration pathways, defect formation energetics, and ultimately the physical and chemical behavior of perovskite oxides in applications such as catalysis, energy conversion, and electronic devices. By providing a rigorous framework for describing and analyzing structural deviations, these descriptors enable a comprehensive and mechanistic understanding of the complex interplay between local structure and material functionality.

The crystal structures of perovskite oxides are diverse, with the six major crystal phases including cubic, hexagonal, tetragonal, orthorhombic, rhombohedral, and monoclinic (Figure 3). These phases differ in terms of their lattice symmetry, atomic arrangement, and the interactions between neighboring atoms, all of which directly influence the pathways and efficiency of electrocatalytic reactions [81–83]. Perovskite oxides with different crystal phases exhibit distinct electronic structures, oxygen vacancy distributions, and catalytic active sites, leading to significant variations in their catalytic performance during water splitting [84–86]. Therefore, investigating the structural characteristics of these phases and their relationship with electrocatalytic performance provides crucial theoretical support for the design of perovskite oxide catalysts.

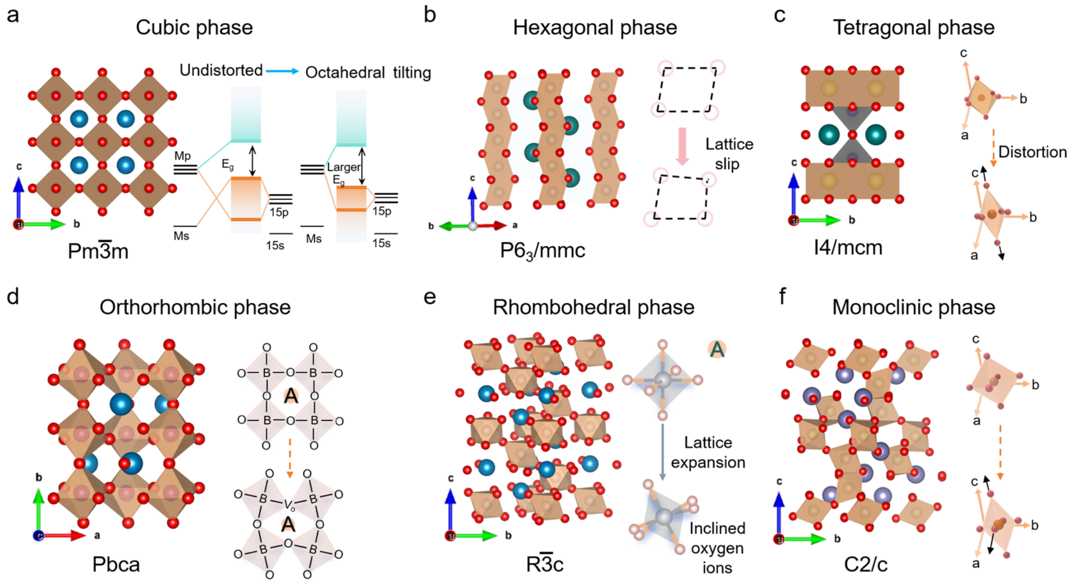

Figure 3. Crystalline phase classification and structural features of perovskite oxides. (**a**) Cubic phase ($Pm\bar{3}m$), featuring highly symmetric corner-sharing BO_6 octahedra with minimal lattice distortion; (**b**) Hexagonal phase ($P6_3/mmc$), composed of face-sharing octahedral chains that induce anisotropic stacking and basal-plane lattice slip; (**c**)Tetragonal phase(I4/mcm),characterized by octahedral distortion with axial elongation/compression and reduced symmetry along the c-axis; (**d**) Orthorhombic phase (Pbca), showing cooperative octahedral rotations and A-site displacement that alter B–O–B connectivity; (**e**) Rhombohedral phase ($R\bar{3}c$), with tilted BO_6 octahedra and lattice expansion along the rhombohedral direction, accompanied by inclined oxygen ions; (**f**) Monoclinic phase (C2/c), exhibiting strong octahedral tilting and bond-angle deviations that generate significant lattice distortion and low-symmetry coordination.

2.2.1. Cubic Phase

The cubic phase perovskite oxides are among the most common and symmetric crystal phases, characterized by high lattice symmetry, typically belonging to the space group $Pm\overline{3}m$ [87,88]. In this structure, A-site cations are positioned at the center of the cubic unit cell, while B-site cations occupy the centers of oxygen octahedra, and oxygen anions are located at the vertices of the cube [89,90]. This arrangement results in a highly uniform lattice environment. In such a symmetric structure, the coordination environment of both A- and B-site cations is equivalent, with A-site cations interacting with B-site cations via oxygen anions, forming a stable three-dimensional network [91–93]. The high symmetry of this arrangement imparts significant lattice stability and structural integrity to cubic perovskite oxides [94]. Another notable feature of the cubic phase is its relatively low lattice energy, which helps reduce energy losses during electrocatalytic processes and facilitates efficient charge and ion transport [95–97]. The low lattice energy leads to weaker interactions between A-site and B-site cations, providing flexibility for structural changes under external stimuli, such as the generation and migration of oxygen vacancies [98]. Additionally, the oxygen vacancy distribution in the cubic phase is relatively regular, and the formation and migration of oxygen vacancies can influence the kinetics of redox reactions [99]. Thus, cubic perovskite oxides maintain structural stability while allowing for the optimization of catalytic activity through the tuning of oxygen vacancies [100–102]. Regarding electronic structure, cubic perovskite oxides generally exhibit high conductivity and low electronic band gaps, making them effective in charge transfer processes [103]. The migration of electrons mainly depends on the presence and distribution of oxygen vacancies, which often leads to localized electron accumulation, thereby promoting the adsorption of reactants and electron transfer. Due to the high symmetry of the structure, the surface electron density in cubic perovskite oxides is relatively uniform, which helps enhance the uniformity and stability of catalytic reactions [104]. By appropriately tuning the A-site and B-site elements, the electronic structure of cubic perovskite oxides can be further optimized to achieve higher electrocatalytic performance. In conclusion, the structural characteristics of cubic perovskite oxides, including their high symmetry, low lattice energy, stable oxygen vacancy distribution, and optimized electronic structure, collectively contribute to their strong potential in electrocatalytic reactions [105,106].

2.2.2. Hexagonal Phase

The hexagonal perovskite oxide exhibits distinct hexagonal symmetry, typically belonging to the space group $P6_3/mmc$ [107]. In this structure, the coordination environments of the A-site and B-site cations are notably different. The A-site cations are positioned at the center of the hexagonal unit cell, while the B-site cations are located at the center of octahedral oxygen coordination, forming nearly octahedral coordination [108]. Unlike the high symmetry of the cubic phase, the hexagonal phase features a layered structure, with the A-site and B-site cations located in separate layers [109,110]. This arrangement results in relatively weak interlayer interactions along the c-axis, allowing for potential lattice slip or rearrangement, which contributes to its tunable properties under specific conditions. In the hexagonal phase, oxygen anions form octahedra around the B-site cations, and these octahedra are interconnected by sharing oxygen atoms, creating a three-dimensional network [111–113]. The stacking along the c-axis is asymmetrical, leading to lattice distortion and significant anisotropy in lattice density along different directions. This asymmetrical stacking structure induces lattice strain and notably affects the formation and distribution of oxygen vacancies, which in turn influences the stability and catalytic activity. Oxygen vacancies typically arise at sites where oxygen ions are mismatched, and these defect sites not only facilitate the transport of electrons and ions but also serve as active sites in catalytic processes [114–116]. Furthermore, the electronic structure of the hexagonal phase is closely related to its lattice characteristics. Due to its layered structure and lattice inhomogeneity, the rate of electron migration between different crystal planes exhibits directional anisotropy. Compared to the cubic phase, the electronic density distribution in the hexagonal perovskite is highly anisotropic, causing its electrical properties to vary depending on the direction. The electronic configuration of the A-site and B-site cations, along with the coordination of the oxygen anions, further modulates its conductivity, bandgap, and conduction mechanisms. Overall, the asymmetrical layered stacking, distribution of oxygen vacancies, and anisotropic electronic structure of the hexagonal perovskite confer unique physical properties and potential tunability, providing advantages for specific applications.

2.2.3. Tetragonal Phase

Tetragonal-phase perovskite oxides typically belong to the $I4/mcm$ space group, exhibiting relatively high symmetry. However, in contrast to the cubic phase, significant distortions along the c-axis are present in their lattice structure. These distortions arise from variations in the coordination environment of the B-site metal ions, resulting in the elongation or compression of the oxygen octahedra, which alters the coordination geometry and the coordination number between the oxygen ions and B-site metal ions [117]. Specifically, in the tetragonal phase, the oxygen octahedra along the c-axis are of different sizes, creating anisotropy in the crystal lattice and leading to directional differences throughout the material. In this phase, the A-site ions are located in relatively larger voids, interacting weakly with the surrounding oxygen ions [118]. These ions are more susceptible to displacement or distortion due to external factors such as temperature and stress. The asymmetry in the structure makes the tetragonal phase more stable at lower temperatures but also more sensitive to structural changes induced by lattice stress [119–121]. The formation of oxygen vacancies in the tetragonal phase is significantly influenced by these lattice distortions, and the oxygen ion migration exhibits anisotropic behavior, which further intensifies the impact of lattice stress on structural stability. Additionally, the electronic structure and ionic conductivity of tetragonal-phase perovskites are affected by lattice distortions. Due to the deformation of the oxygen octahedra, the tetragonal phase shows high anisotropy in its conductivity, with electron migration differing in efficiency across various directions. This non-isotropic structure imparts strong adaptability and stability under conditions of varying stress and temperature [122]. Although its performance is influenced by lattice changes, the tetragonal-phase perovskite still holds significant potential, particularly in catalytic reactions, where the dynamic behavior of oxygen vacancies plays a crucial role, despite the structural variations.

2.2.4. Orthorhombic Phase

The orthorhombic perovskite oxides crystallize in the Pbca space group, which is characterized by relatively low symmetry compared to other perovskite phases. The lattice consists of oxygen octahedra that undergo elongation or compression along three distinct directions, resulting in unequal lattice constants along each axis. Unlike the cubic and hexagonal phases, the internal arrangement in the orthorhombic phase is more irregular. The A-site cations typically reside in larger octahedral voids, but due to the crystal distortion, these cations shift significantly compared to other phases [123]. This shift alters the interactions between A-site cations and oxygen ions, affecting lattice distortion and the formation of oxygen vacancies. The lattice distortion in the orthorhombic phase is reflected in the varying sizes and shapes of the oxygen octahedra, leading to non-uniform oxygen ion arrangements and modifying the interactions between metal ions and oxygen ions. In contrast to perovskites with higher symmetry, the orthorhombic lattice exhibits stronger anisotropy, with notable differences in the distances between oxygen ions [124,125]. This heterogeneity in oxygen ion spacing complicates the distribution of oxygen vacancies and the coordination environment of metal ions. The weaker interactions between A-site cations and oxygen ions contribute to greater structural flexibility, enabling the lattice to adapt to external changes, especially under temperature fluctuations or stress. However, this complexity results in relatively poor stability for the orthorhombic phase, making it more susceptible to environmental changes. Due to the low symmetry of orthorhombic perovskites, the interactions between oxygen ions and metal ions are more intricate, leading to a strong directional dependence in the formation and migration of oxygen vacancies. The generation of oxygen vacancies is closely linked to lattice distortion, with their formation rate increasing under high temperatures or stress. This structural feature gives orthorhombic perovskites an advantage in certain catalytic reactions, particularly when their lattice structure can strongly interact with reactants, potentially enhancing catalytic performance. However, the complexity of the structure and its relatively low stability also limit the widespread application of orthorhombic perovskites, particularly regarding their operational stability at high temperatures and long-term performance [126,127].

2.2.5. Rhombohedral Phase

The rhombohedral phase of perovskite oxides typically adopts the $R\overline{3}c$ space group, exhibiting lower symmetry compared to other perovskite structures, which results in distinct lattice distortions [128]. In this structure, the octahedra formed by the A-site and B-site cations are arranged asymmetrically, leading to lattice elongation or compression and introducing directional differences. Unlike other common crystal phases, the octahedra in the rhombohedral phase are not perfectly symmetrical, and undergo distortion along specific directions, resulting in a non-homogeneous lattice structure [129]. In the rhombohedral phase, the interactions between the A-site cations and the oxygen octahedra are uneven, causing the oxygen ions to arrange with tilting, which results in a non-uniform distribution of oxygen vacancies [130]. This local structural asymmetry affects the formation and migration of oxygen vacancies, and their distribution and dynamic behavior may change under varying external conditions [131,132]. Especially under certain conditions, the strength of the metal-oxygen bond and the coordination environment of oxygen ions exhibit strong anisotropy. The rhombohedral phase's crystal structure also displays strong interlayer interactions, further influencing the stability of the oxygen octahedra and the mobility of oxygen ions. Due to the asymmetry of the lattice, the metal-oxygen coordination structure becomes looser or tighter along certain directions, affecting its stability and catalytic performance [133,134]. Moreover, this asymmetry makes the rhombohedral phase more prone to structural deformation under high temperatures or stress, impacting its catalytic stability, particularly during prolonged operation, where phase transitions may occur, leading to performance degradation. In summary, rhombohedral-phase perovskite oxides exhibit high thermal stability; however, their structural asymmetry and sensitivity to environmental changes pose certain challenges for long-term applications.

2.2.6. Monoclinic Phase

Monoclinic perovskite oxides typically belong to the space group C2/c, exhibiting low symmetry, which results in unequal unit cell parameters along different directions. This reduced symmetry leads to significant distortions along the a- and c-axes, and the coordination environment of the oxygen octahedra becomes inhomogeneous, influencing the distribution of oxygen vacancies and the kinetics of electrocatalytic reactions [135,136]. In the monoclinic phase, the coordination between the B-site cations and oxygen ions is relatively loose, and the oxygen ions are unevenly positioned, leading to inconsistent bond lengths within the oxygen octahedra, further facilitating the formation of oxygen vacancies [137]. Oxygen vacancies play a critical role in the monoclinic phase by providing more active sites for reactants and accelerating the oxygen reduction reaction. Due to the strong anisotropy of this phase, the chemical environment varies significantly along different directions, which may result in high catalytic activity under specific conditions. However, this inhomogeneity also makes it prone to structural degradation or phase transitions at elevated temperatures, which compromises its thermodynamic stability and long-term performance. Consequently, while monoclinic perovskites exhibit strong activity in certain catalytic reactions, their stability and complex thermodynamic behavior pose challenges for practical applications.

2.3. Impact of Crystal Phases on Electrocatalytic Reaction Mechanisms and Performance for Water Splitting

For clarity, oxygen vacancies discussed in the following sections may originate from a variety of sources, including thermodynamically formed bulk vacancies, kinetically stabilized surface or near surface vacancies, and electrochemically induced defects generated under operating conditions. Thermodynamically formed bulk vacancies typically arise from intrinsic lattice instabilities or nonstoichiometry under high temperature or low oxygen pressure environments, whereas kinetically stabilized surface or near surface vacancies often result from processing conditions, surface reconstruction, or adsorption desorption dynamics. Electrochemically induced defects, on the other hand, are dynamically generated under applied potentials or during redox cycling, and their concentration and distribution can be highly sensitive to the local electrochemical environment. Unless otherwise specified, the discussion hereafter primarily focuses on surface-related oxygen vacancies, which are most directly involved in interfacial charge transfer, catalytic adsorption, and electrocatalytic reactions. These surface vacancies not only modulate the local electronic structure and surface reactivity, but also serve as active sites that govern reaction kinetics, selectivity, and overall performance in energy conversion and storage applications.

Within this context, it is important to clarify the hierarchical relationship among lattice distortion, octahedral tilting, and bond angle deviation in perovskite oxides. These structural descriptors are not independent, but rather represent different manifestations of symmetry lowering across length scales. Lattice distortion reflects the overall deviation of the crystal framework from ideal cubic symmetry and is commonly accommodated through cooperative tilting of BO_6 octahedra, which directly induces deviations of the B-O-B bond angle from 180°, providing a local structural parameter that governs orbital overlap, electronic bandwidth, and metal oxygen covalency. Consequently, bond angle deviation modulates the overlap between O-2p and transition metal 3d orbitals, thereby regulating electronic structure, charge transfer characteristics, and defect energetics. Beyond this, these structural perturbations manifest both at local and long range scales: while lattice distortion captures the global symmetry lowering, octahedral tilting and bond angle deviation provide a nuanced understanding of local distortions that directly influence the chemical environment around active sites, affecting not only electronic density distribution but also lattice vibrational properties and electron phonon coupling. Moreover, the anisotropic strain associated with tilting leads to preferential modifications in cation anion bond lengths, further tuning the energetic landscape for defect formation, migration, and stabilization. This is particularly relevant for oxygen vacancies, whose formation and mobility are highly sensitive to local coordination asymmetry, and the interplay between global lattice distortion and local octahedral behavior establishes a multiscale framework linking crystallographic symmetry, electronic structure, defect chemistry, and ultimately functional properties such as electrocatalytic activity, ionic conductivity, and redox behavior.

To explore the impact of crystal phases of perovskite oxides on electrocatalytic water splitting performance, several critical factors must be considered, including lattice symmetry, oxygen vacancy distribution, lattice distortion, and surface structure, which all play a pivotal role in determining catalytic activity (Figure 4). These factors not only affect the electronic structure of perovskite oxides but also govern their interaction with reaction intermediates during the catalytic process, thus influencing the overall electrocatalytic performance.

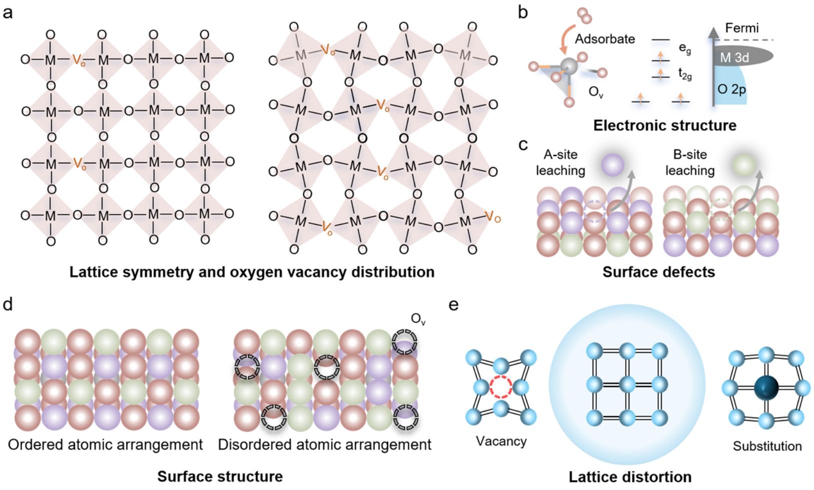

Figure 4. Correlation between crystal phases and electrocatalytic performance in perovskite oxides. (**a**) Lattice symmetry and oxygen-vacancy distributions in ordered and distorted octahedral frameworks; (**b**) Electronic structure modulation, showing adsorbate interactions with oxygen vacancies and the relative O-2p and M-3d orbital levels; (**c**) Surface defect generation through A-site or B-site leaching, inducing local structural and electronic perturbations; (**d**) Ordered and disordered surface atomic arrangements, highlighting vacancy-induced disorder; (**e**) Lattice distortion associated with vacancy formation and cation substitution, illustrating local structural relaxation around defect sites.

Firstly, lattice symmetry fundamentally dictates the electronic characteristics of perovskite oxides. Perovskites with high symmetry, such as the cubic phase, exhibit a more ordered and stable atomic arrangement, leading to relatively lower conductivity. This lack of localized electronic states limits the interaction between surface electrons and reactant molecules, thus reducing catalytic efficiency. In contrast, lower-symmetry perovskite phases, such as hexagonal and orthorhombic phases, often exhibit more structural defects and asymmetrical atomic arrangements. These defects serve as active sites, enhancing electron transfer and reactant adsorption, which boosts catalytic activity. These local defects modulate the electronic density and structure of the catalyst, creating more reactive sites that can accelerate electrocatalytic reactions [138].

Secondly, the generation and distribution of oxygen vacancies are essential for determining the catalytic activity of perovskite oxides. Oxygen vacancies not only act as active sites for water molecule adsorption and dissociation but also serve as critical sites for the adsorption of reaction intermediates, such as hydroxide ions, during the electrocatalytic process. In perovskite phases with lower symmetry, such as hexagonal and orthorhombic phases, lattice distortion enhances the formation and non-uniform distribution of oxygen vacancies, promoting enhanced adsorption and activation of water molecules. These defects provide a localized electronic structure that facilitates the dissociation of water and the formation of hydroxide intermediates. In contrast, cubic-phase perovskites, with their more ordered structures, show more uniform and sparse oxygen vacancies, resulting in less catalytic activity. The density and distribution of oxygen vacancies influence the overall catalytic pathway, including charge transfer and the stability of reaction intermediates, which directly impact the efficiency and selectivity of the water splitting reaction [139,140].

Lattice distortion also plays a crucial role by influencing the electronic structure and charge transfer properties of the catalyst. Perovskites with significant lattice distortion, such as hexagonal and orthorhombic phases, induce localized stress effects that lead to the uneven distribution of electrons on the catalyst surface. This distortion can enhance the electron transfer properties of the catalyst, thus accelerating the catalytic process. The stress effects induced by lattice distortion create more "active states" on the catalyst surface, making them more effective in promoting electron and reactant molecule interactions. For instance, the higher lattice distortion in hexagonal-phase perovskites results in a more reactive surface, facilitating faster electron transfer and reducing the activation energy for water dissociation. In comparison, cubic-phase perovskites, with their symmetrical and less-distorted structure, exhibit weaker electron transfer capabilities, limiting the rate of catalytic reactions.

Additionally, surface structure is crucial in determining catalytic performance. The arrangement of surface atoms, the presence of defects, and the distribution of these defects significantly influence the catalytic reaction.

Perovskite oxides typically have surfaces rich in defects and irregular atomic arrangements, which provide more active sites for reaction and enable better interaction with reactant molecules [141–143]. Lower-symmetry phases such as hexagonal and orthorhombic phases have more surface defects, promoting water adsorption, dissociation, and intermediate formation, leading to enhanced catalytic efficiency. On the other hand, higher-symmetry phases like cubic perovskites, with their smoother and more ordered surfaces, have fewer defects, resulting in lower surface activity and reduced catalytic efficiency [144]. Furthermore, the coordination environment between surface atoms and oxidation-reduction intermediates affects the catalytic reaction pathway. By adjusting the defect density and surface coordination environment, perovskite oxides can tune the catalytic activity, further reinforcing the connection between crystal phase structure and electrocatalytic performance [145–147].

It should be noted that, although reduced crystallographic symmetry is frequently associated with enhanced oxygen vacancy formation and improved electrocatalytic activity, this correlation is not universal. High symmetry cubic perovskites with optimized B-site valence states, strong metal oxygen covalency, and favorable electronic configurations can also exhibit excellent OER performance, even in the absence of a high intrinsic vacancy concentration. Therefore, crystallographic symmetry should be regarded as an enabling, rather than an exclusive, factor in governing catalytic activity.

Moreover, it is essential to distinguish among oxygen vacancy concentration, vacancy ordering, and vacancy mobility, as these descriptors capture fundamentally different aspects of defect chemistry. While vacancy concentration reflects the thermodynamic propensity for defect formation, vacancy ordering describes the spatial arrangement and correlation of vacancies within the lattice, which can strongly influence electronic structure and lattice stability. Vacancy mobility, on the other hand, governs the dynamic accessibility of active sites and oxygen exchange kinetics under operating conditions. Importantly, reduced symmetry does not necessarily optimize all three parameters simultaneously; for instance, highly distorted structures may increase vacancy concentration but impede vacancy mobility due to local trapping or strong lattice distortions.

Consequently, the dominant factor governing catalytic activity depends on the specific materials regime and operating conditions. In systems where bulk defect formation and lattice oxygen participation are rate limiting, crystallographic symmetry and its associated structural distortions play a primary role. In contrast, when electronic structure descriptors such as metal oxygen covalency or occupancy are optimized, or when extensive surface reconstruction leads to the formation of oxyhydroxide active layers, catalytic performance may become less sensitive to the initial bulk symmetry. This nuanced interplay underscores the necessity of considering crystallographic symmetry, electronic structure, and surface reconstruction as complementary, rather than mutually exclusive, determinants of electrocatalytic activity.

To provide a design-oriented perspective, Table 1 establishes a unified framework that translates crystallographic symmetry from a qualitative structural concept into a set of quantitative and physically meaningful descriptors, including tolerance factor, octahedral tilting amplitudes, B-O-B bond angle deviations, and symmetry induced lattice strain. These symmetry derived descriptors are further correlated with oxygen defect energetics, such as vacancy formation energy, spatial distribution, ordering tendency, and migration barriers, thereby explicitly linking symmetry lowering to defect formation and transport behavior. By integrating structural, defect, and electronic considerations, this framework clarifies when crystallographic symmetry acts as a primary governing factor and when its influence is mediated through electronic structure or surface reconstruction. Importantly, it enables a systematic and internally consistent comparison across different crystal phases and identifies symmetry controlled parameters that can be deliberately tuned via composition, strain, or phase engineering to rationally optimize electrocatalytic activity, stability, and defect dynamics under realistic operating conditions.

Table 1. Crystallographic symmetry derived descriptors governing oxygen defect chemistry and electrocatalytic behavior in perovskite oxides.

Crystal Symmetry	**Space Group**	**Symmetry Derived Structural Descriptors**	**Oxygen-Defect Energetics and Characteristics**	**Electronic/Catalytic Implications**
Cubic Phase (high symmetry)	$Pm\bar{3}m$	Tolerance factor t ≈ 1; negligible octahedral tilting; B–O–B bond angle ≈ 180°	High oxygen vacancy formation energy ΔEv; low intrinsic vacancy concentration	Broad electronic bandwidth, strong orbital delocalization; limited surface defect density, typically moderate catalytic activity
Hexagonal Phase	$P6_3/mmc$	Face-sharing octahedra; non-perovskite connectivity; reduced B–O orbital overlap	Preferential vacancy formation at specific lattice sites	Distinct reaction pathways and surface chemistry; unique activity trends beyond conventional perovskite models
Tetragonal Phase	I4/mcm	Anisotropic lattice distortion; moderate octahedral rotation along c-axis; slight B–O–B angle deviation	Moderately reduced ΔEv; anisotropic vacancy distribution	Direction-dependent electronic structure; enhanced surface reactivity along specific crystallographic orientations

Table 1. *Cont.*

Orthorhombic Phase	Pbca	Pronounced cooperative octahedral tilting; significantly reduced B–O–B bond angle; t < 1	Lower ΔEv; enhanced vacancy concentration and mobility	Optimized metal–oxygen covalency and p–d orbital overlap; favorable balance between electronic conductivity and defect reactivity for OER
Rhombohedral Phase	$R\bar{3}c$	Trigonal distortion; coupled octahedral rotation and lattice strain; asymmetric local coordination	Stabilized surface and near surface oxygen vacancies	Enhanced adsorption of oxygen intermediates; improvedcharge-transfer kinetics and catalytic turnover
Monoclinic Phase (low symmetry)	C2/c	Strong symmetry lowering; diverse bond-length and bond-angle distributions; local coordination heterogeneity	Highly heterogeneous vacancy formation energies; defect-rich surfaces	High density of catalytically active sites; enhanced reaction flexibility but potentially reduced structural stability

2.4. Statistical Summary of Perovskite Oxides for Electrocatalytic Water Splitting

To specify, we use defect related terms such as "mismatch" and "symmetry deviation" to describe specific physical origins, including ionic size or lattice parameter mismatches and deviations from ideal perovskite symmetry at both local and long range scales. These descriptors capture subtle structural perturbations that arise from compositional heterogeneity, cation substitution, or strain effects, which can influence lattice stability, electronic structure, and ion transport properties. Importantly, these concepts are distinct from intrinsic point defects, such as oxygen vacancies, unless explicitly stated, as they reflect broader structural inconsistencies rather than the presence of discrete missing or interstitial atoms. By clearly delineating these categories, we provide a rigorous framework for interpreting structural distortions and their consequences on the functional behavior of perovskite oxides, including effects on electronic conductivity, catalytic activity, and defect formation energetics. Such distinctions are essential for accurately correlating microscopic structural features with macroscopic material performance in experimental and computational studies.

The compiled data reveal several consistent structure–performance correlations spanning crystalline symmetry, A-site chemistry, and B-site configuration (Table 2). Cubic and near-cubic perovskites that host Co or Ni at the B site and Sr or Ba at the A site frequently deliver the lowest η at 10 mA cm^{-2} with Tafel slopes in the approximate 40–70 mV dec^{-1} band, a trend attributable to higher tolerance factors, reduced octahedral tilts, and elevated B-site valence states that push e_g occupancy toward unity while sustaining p-type conductivity; representative $Sr(Co,Fe)O_{3-\delta}$ and $Ba(Sr)CoO_{3-\delta}$ families typify this regime with multi-tens of hours to hundreds of cycles of stable operation. Rhombohedral variants containing La retain competitive overpotentials with improved cycling endurance, indicating that slightly lower symmetry can moderate reconstruction while preserving strong O 2p–TM 3d covalency. Hexagonal and tetragonal entries generally show higher kinetic slopes and η values unless vacancy ordering or layered stacking introduces rapid anion transport pathways, suggesting that anisotropic lattices require deliberate vacancy and bandwidth engineering to offset less favorable crystal-field landscapes. Orthorhombic compositions span a wide activity window, and performance rises markedly when A-site Sr/Ba substitution increases average B-site valence and oxygen nonstoichiometry, highlighting a vacancy-assisted route to accelerate *OH and *O formation. Monoclinic examples are fewer but include cases with respectable HER or bifunctional behavior when heteroatom doping or conductive scaffolds compensate for limited intrinsic transport. Across A-site chemistry, alkaline-earth substitution (Sr, Ba, Ca) consistently enhances OER metrics by enforcing charge compensation to $TM^{3.5+}$–TM^{4+} and by lowering vacancy formation barriers, whereas rare-earth La and Gd often improve durability through stronger lattice cohesion at comparable activity. B-site trends indicate a hierarchy where Co > Ni > Fe for OER mass activity at similar symmetry and vacancy levels, while Fe incorporation in Co/Ni matrices stabilizes high-valent states and suppresses parasitic oxygen release, narrowing Tafel slopes without sacrificing longevity. Perovskite-derived phases, notably brownmillerites and vacancy-ordered orientations, show distinct advantages for both OER and HER by combining labile oxygen channels with electronically percolating frameworks; stability improves further when surface reconstruction yields thin oxyhydroxide skins over oxygen-deficient perovskite subsurfaces rather than complete amorphization. Composites and heterostructures in the table, including MXene-coupled and noble-metal-modified systems, lower η and extend cycle life by boosting charge delivery and protecting the lattice, although entries with excessive A-site leaching or poorly anchored dopants exhibit rapid decay. Taken together, the statistics indicate that optimal catalysts co-maximize lattice symmetry near the cubic limit, A-site compositions that drive high B-site valence with controllable δ, and B-site chemistries that balance strong covalency with moderated vacancy densities, while permitting reconstructive formation of stable oxyhydroxide interfaces that sustain high turnover under prolonged bias.

Table 2. A comprehensive overview of electrocatalytic performance of perovskite oxides.

Crystalline Phases	**Material**	**Application**	**Electrolytes**	**Tafel Slope (mV dec^{-1})**	**Overpotential (η @ j, mV)**	**Stability (@ Current Density)**	**Ref.**
Cubic phase	$LaNiO_3$	UOR	1 M KOH + 0.33 M urea	33.1	-	45 h @ 50 mA cm^{-2}	[148]
	$BaCo_{0.7}Fe_{0.2}Sn_{0.1}O$	OER	0.1 M KOH	68 ± 2	-	-	[149]
	Sm-$LaCoO_3$	OER	1 M PBS (pH 7)	135.5	$\eta_{10} = 530$	50 h @ 10 mA cm^{-2}	[150]
	LSCO	OER	1 M KOH	76.6	$\eta_{10} = 360$	-	[151]
	10%Fe-$SrCoO_{3-\delta}$	OER	0.1 M KOH	-	$\eta_{10} \approx 410$	2 h @ 10 mA cm^{-2}	[152]
	$MoReS_2$/LSC	OER	1 M KOH	37.2	$\eta_{10} = 210$	200 h @ 20 mA·cm^{-2}	[153]
	LSFN-0.4	OER	0.1 M KOH	35	$\eta_{10} = 320$	36 h @ 9.3mA·cm^{-2}	[39]
	SFSi	OER	0.1 M KOH	58	-	-	[154]
	BSCF	OER	0.1 M KOH	-	-	-	[68]
	$La_{0.6}Ca_{0.4}(CrMnFeCo_2Ni)\ O_3$	OER	1 M KOH	57.4	$\eta_{10} \approx 340$	200 h @10 mA·cm^{-2}	[155]
	P-HEO	OER	1 M KOH	51	-	-	[156]
	L-0.5/rGO	OER	1 M KOH	80	$\eta_{10} = 338$	-	[157]
		HER	1 M KOH	46	$\eta_{150} = 187$	-	
	P-PLBC-F	HER	1 M KOH	32.9	$\eta_{10} = 208$	-	[158]
	LBSCOF	HER	1 M KOH	44	$\eta_{100} = 256$	-	[159]
	$SrTi_{0.7}Ru_{0.3}O_{3-\delta}$	HER	1M KOH	40	$\eta_{10} = 46$	200 h @10 mA·cm^{-2}	[160]
	$BaMoO_3$	HER	1 M KOH	110	$\eta_{10} = 336$	-	[161]
Hexagonal phase	6H–$SrIrO_3$	OER	0.1 M $HClO_4$	54.5	$\eta_{10} = 256$	-	[162]
	LMN	OER	1 M KOH	88.3	$\eta_{10} = 318$	20 h @ 10 mA·cm^{-2}	[163]
		HER	1 M KOH	96.3	$\eta_{10} = 225$		
Tetragonal phase	PO_4-PBCC	OER	0.1 M KOH	51	$\eta_{10} = 290$	100 h @ 10 mA·cm^{-2}	[164]
	$PrBaCo_2O_{5+\delta}$	OER	-	-	-	-	[165]
Orthorhombic phase	$SrIrO_3$	OER	0.5 M H_2SO_4	59.5	-	-	[166]
	$Gd_{0.8}Sr_{0.2}FeO_3$	OER	1 M KOH	55.85	$\eta_{10} = 294$	20 h @10 mA cm^{-2}	[167]
	$Sr_{0.9}Na_{0.1}RuO_3$	OER	0.1 M $HClO_4$	-	$\eta_{0.5} = 120$	-	[168]
	$LaMnO_3$	OER	0.1 M KOH	74	$\eta_{10} = 324$	10 h @ 10 mA cm^{-2}	[169]
	$CaMnO_3$/C	OER	0.1 M KOH	197	-	-	[170]

Table 2. *Cont.*

Crystalline Phases	**Material**	**Application**	**Electrolytes**	**Tafel Slope (mV dec^{-1})**	**Overpotential (η @ j, mV)**	**Stability (@ Current Density)**	**Ref.**
Orthorhombic phase	$NdBaMn_2O_{5.5}$	OER	1 M KOH	75	η_{10} = 430	50 h @ 10 mA cm^{-2}	[171]
		HER	1 M KOH	87	η_{10} = 290		
	S-LCF	OER	1 M KOH	60	η_{10} = 360	7 h @~11.5 mA cm^{-2}	[172]
		HER	1 M KOH	-	η_{10} = 340		
	$La_{0.6}Sr_{0.4}CoO_3$ (HTS-2)	OER	1 M KOH	73	η_{10} = 363	-	[173]
		HER	1 M KOH	52	η_{10} =261		
Rhombohedral phase	$Sr_{0.1}La_{0.9}Ni_{0.5}Co_{0.5}O_3$	OER	H_2O	-	η_{1000} =1810	20 h @ 500 mA cm^{-2}	[174]
	$LaNiO_3$ nanocrystals	OER	0.1 M KOH	-	η_{10} = 440	-	[77]
Monoclinic phase	S-doped M-$SrIrO_3$	OER	0.5 M H_2SO_4	58.4	η_{10} = 228	20 h @ 10 mA·cm^{-2}	[175]
	4CeO_2@$SrIrO_3$	OER	0.5 M H_2SO_4	71.7	η_{10} = 238	50 h @ 10 mA·cm^{-2}	[176]
	Ir@$SrIrO_3$	OER	0.5 M H_2SO_4	61.8	η_{10} = 229	100 h @ 10 mA·cm^{-2}	[177]
		HER		27.6	η_{10} = 28		
	$La_2(Co_{1/6}Ni_{1/6}Mg_{1/6}Zn_{1/6}Na_{1/6}Li_{1/6})RuO_6$	HER	1 M KOH	97.8	η_{10} =40.7	82 h @ 10 mA·cm^{-2}	[178]
Derived structure	PBSCF-III	OER	0.1M KOH	52	η_{10} = 358	12 h @ 10 mA·cm^{-2}	[179]
	$CaCu_3Fe_4O_{12}$	OER	0.1 M KOH	51	$\eta_{0.5}$ = 310	-	[180]
	$SrCoO_{2.52}$	OER	1.0 M KOH	-	η_{10} = 525	-	[27]
	$(Pr_{0.5}Ba_{0.5})_2Co_2O_{5+\delta}$	OER	-	-	-	-	[181]
	$LaNiO_{3-\delta}$ (111)	OER	0.1 M KOH	50.4	η_1 = 450	-	[182]
	$CaCu_3Co_2Ru_2O_{12}$	OER	1 m KOH	37	η_{10} = 198	500 h @ 500 mA cm^{-2}	[183]
	LSNF30	OER	0.1 M KOH	44	η_{10} = 360	-	[36]
	$La_{0.6}Sr_{0.4}CoO_{3-\delta}$	OER	0.1 M KOH	~88	-	200 h @ 0.1mA cm^{-2}	[184]
	$LaMnNiCoO_3$ (1:2:3)	OER	0.1 M KOH	80.19	η_{10} = 370	-	[185]
	BM-$SrFeO_{2.5}$	OER	1 M KOH	70.5	η_1 = 460	-	[186]
	BICO-2	OER	0.5 M H_2SO_4	46.3	η_{10} = 216	140 h @ 10 mA cm^{-2}	[187]
	SNCF-NRs	OER	0.1 M KOH	61	η_{10} = 390	10 h @ 10 mA cm^{-2}	[188]
		HER	0.1 M KOH	134	η_{10} = 262		
	LSC/K-$MoSe_2$	OER	1 M KOH	79	η_{10} = 230	2500 h @ 100 mA cm^{-2}	[189]
		HER	1 M KOH	45	η_{10} = 128		
	TRO/RKLTO	HER	1 M KOH	-	η_{10} = 20	-	[190]

It is important to emphasize that the performance data compiled in Table 2 originate from different studies employing varied testing conditions, including electrolyte environments, pH values, applied current densities, and durability evaluation protocols. As a result, direct numerical comparisons of overpotentials or current densities across different crystal phases may not always be strictly valid. Accordingly, the discussion in this review focuses primarily on identifying trend based correlations between crystallographic symmetry, defect chemistry, and catalytic behavior, rather than on absolute performance metrics.

Where available, intrinsic descriptors such as Tafel slopes, electrochemically active surface area (ECSA) normalized activities, and stability trends under comparable conditions are emphasized, as these metrics provide more reliable insights into the underlying catalytic mechanisms and structure activity relationships. This approach allows for a more rigorous and meaningful comparison of how crystal phase and symmetry influence electrocatalytic performance across diverse material systems.

3. Crystalline Structure-Dependent Electrocatalytic Behavior of Perovskite Oxides

Perovskite oxides display distinct advantages in water splitting that arise from crystal-phase-controlled lattice symmetry, oxygen-defect thermodynamics, and coordination chemistry. To clarify how structure governs activity, the discussion is organized into two complementary categories aligned with this review's chapter sequence. Section 3.1 examines A-site cation families in the order La-series, Sr-series, Ba-series, Ca-series, and Gd-series, emphasizing how tolerance factor, octahedral tilts, and charge-compensation pathways regulate B-site valence and vacancy formation [191,192]. Section 3.2 then analyzes B-site transition-metal families in the order Co-series, Ni-series, Fe-series, Mn-series, and Cr-series, highlighting how e_g occupancy, metal–oxygen covalency, and redox manifolds set intermediate binding and charge-transfer kinetics [193,194]. Across both categories, variations in symmetry, oxygen vacancy distribution, and local coordination create measurable differences in electrocatalytic activity, durability, and intermediate affinity under operating bias. The following subsections integrate these factors to extract actionable structure–activity correlations that guide the rational design of high-performance perovskite electrocatalysts for water splitting.

3.1. A-Site Cation-Based Perovskite Oxides and Their Electrocatalytic Properties

3.1.1. La-Series Perovskite Oxides

La-based perovskite oxides exhibit significant catalytic activity in electrocatalytic water splitting, with their crystal structure playing a pivotal role in determining their performance [195]. The fundamental crystal structure of La-perovskite oxides is of the ABO_3 type, where La^{3+} occupies the A-site, and transition metal ions occupy the B-site. The relatively large ionic radius of La^{3+} (approximately 1.36 Å) results in a larger lattice constant, typically around 3.84 Å, which induces lattice distortion, particularly when the distance between the A-site and B-site ions is stretched or compressed. This lattice distortion creates space for oxygen vacancy formation, which in turn serves as a catalytic center for the adsorption and dissociation of reaction intermediates [196]. Consequently, the presence of oxygen vacancies lowers the energy barrier for the water splitting reaction. The crystal symmetry of La-based perovskite oxides is relatively low, which enhances their catalytic performance. Specifically, the oxygen positions within the perovskite structure exhibit a high degree of delocalization, enabling more efficient participation in the catalytic process. The concentration of oxygen vacancies is closely related to the oxidation state and coordination environment of the B-site transition metal, which can be tuned by adjusting the doping of the A-site cation or by optimizing lattice distortion. The electrostatic effect of La^{3+} further enhances the oxidation-reduction capacity of the B-site transition metal, facilitating the OER during water splitting. Moreover, the lattice structure of La-based perovskite oxides allows for the fine-tuning of the electron density distribution, optimizing the reaction kinetics of oxidation-reduction processes, and improving the efficiency of electrocatalytic water splitting. Additionally, La-based perovskite oxides exhibit high thermal stability and excellent corrosion resistance, maintaining good electrocatalytic activity over a wide pH range, which is crucial for long-term stability in practical applications [197,198]. Therefore, the unique structural characteristics of La-based perovskite oxides offer distinct advantages in electrocatalytic water splitting.

In recent years, significant research attention has been devoted to understanding how crystal structure regulation influences the electrocatalytic activity of La-based perovskite oxides for water splitting. Building on this foundation, Park et al. employed a template-assisted epitaxial growth strategy to precisely tailor the crystal orientation and interfacial electronic environment of $La_{0.6}Sr_{0.4}CoO_{3-\delta}$ (LSC) through integration with $MoReS_2$ nanosheets [153]. As shown in Figure 5A, the atomic structure model indicates that the lattice coherence between the LSC (110) plane and the $MoReS_2$ substrate promotes oriented epitaxial growth and induces moderate lattice distortion, thereby exposing high-energy facets favorable for oxygen adsorption and catalytic activation. Figure 5B further confirms through high-resolution TEM that a coherent and defect-free van der Waals interface is formed, enabling efficient interfacial coupling and charge redistribution that optimize the electronic configuration of Co sites. Correspondingly, Figure 5C demonstrates that the facet-engineered $MoReS_2$/LSC heterostructure achieves an overpotential of 210 mV at 10 mA cm^{-2} and a Tafel slope of 37.2 mV dec^{-1}, outperforming pristine LSC (400 mV, 160 mV dec^{-1}) and even the benchmark IrO_2 catalyst (340 mV). Collectively, these findings reveal that facet orientation control and interfacial electronic modulation synergistically enhance the oxygen evolution activity and reaction kinetics of La-based perovskite oxides. Following the facet-engineering approach, Yu et al. employed an A-site substitution strategy to precisely modulate the lattice structure and electronic configuration of $LaCoO_3$ perovskite oxides for enhanced electrocatalytic activity [150]. As shown in Figure 5D, the substitution of La^{3+} with various rare-earth cations introduces controlled lattice distortion and modifies the Co–O bond geometry, thereby optimizing the structural symmetry and facilitating charge transport during oxygen evolution. In Figure 5E, the HRTEM image of Sm–$LaCoO_3$ after long-term OER testing demonstrates that the perovskite lattice remains highly crystalline, confirming its excellent structural integrity under electrochemical conditions. As illustrated in Figure 5F, the optimized perovskite, Sm–$LaCoO_3$, exhibits an overpotential of 530 mV at 10 mA cm^{-2} and a Tafel slope of 135.5 mV dec^{-1}, outperforming both unmodified $LaCoO_3$ and RuO_2, indicating that A-site substitution–induced lattice modulation effectively enhances the oxygen evolution kinetics of La-based perovskite oxides. Building upon the compositional optimization strategy, Hu et al. introduced a surface ion-exchange and nucleation-growth strategy to construct a perovskite-based composite with finely tuned structural and electronic features [190]. As shown in Figure 5G, the schematic depicts the synthesis of Ru-doped $K_{0.469}La_{0.531}TiO_3$ (RKLTO) coupled with Ti-doped RuO_2 (TRO) nanoparticles, where surface ion exchange enables Ru incorporation into the perovskite lattice and facilitates the controlled growth of TRO at the interface. In Figure 5H, high-resolution characterization clearly reveals the enrichment of Ru at the surface and edge regions, verifying the successful cation substitution and the formation of a coherent heterointerface. As presented in Figure 5I, the resulting TRO/RKLTO composite achieves an exceptionally low overpotential of 20 mV at 10 mA cm^{-2}, surpassing commercial Pt/C and conventional oxide catalysts, confirming that surface ion exchange–induced lattice reconstruction and interfacial coupling synergistically enhance the hydrogen evolution kinetics of perovskite oxides. Extending beyond interfacial engineering, Cui et al. employed a high-temperature shock (HTS) synthesis approach to finely regulate the crystal symmetry and defect chemistry of $La_{0.6}Sr_{0.4}CoO_3$ perovskite oxides for enhanced water oxidation [173]. As shown in Figure 5J, the atomic structure model depicts the orthorhombic phase of $La_{0.6}Sr_{0.4}CoO_3$, where the ultrafast HTS process induces localized lattice distortion at Co sites and generates oxygen vacancies that serve as active centers for catalytic reactions. In Figure 5K, the HAADF-STEM image of the HTS-processed sample (HTS-2) reveals a well-preserved orthorhombic lattice featuring uniformly distributed cations and abundant defect sites, indicating that rapid thermal activation simultaneously maintains crystallinity and introduces structural disorder beneficial for catalysis. As presented in Figure 5L, the optimized HTS-derived catalyst achieves an overpotential of 280 mV at 10 mA cm^{-2} and a Tafel slope of 47 mV dec^{-1}, confirming that HTS-induced lattice reconstruction and defect modulation effectively accelerate charge transfer and oxygen evolution kinetics in La-based perovskite oxides.

3.1.2. Sr-Series Perovskite Oxides

Sr-based perovskite oxides occupy a distinctive position in water splitting catalysis because the A-site Sr^{2+} cation, with an ionic radius that yields a tolerance factor close to unity, produces lattices with modest octahedral tilts, high oxygen mobility, and comparatively low migration barriers for anion transport, features that couple favorably to fast redox cycling at the B site. In archetypes such as $SrCoO_{3-\delta}$, $SrFeO_{3-\delta}$, $SrNiO_3$, and related Sr-substituted La/Ba systems, A-site Sr^{2+} enforces charge compensation through increased B-site valence, raising the average d-electron oxidation state toward Co^{4+}, Fe^{4+}, or Ni^{3+} and tuning e_g occupancy toward the near-optimal regime for oxygen evolution, while the accompanying oxygen nonstoichiometry creates labile vacancies that accelerate adsorbate activation and lattice oxygen participation [199]. The perovskite–brownmillerite redox couple exemplified by $SrCoO_{3-\delta} \leftrightarrow SrCoO_{2.5}$ delivers reversible topotactic transformations that modulate Co–O coordination, electronic bandwidth, and defect chemistry under bias, thereby reshaping OER pathways between adsorbate-evolving and lattice-oxygen mechanisms according to δ and potential. Electronic transport in these oxides is typically p-type with strong metal–oxygen covalency, enabling rapid charge transfer to surface intermediates, while the relatively open Sr framework supports high vacancy diffusivity that sustains steady-state turnover at elevated current densities. Under alkaline operation, surface reconstruction often yields Sr-depleted oxyhydroxide layers and defect-rich perovskite subsurfaces; this dynamic passivation can lower kinetic barriers and expand electrochemically active area, yet uncontrolled A-site leaching compromises crystallographic integrity and long-term stability [200–202]. Effective design therefore centers on balancing vacancy concentration with electronic conductivity, stabilizing high-valent B-site states through compositional tuning or strain, and constraining detrimental A-site dissolution via surface terminations, heteroanion strategies, or protective scaffolds. Within this framework, Sr-series perovskites provide a versatile platform in which lattice symmetry, oxygen-defect thermodynamics, and B-site electronic structure can be co-engineered to realize high intrinsic OER activity with competitive durability, and to enable HER co-catalysis when coupled in bifunctional or heterostructured architectures [203].

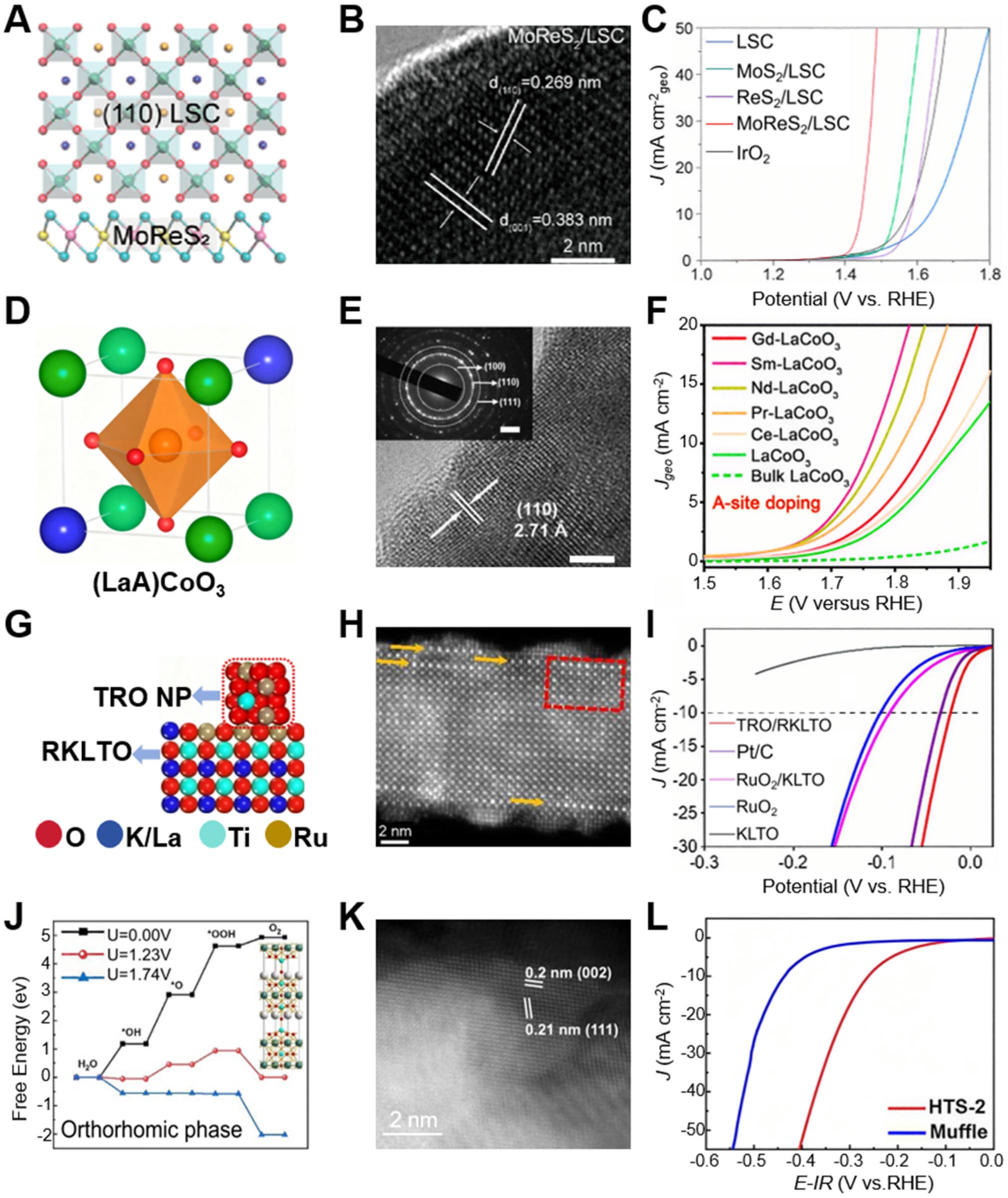

Figure 5. Structural and phase engineering of La-based perovskite oxides greatly enhance their bifunctional electrocatalytic performance for overall water splitting. (**A**) Structural schematic of cubic LSC on $MoReS_2$ interface. (**B**) HRTEM image of $MoReS_2$/LSC showing (110) and (001) lattice fringes. (**C**) OER polarization curves of LSC, MoS_2/LSC, ReS_2/LSC, $MoReS_2$/LSC, and IrO_2 [153]. Reproduced with permission from Ref. [153]. Copyright 2023, American Chemical Society. (**D**) Crystal structure model of A-site-substituted $(LaA)CoO_3$ perovskite. (**E**) HRTEM image of $LaCoO_3$ showing (110) lattice spacing of 2.70 Å. (**F**) OER polarization curves of $LaCoO_3$ and A-site-doped variants (Gd-, Sm-, Nd-, Pr-, Ce-$LaCoO_3$) [150]. Reproduced with permission from Ref. [150]. Copyright 2022, American Chemical Society. (**G**) Structural schematic of TRO nanoparticles on RKLTO substrate. (**H**) HAADF-STEM image showing lattice coupling of TRO/RKLTO. (**I**) HER polarization curves of TRO/RKLTO and reference catalysts [190]. Reproduced with permission from Ref. [190]. Copyright 2020, Royal Society of Chemistry. (**J**) HRTEM image of orthorhombic $La_{0.6}Sr_{0.4}CoO_3$ (HTS-2). (**K**) Free-energy diagram of OER pathways for orthorhombic $La_{0.6}Sr_{0.4}CoO_3$. (**L**) HER polarization curves of HTS-2 and muffle-calcined samples [173]. Reproduced with permission from Ref. [173]. Copyright 2024, Elsevier.

To further elucidate the tunability of lattice–electronic interactions within Sr-based perovskite oxides, several representative studies have demonstrated that A-site engineering serves as an effective route to optimize both catalytic activity and structural robustness under oxygen evolution conditions. Retuerto et al. systematically explored Na incorporation into the $SrRuO_3$ lattice, establishing a strong correlation between cation substitution, octahedral distortion, and electrocatalytic behavior in acidic environments [168]. Figure 6A illustrates the successful synthesis of $Sr_{1-x}Na_xRuO_3$ (x = 0, 0.05, 0.10), where homogeneous Na^+ doping preserves the orthorhombic perovskite framework while subtly modifying lattice parameters. Figure 6B reveals, through HRTEM and DDP analyses, that Na-doped samples maintain long-range crystallinity with less distorted RuO_6 octahedra, signifying enhanced structural stability. Figure 6C presents the polarization curves of $SrRuO_3$ (black), $Sr_{0.95}Na_{0.05}RuO_3$ (blue), and $Sr_{0.90}Na_{0.10}RuO_3$ (red), confirming that Na substitution markedly improves OER performance, achieving approximately 0.5 mA cm^{-2} at 1.35 V vs. RHE ($\eta \approx 120$ mV). Figure 6D compares the corresponding Tafel plots, showing that $Sr_{0.90}Na_{0.10}RuO_3$ delivers a current density of ~10 mA cm^{-2} oxide at ≈ 1.4 V with a Tafel slope near 40 mV dec^{-1}, outperforming pristine $SrRuO_3$ and approaching the intrinsic OER activity of benchmark Ir-based perovskites in acidic media. To further elucidate the structure–activity correlation revealed in Na-doped $SrRuO_3$, Kim et al. systematically examined the crystalline configuration and OER activity of Sr–Ir–O perovskites in acidic environments, elucidating the correlation between lattice symmetry and reaction kinetics [162]. Figure 6E illustrates the three-dimensional perovskite structure of $SrIrO_3$, in which corner-sharing IrO_6 octahedra construct a robust network that ensures high electronic conductivity and strong Ir–O covalency, favorable for charge transfer during oxygen evolution. Figure 6F displays the HAADF-STEM image of the layered Sr_2IrO_4 phase with an oriented (001) facet, revealing a highly ordered arrangement of alternating IrO_2 and SrO layers that stabilize the structure and regulate surface terminations. Figure 6G presents the corresponding atomic model of Sr_2IrO_4, showing that lattice strain and modulated Ir coordination enhance active-site accessibility and electronic coupling. Figure 6H compares the Tafel slopes of SrIrO–T and commercial IrO_2 in 0.5 M H_2SO_4, where SrIrO–T exhibits a smaller slope of approximately 44 mV dec^{-1}, reflecting accelerated charge-transfer kinetics and superior intrinsic activity. Building on the structural modulation strategies demonstrated in Sr–Ir–O systems, Dai et al. developed a single-phase $SrTi_{0.7}Ru_{0.3}O_{3-\delta}$ (STRO) perovskite oxide to probe the atomic-level mechanisms underlying hydrogen evolution activity [160]. Figure 6I illustrates the cubic perovskite framework of STRO, where Ti and Ru cations co-occupy the B-site lattice, forming corner-sharing octahedra that facilitate robust electronic coupling and efficient charge delocalization. Figure 6J depicts the super-exchange interaction between adjacent Ti^{3+} and Ru^{5+} centers, which strengthens orbital hybridization and improves electrical conductivity. Figure 6K compares the ECSA-normalized specific activity of STO, STRO, and SRO catalysts, demonstrating that STRO achieves the highest intrinsic activity of approximately 0.15 mA cm^{-2} ECSA at an overpotential of 0.1 V, attributed to optimized electronic interactions. Figure 6L presents the corresponding Tafel plots, where STRO exhibits a notably smaller slope of around 40 mV dec^{-1}, reflecting accelerated reaction kinetics and superior charge-transfer dynamics during the hydrogen evolution process. Following the compositional tuning explored in $SrTi_{0.7}Ru_{0.3}O_{3-\delta}$, Zhang et al. employed a microwave shock synthesis technique to fabricate cubic $La_{0.5}Sr_{0.5}CoO_{3-\delta}$ (LSCO), enabling ultrafast crystallization and homogeneous phase evolution within seconds [151]. As depicted in Figure 6M, the atomic structure model illustrates a highly ordered cubic lattice constructed from corner-sharing CoO_6 octahedra, forming a robust three-dimensional framework that facilitates efficient charge transport and provides abundant accessible active sites. This structural integrity is further corroborated by the SAED patterns in Figure 6N, which confirm the high crystallinity and pure cubic phase of LSCO, demonstrating the effectiveness of microwave-assisted synthesis in stabilizing the perovskite framework. Building upon this well-defined structure, Figure 6O compares the OER polarization behavior of LSCO, LCO, and RuO_2, revealing that LSCO exhibits a markedly lower overpotential and higher current density, indicative of superior intrinsic activity. Consistently, Figure 6P presents the corresponding Tafel analysis, where LSCO displays the smallest slope of approximately 49.5 mV dec^{-1}, signifying accelerated reaction kinetics and enhanced charge-transfer dynamics during the oxygen evolution process.

3.1.3. Ba-Series Perovskite Oxides

Ba-series perovskite oxides exhibit significant advantages in electrocatalytic water splitting due to their unique crystal structure and excellent catalytic performance. The Ba^{3+} ion, with a relatively large ionic radius (approximately 1.61 Å), results in a larger lattice constant, typically around 3.92 Å, which provides ample space for the formation of oxygen vacancies within the crystal structure. This characteristic plays a crucial role in electrocatalytic reactions. Ba-based perovskite oxides adopt an ABO_3-type structure, with Ba^{3+} occupying the A-site and transition metals such as Co^{3+} or Fe^{3+} occupying the B-site [204]. The larger size of Ba^{3+} induces lattice distortion, causing changes in the electronic structure of the B-site transition metals, which optimizes the redox reaction kinetics. This lattice distortion not only facilitates the formation of oxygen vacancies but also increases their concentration, enhancing the efficiency of electron transfer during the oxidation-reduction process [161,205]. In Ba-series perovskite oxides, oxygen vacancies are critical structural features that significantly impact catalytic performance. The formation of oxygen vacancies not only improves electronic conductivity but also provides additional active sites, increasing the activity for the OER during water splitting. Due to the strong electrostatic effect of Ba^{3+}, the oxidation-reduction reactions at the B-site transition metals are promoted, which accelerates the dissociation of water molecules. Compared to other perovskite oxides, Ba-series perovskites exhibit a higher concentration of oxygen vacancies, allowing for more efficient electrocatalytic reactions at lower overpotentials. Additionally, Ba-series perovskite oxides demonstrate superior catalytic stability over a wide pH range, which is essential for their durability in practical applications. Furthermore, Ba-series perovskite oxides can optimize their electronic structure by adjusting the combination of A-site and B-site ions, enhancing the adsorption and dissociation processes of reaction intermediates. Therefore, due to their unique structural advantages and catalytic properties, Ba-series perovskite oxides are emerging as highly promising materials for efficient electrocatalytic water splitting, particularly in facilitating the OER.

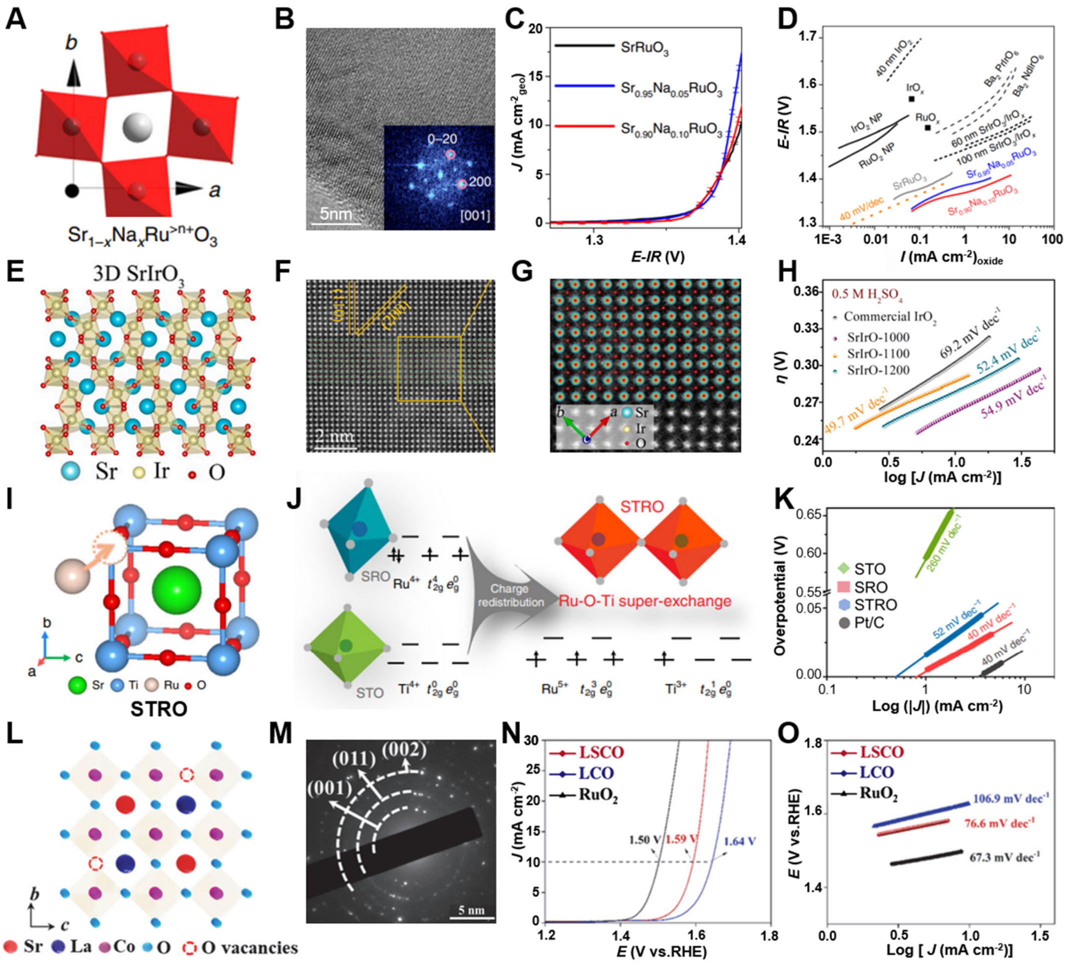

Figure 6. Lattice distortion and electronic modulation in Sr-based perovskite oxides drive enhanced catalytic performance for overall water splitting. (**A**) Crystal structure of Na-doped $SrRuO_3$ perovskite. (**B**) HRTEM image and FFT pattern of $Sr_{1-x}Na_xRuO_3$. (**C**) OER polarization curves of $SrRuO_3$ and Na-doped $SrRuO_3$. (**D**) Tafel plots comparing $Sr_{1-x}Na_xRuO_3$ with reference oxides [168]. Reproduced with permission from Ref. [168]. Copyright 2019, Springer Nature. (**E**) Crystal structure of 3D $SrIrO_3$ perovskite. (**F**) HAADF-STEM image of $SrIrO_3$ showing (110) and (200) planes. (**G**) Atomic-resolution image of $SrIrO_3$ lattice along [001] direction. (**H**) Tafel plots of $SrIrO_3$ samples synthesized at different temperatures [162]. Reproduced with permission from Ref. [162]. Copyright 2021, Elsevier. (**I**) Crystal structure of $SrTi_{0.5}Ru_{0.5}O_3$ (STRO) perovskite. (**J**) Schematic illustration of Ru–O–Ti super-exchange and charge redistribution in STRO. (**K**) Tafel plots of STO, SRO, STRO, and Pt/C catalysts [160]. Reproduced with permission from Ref. [160]. Copyright 2020, Springer Nature. (**L**) Crystal structure of $La_{0.2}Sr_{0.8}CoO_3$ with oxygen vacancies. (**M**) SAED pattern of cubic perovskite LSCO. (**N**) OER polarization curves of LSCO, LCO, and RuO_2. (**O**) Tafel plots of LSCO and reference catalysts [151]. Reproduced with permission from Ref. [151]. Copyright 2023, Elsevier.

Building on the preceding discussion of the structural and electronic characteristics of Ba-based perovskite oxides, the following study provides a clear demonstration of how phase transformation precisely governs catalytic behavior through structural reorganization and electronic modulation. Xu et al. achieved the transformation of scheelite-type $BaMoO_4$ into cubic perovskite $BaMoO_3$ via a hydrogen reduction process, enabling direct comparison of how crystal symmetry and lattice connectivity affect electrocatalytic activity [161]. The high-resolution TEM image (Figure 7A) reveals the formation of a highly ordered cubic lattice composed of interconnected MoO_6 octahedra, signifying the conversion from isolated MoO_4 tetrahedra to a perovskite framework that supports enhanced orbital overlap and electron delocalization. The polarization curves (Figure 7B) confirm that $BaMoO_3$ exhibits a substantially lower onset potential (−0.197 V vs. RHE) and overpotential (η_{10} = 336 mV) compared with $BaMoO_4$ (η_{10} = 561 mV), evidencing that the structural reconstruction effectively accelerates charge-transfer kinetics and facilitates hydrogen evolution. Furthermore, the electrical conductivity data (Figure 7C) show an increase exceeding seven orders of magnitude—from approximately 10^{-6} S cm^{-1} for $BaMoO_4$ to 10^{2} S cm^{-1} for $BaMoO_3$—reflecting a transition from insulating to metallic conduction. Collectively, these results highlight that the scheelite-to-perovskite phase transformation optimizes crystal symmetry, electronic structure, and active-site connectivity, thereby significantly enhancing the intrinsic electrocatalytic activity of $BaMoO_3$ perovskite for hydrogen evolution. Building upon the understanding of phase transformation in $BaMoO_3$, Hua et al. designed a fluorine-doped cubic perovskite oxide ($La_{0.5}Ba_{0.25}Sr_{0.25}CoO_{2.9-\delta}F_{0.1}$) to elucidate how anion substitution influences lattice structure and catalytic activity [159]. The schematic model (Figure 7D) illustrates the ideal cubic perovskite framework and corresponding $CoO_{6-\delta}$ polyhedra, where partial replacement of O^{2-} by F^{-} introduces controlled lattice distortion and oxygen vacancies, thereby modulating the local Co–O coordination environment. The structural representation (Figure 7E) further highlights that such fluorine incorporation enhances orbital hybridization between Co 3d and O 2p orbitals, facilitating charge delocalization and improving intrinsic electrical conductivity. As demonstrated by the polarization curves (Figure 7F), the F-doped perovskite delivers a significantly lower overpotential of 319 mV at 10 mA cm^{-2} and a smaller Tafel slope of 54 mV dec^{-1} relative to the undoped counterpart, confirming accelerated oxygen-evolution kinetics. Collectively, these findings demonstrate that fluorine-induced lattice modulation effectively tailors crystal symmetry and electronic structure, thereby enhancing charge-transfer efficiency and endowing the cubic Ba-containing perovskite with superior electrocatalytic activity for water oxidation. Building upon the effect of anion substitution on lattice modulation, Yang et al. synthesized Bi-substituted $BaIrO_3$ (BICO) perovskites using a sol–gel method followed by high-temperature annealing to elucidate the influence of A-site cation regulation on crystal structure and electrocatalytic behavior [187]. The charge-density distribution (Figure 7G) reveals that partial replacement of Ba^{2+} with Bi^{3+} redistributes electron density around Ir sites, weakens Ir–O bond strength, and promotes the adsorption of oxygen intermediates, which facilitates the lattice-oxygen mechanism. The HRTEM image (Figure 7H) of BICO-2 exhibits distinct lattice fringes corresponding to the (004) plane, confirming a well-ordered perovskite phase with localized lattice distortion and surface reconstruction that expose more catalytically active Ir–O sites. The Tafel slope data (Figure 7I) indicate that BICO-2 achieves a significantly lower value of 46.3 mV dec^{-1} compared with 82.1 mV dec^{-1} for pristine $BaIrO_3$, validating the improvement in charge-transfer kinetics and oxygen-evolution efficiency. Collectively, these findings demonstrate that A-site Bi substitution effectively optimizes lattice symmetry, modulates the IrO_6 octahedral framework, and enhances both the intrinsic activity and long-term stability of Ba-based perovskite oxides in acidic OER catalysis. Building upon the influence of A-site substitution on lattice distortion, Liu et al. synthesized a series of $PrBaCo_{2-x}Fe_xO_{5+\delta}$ ($PBCF_x$) perovskites via a sol–gel combustion method to elucidate the structural–functional relationship between ion ordering and catalytic activity [165]. The crystalline structure model (Figure 7J) reveals that $PBCF_{22}$ adopts a cubic perovskite phase with A-site disorder, where the random distribution of Pr^{3+} and Ba^{2+} disrupts long-range lattice symmetry and restricts oxygen-ion diffusion pathways. The HAADF-STEM elemental maps (Figure 7K) confirm a uniform elemental distribution but the absence of distinct cation ordering, indicating a disordered lattice that reduces structural coherence and limits electronic conductivity. The chronoamperometry curves (Figure 7L) demonstrate that the A-site ordered perovskite achieves a significantly higher current density of 3.40 A cm^{-2} at 2.0 V and 800 °C compared with its disordered counterpart, validating that ordered lattice symmetry substantially enhances oxygen-ion mobility and surface reaction kinetics. Collectively, these findings emphasize that precise control over crystal symmetry and cation ordering is crucial for optimizing structural stability, charge transport, and overall electrocatalytic efficiency in Ba-based double perovskite systems.

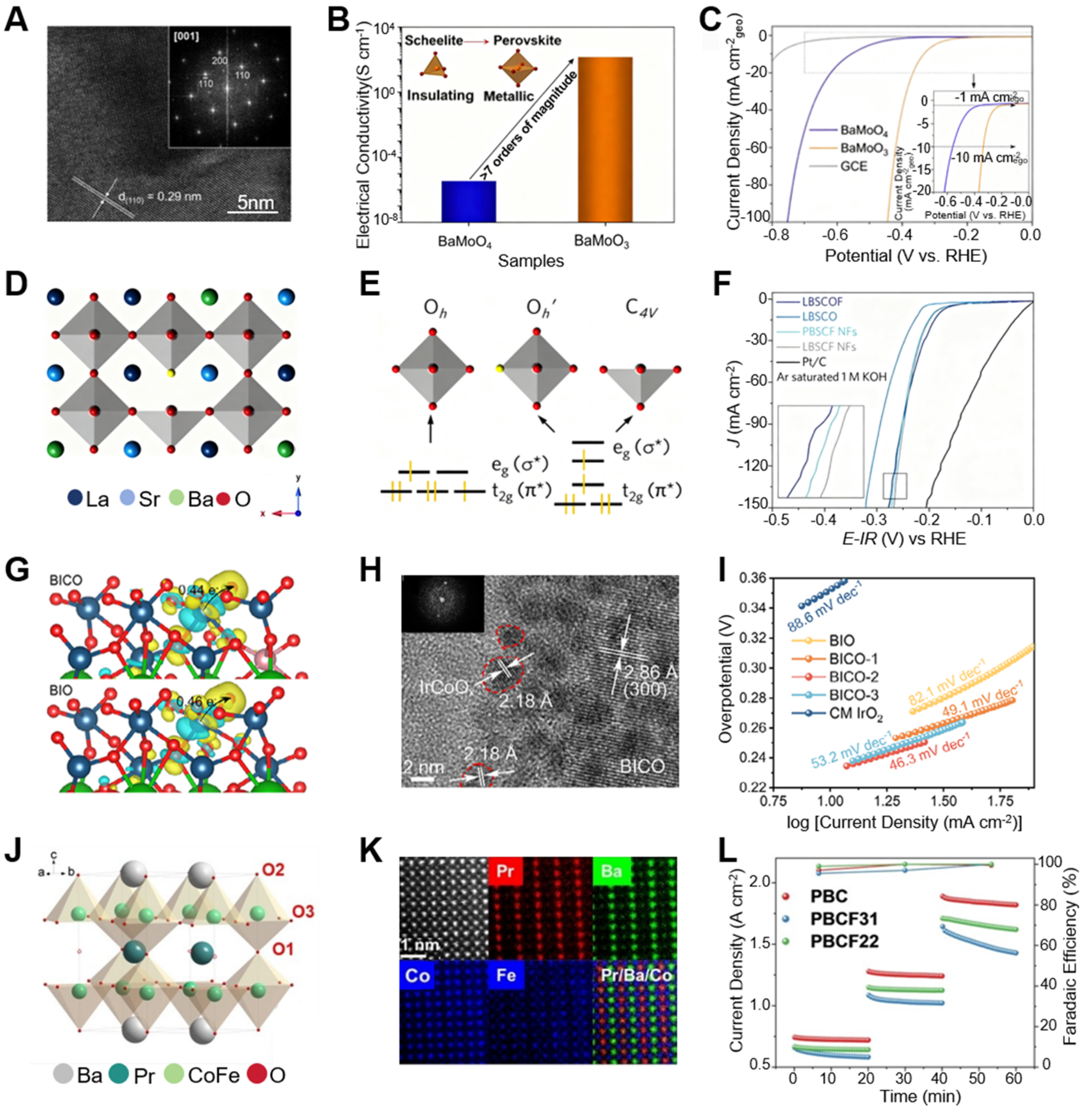

Figure 7. Crystal structure regulation and A-site substitution in Ba-based perovskite oxides promote superior OER and HER activity through optimized electron transport and surface reconstruction. (**A**) HRTEM image and FFT pattern of cubic $BaMoO_3$. (**B**) Electrical conductivity comparison between $BaMoO_4$ and $BaMoO_3$. (**C**) HER polarization curves of $BaMoO_4$ and $BaMoO_3$ catalysts [161]. Reproduced with permission from Ref. [161]. Copyright 2020, Elsevier. (**D**) HRTEM image and FFT pattern of cubic LBSCOF perovskite. (**E**) Electronic-orbital splitting diagram showing F-anion-induced energy-level shift. (**F**) Polarization curves for HER and OER of LBSCO and LBSCOF in 1 M KOH (η_{10} = 256 mV for HER, E_{100} = 1.748 V for OER) [159]. Reproduced with permission from Ref. [159]. Copyright 2018, Elsevier. (**G**) Charge-density difference of BIO and BICO. (**H**) HRTEM image of BICO showing $IrCoO_x$ nanoparticles. (**I**) Tafel plots of BIO, BICO, and IrO_2 catalysts [187]. Reproduced with permission from Ref. [187]. Copyright 2025, Wiley-VCH GmbH. (**J**) Crystal structure of $PrBaCo_{2-x}Fe_xO_{5+\delta}$. (**K**) Elemental mapping of Pr, Ba, Co, and Fe in the lattice. (**L**) Stability and Faradaic efficiency of PBC-based electrodes [165]. Reproduced with permission from Ref. [165]. Copyright 2023, Wiley-VCH GmbH.

3.1.4. Ca- and Gd-Series Perovskite Oxides

Ca-series perovskite oxides exhibit exceptional catalytic performance in electrocatalytic water splitting, driven by their unique crystal structure and efficient catalytic properties. The smaller ionic radius of Ca^{2+} (approximately 1.12 Å) results in a relatively compact lattice structure, with a lattice constant typically around 3.82 Å. This smaller ionic radius contributes to a more stable crystal lattice, which helps maintain high catalytic stability during electrocatalytic reactions. The Ca-series perovskite oxides adopt the ABO_3-type crystal structure, where Ca^{2+} occupies the A-site and transition metal ions such as Fe^{3+} and Ni^{2+} occupy the B-site. The smaller size of Ca^{2+} leads to a stronger oxidation-reduction capacity in the B-site metal ions and, through local lattice distortion, promotes the formation of oxygen vacancies. These vacancies not only enhance electronic conductivity but also provide effective adsorption and dissociation sites for reaction intermediates in the water splitting process [206]. From a materials science perspective, the crystal structure of Ca-series perovskite oxides offers clear advantages. In water splitting reactions, these oxides generate more oxygen vacancies due to their smaller lattice constant and pronounced local lattice distortions. Oxygen vacancies are crucial for catalysis as they significantly lower the energy barrier for water dissociation, enhance the conductivity of the catalyst, and improve the efficiency of the electrocatalytic process [207]. Compared to other perovskite oxides, Ca-series perovskites exhibit strong stability, particularly in acidic or alkaline media, with excellent corrosion resistance and durability. Additionally, the electronic structure of B-site transition metals in Ca-series perovskite oxides remains stable during water splitting, maintaining strong oxidation-reduction capabilities and promoting efficient electron transfer during the OER. Therefore, the unique structural features of Ca-series perovskite oxides, particularly their oxygen vacancy regulation and optimized redox properties of the transition metals, make them highly advantageous for efficient electrocatalytic water splitting.

Building on the above discussion of Ca-based perovskite structures, recent work has explored how tuning oxygen deficiency and lattice symmetry can enhance their electrocatalytic activity. Zhang et al. synthesized an oxygen-deficient orthorhombic perovskite $Ca_2Mn_2O_5$ using a solid-state reaction method to investigate the intrinsic relationship between crystal structure and water-splitting performance [170]. As shown in Figure 8A, the HRTEM and FFT images reveal submicron-sized, well-crystallized $Ca_2Mn_2O_5$ particles with distinct lattice fringes, confirming the formation of a highly ordered perovskite framework. Figure 8B displays the unit cell configuration of $Ca_2Mn_2O_5$, where oxygen vacancies are periodically arranged along directions normal to the *ab* plane. These ordered vacancies generate lattice distortions, improve electronic conductivity, and act as active centers that facilitate the adsorption and conversion of oxygen intermediates during the oxygen evolution reaction. As presented in Figure 8C, the iR-corrected polarization curves show that $Ca_2Mn_2O_5$/C exhibits a significantly lower overpotential of approximately 370 mV at 10 mA cm^{-2}, outperforming $CaMnO_3$/C and Vulcan carbon, which require overpotentials exceeding 430 mV and 500 mV, respectively. This remarkable enhancement demonstrates that ordered vacancy engineering within the orthorhombic perovskite lattice effectively modulates charge transport and reaction kinetics, leading to improved catalytic activity and long-term stability during water splitting. Building on the understanding of oxygen-vacancy ordering in Ca-based perovskites, Yagi et al. synthesized a cubic quadruple perovskite $CaCu_3Fe_4O_{12}$ (CCFO) using a high-pressure solid-state reaction method to investigate the influence of covalency reinforcement on electrocatalytic behavior [180]. As shown in Figure 8D, CCFO exhibits a well-ordered cubic perovskite structure in which Ca, Cu, and Fe ions occupy distinct lattice sites, forming a highly stable and interconnected framework conducive to efficient redox processes. Figure 8E presents the three-dimensional electron density distribution, revealing a continuous Fe–O–Cu covalent network that facilitates electron delocalization and enhances charge-transfer kinetics within the lattice. Figure 8F demonstrates that CCFO retains nearly constant current density after 100 consecutive OER cycles, confirming its superior structural integrity and long-term durability. These results collectively indicate that the reinforced Fe–O–Cu covalent bonding network within the cubic CCFO lattice plays a decisive role in maintaining high catalytic stability and sustained water-splitting performance. Building upon the structural insights gained from covalency-enhanced Ca-based perovskites, Fan et al. synthesized a cubic quadruple perovskite $CaCu_3Co_2Ru_2O_{12}$ (CCCRO) via a high-pressure solid-state reaction method to elucidate the structural and electronic factors governing its exceptional oxygen evolution reaction (OER) activity [183]. As illustrated in Figure 8G, the crystal structural model demonstrates a highly ordered cubic perovskite lattice in which Ca, Cu, Co, and Ru ions occupy distinct A- and B-site positions, forming a robust and symmetric framework conducive to efficient charge transport and redox cycling. Figure 8H presents an atomic-resolution HAADF-STEM image that clearly visualizes the periodic arrangement of atomic columns along the (001) plane, confirming the excellent crystallinity and structural stability of CCCRO. Figure 8I shows the corresponding Tafel plots, where CCCRO achieves a notably low slope of 37 mV dec^{-1}, indicative of rapid reaction kinetics and superior catalytic efficiency. These findings demonstrate that the synergistic interactions among Cu, Co, and Ru ions within the cubic perovskite lattice effectively regulate the electronic structure and strengthen the lattice stability, thereby achieving enhanced electrocatalytic activity and durability in water-splitting reactions.

Gd-series perovskite oxides exhibit unique crystal structural characteristics that contribute to their enhanced catalytic activity and stability in electrocatalytic water splitting. The Gd^{3+} ion, with a relatively small ionic radius of approximately 1.05 Å, induces higher lattice strain compared to La^{3+}, resulting in a more distorted lattice structure in the perovskite oxides. These materials typically adopt the ABO_3-type crystal structure, where Gd^{3+} occupies the A-site, and transition metals such as iron or cobalt occupy the B-site. Due to the smaller ionic radius of Gd^{3+}, the lattice constant of Gd-based perovskite oxides typically ranges from 3.78 Å to 3.83 Å, demonstrating significant lattice distortion. This lattice distortion creates favorable conditions for the formation of oxygen vacancies, which act as catalytic centers, significantly enhancing the OER in water splitting. Oxygen vacancies not only accelerate the redox reaction rate but also optimize the adsorption behavior of reaction intermediates by adjusting the surface electronic structure, thereby lowering the reaction energy barriers. Furthermore, the strong lattice distortion and smaller ionic radius of Gd result in a relatively higher surface defect density, which plays a crucial role in modulating the electronic environment of B-site transition metals. For example, the doping of Gd at the A-site helps modulate the oxidation states and coordination environments of B-site metals, thereby improving the electrocatalytic performance of these oxides. Studies have shown that Gd-based perovskite oxides exhibit enhanced catalytic efficiency in water splitting, as the oxygen vacancies not only lower the reaction energy barriers but also optimize the adsorption strength of reaction intermediates. Gd doping plays a pivotal role in improving the surface electronic structure, promoting effective interaction and electron transfer between reactants and catalysts. These structural characteristics enable Gd-series perovskite oxides to demonstrate distinct advantages, particularly in the OER, leading to significant improvements in catalytic efficiency and stability. Understanding these structure-performance relationships provides valuable theoretical insights for the development of highly efficient electrocatalysts for water splitting.

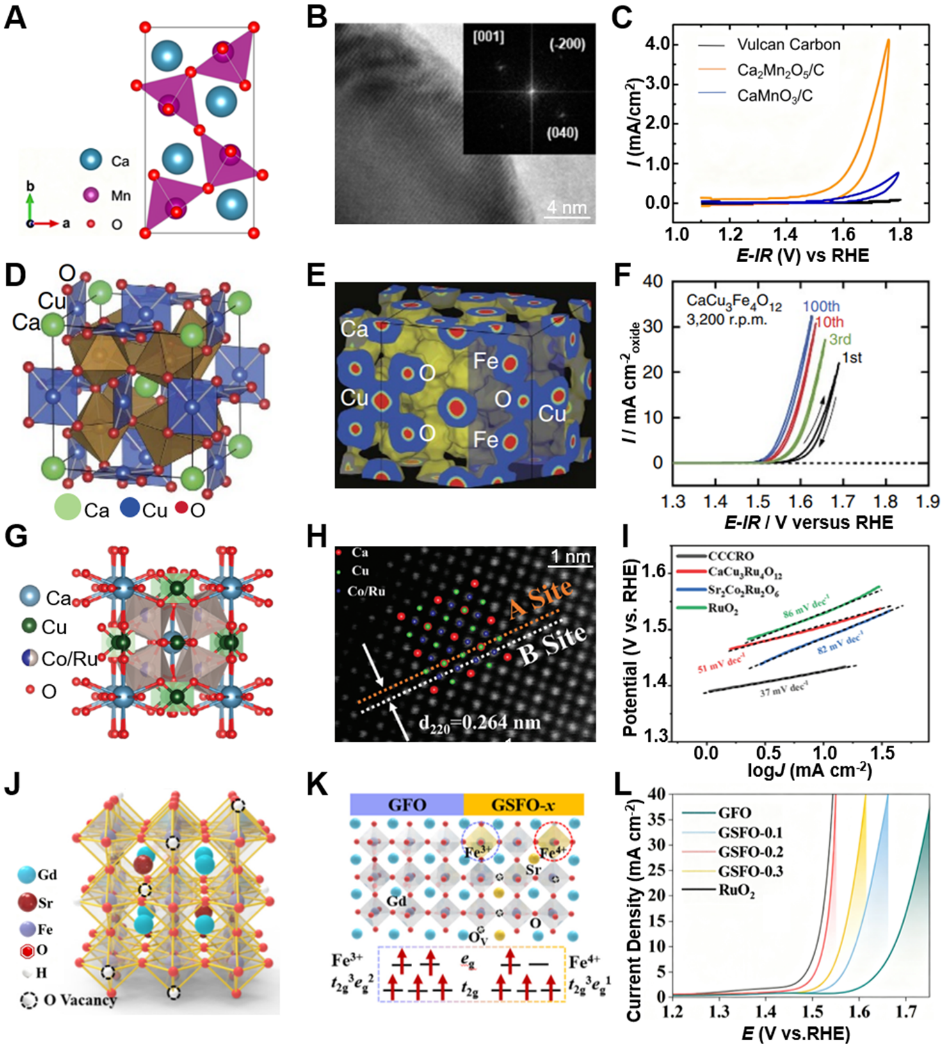

Figure 8. Structural regulation of Ca- and Gd-based perovskite oxides enhances lattice distortion and oxygen-vacancy activity for improved water-splitting electrocatalysis. (**A**) Crystal structure of orthorhombic $Ca_2Mn_2O_5$ with ordered oxygen vacancies. (**B**) HRTEM and FFT pattern confirming orthorhombic phase. (**C**) Polarization curves of $Ca_2Mn_2O_5$/C and $CaMnO_3$/C showing enhanced OER activity [170]. Reproduced with permission from Ref. [170]. Copyright 2014, American Chemical Society. (**D**) Crystal structure of cubic $CaCu_3Fe_4O_{12}$. (**E**) Electron density map showing Fe–O–Cu bonding. (**F**) LSV curves exhibiting stable OER activity over 100 cycles [180]. Reproduced with permission from Ref. [180]. Copyright 2015, Springer Nature. (**G**) Crystal structure of cubic $CaCu_3Co_2Ru_2O_{12}$. (**H**) HAADF-STEM image showing A/B-site ordering of Co and Ru in the lattice (d_{220} = 0.264 nm). (**I**) Tafel plots demonstrating superior OER activity of CCCRO [183]. Reproduced with permission from Ref. [183]. Copyright 2024, Wiley-VCH GmbH. (**J**) Crystal structure of GSFO-0.2 showing Sr-induced oxygen vacancies. (**K**) Fe^{3+}/Fe^{4+} distribution and oxygen-vacancy formation at the GFO/GSFO-x interface. (**L**) LSV curves showing superior OER activity of GSFO-0.2 [167]. Reproduced with permission from Ref. [167]. Copyright 2023, Elsevier.

Gd-based perovskite oxides exhibit highly tunable lattice structures that enable precise control over their catalytic properties and electrochemical stability. Jiang et al. synthesized a two-dimensional porous $Gd_{0.8}Sr_{0.2}FeO_3$ with an orthorhombic perovskite structure enriched in oxygen vacancies through a microwave-shock strategy, achieving rapid A-site Sr incorporation and controlled 2D porous formation [167]. As shown in Figure 8J, Sr substitution alters the Fe^{3+}/Fe^{4+} spin configuration and induces pronounced lattice distortion, effectively modulating the coordination environment and strengthening Fe–O orbital interactions within the perovskite lattice. Figure 8K illustrates the oxygen-rich vacancy structure, where lattice distortion and defect generation synergistically enhance electronic conductivity, facilitate charge transfer, and optimize the adsorption–desorption kinetics of key OER intermediates (*OH, *O, and *OOH), thus reducing the reaction energy barrier. As presented in Figure 8L, the GSFO-0.2 catalyst delivers an overpotential of 294 mV at 10 mA cm^{-2} and a Tafel slope of 55.85 mV dec^{-1}, demonstrating excellent activity and stability. These results confirm that the defect-engineered orthorhombic lattice with abundant oxygen vacancies fundamentally enhances the intrinsic catalytic performance of Gd-based perovskite oxides for efficient water oxidation.

3.2. B-Site Transition Metal-Based Perovskite Oxides and Their Electrocatalytic Properties

3.2.1. Co-Series Perovskite Oxides

Co-based perovskite oxides constitute a prototypical platform for water splitting catalysis because the Co^{3+}/Co^{4+} redox couple, variable spin states, and strong O 2p–Co 3d covalency jointly tune e_g occupancy, oxygen-defect chemistry, and charge transport in catalytic potential windows. In compositions such as $LaCoO_{3-\delta}$, $SrCoO_{3-\delta}$, $BaCoO_{3-\delta}$, and A-site solid solutions, partial oxidation toward Co^{4+} and controlled creation of oxygen vacancies reduce the energy cost of forming OER intermediates, while enhanced p-type conductivity expedites electron exchange with adsorbates. Crystal symmetry and octahedral tilt patterns regulate Co–O bond lengths, crystal field splitting, and spin crossover, which shift the balance between the adsorbate evolution mechanism and the lattice oxygen mechanism as a function of covalency and vacancy concentration. Under anodic polarization, surface reconstruction typically yields CoOOH-like layers interfaced with an oxygen-deficient perovskite subsurface; this dynamic heterostructure increases active site density and lowers kinetic barriers, provided that A-site leaching and excessive oxygen release are mitigated [208–210]. Design strategies that stabilize high-valent Co without crippling conductivity include A-site tuning to adjust tolerance factor and vacancy thermodynamics, partial B-site substitution with Fe or Ni to modulate Co–O bandwidth and suppress deleterious phase collapse, and heteroanion regulation with limited sulfate, phosphate, or fluoride incorporation to restrain overreconstruction. Strain engineering and epitaxial control further tailor Co–O hybridization and oxygen exchange coefficients, enabling high intrinsic OER activity at reduced overpotentials with improved turnover stability. For bifunctional operation, coupling Co perovskites with conductive carbons or nitrides enhances HER kinetics by improving proton/electron delivery and by providing complementary adsorption energetics, while core–shell or gradient architectures protect the perovskite lattice during high current operation. Within these structure–property guidelines, Co-series perovskite oxides offer a coherent route to co-engineer electronic structure, defect landscapes, and interfacial dynamics for efficient and durable electrocatalysis.

Building on previous evidence that lattice symmetry strongly influences the catalytic behavior of Co-based perovskites, this study investigates how dopant regulation affects phase stability and OER performance. Wygant et al. employed a polymerized complex method followed by high-temperature annealing to synthesize Fe- and Sc-doped $SrCoO_{3-\delta}$ perovskites with stabilized cubic symmetry, achieving improved electronic conductivity and structural robustness conducive to enhanced catalytic operation [152]. The cubic $SrCoO_{3-\delta}$ lattice (Figure 9A) consists of corner-sharing CoO_6 octahedra surrounding Sr^{2+} ions, forming a highly ordered framework that supports efficient Co^{3+}/Co^{4+} redox transitions and facilitates rapid charge transport, thereby reinforcing both mechanical and electronic integrity. The HRTEM image of 10% Fe–SCO (Figure 9B) reveals that Fe incorporation effectively stabilizes the cubic lattice, reduces octahedral distortion, and enhances crystallinity, while the redox-active nature of Fe further optimizes electron delocalization and catalytic turnover. In contrast, the polarization curves of Sc-doped samples (Figure 9C) indicate that the current density reaches 10 mA cm^{-2} at approximately 1.65 V versus RHE, suggesting that although Sc incorporation preserves cubic symmetry, its redox-inert character restricts further enhancement of oxygen evolution activity. Building upon the dopant-regulated phase tuning discussed earlier, Oh et al. designed a heterostructured catalyst by integrating perovskite $La_{0.5}Sr_{0.5}CoO_{3-\delta}$ (LSC) with potassium-intercalated $MoSe_2$ (K-$MoSe_2$), achieving synergistic electronic interactions that improve overall water-splitting activity [189]. The HR-TEM image of the LSC/K-$MoSe_2$ composite (Figure 9D) displays a distinct heterojunction between the perovskite and 1T-phase $MoSe_2$ domains, where coherent lattice alignment facilitates efficient interfacial electron transfer and strengthens Co–O–Se coupling within the catalytic interface. The high-resolution image of LSC (Figure 9E) reveals a well-ordered lattice with clearly defined (110) and (001) planes, confirming high crystallinity and stable CoO_6 octahedral coordination that support effective charge transport and redox reversibility. Correspondingly, the Tafel plots (Figure 9F) demonstrate that the LSC/K-$MoSe_2$ heterostructure exhibits a notably smaller slope of 45 mV dec^{-1} compared with pristine LSC, verifying that the optimized interfacial electronic configuration accelerates hydrogen evolution kinetics and enhances intrinsic catalytic performance. Building on the interfacial coupling strategy demonstrated in the LSC/K-$MoSe_2$ system, Hao et al. synthesized oxygen-deficient brownmillerite-type $SrCoO_{2.52}$, a layered perovskite phase characterized by alternating octahedral and tetrahedral Co–O units that promote lattice flexibility and oxygen mobility [27]. The *in situ* reconstruction process (Figure 9G) demonstrates that this brownmillerite $SrCoO_{2.52}$ gradually transforms into a spinel Co_3O_4 layer under anodic polarization, where controlled A-site leaching and oxygen vacancy generation facilitate lattice oxygen activation and efficient charge transfer. The HAADF-STEM image (Figure 9H) further shows atomically dispersed Ru single atoms uniformly anchored within the Co_3O_4/CoOOH lattice, stabilizing the reconstructed framework and maintaining Co–O coordination during OER operation. Correspondingly, the Tafel plots (Figure 9I) reveal a remarkably low slope of approximately 33 mV dec^{-1}, confirming that the dynamic transformation from the brownmillerite perovskite to a spinel–oxyhydroxide interface effectively accelerates oxygen evolution kinetics and enhances the intrinsic catalytic activity. Building on the reconstruction-driven activation observed in $SrCoO_{2.52}$ systems, Expanding upon the concept of structural and interfacial coupling introduced in previous studies, Lu et al. developed a two-dimensional perovskite oxide/MXene heterostructure ($La_{0.9}Sr_{0.1}CoO_3$/$Ti_3C_2T_x$ on Ni foam) that integrates light-assisted evaporation with electrocatalytic water splitting to achieve synergistic performance enhancement [163]. The XRD pattern (Figure 9J) confirms that the $La_{0.9}Sr_{0.1}CoO_3$ nanosheets retain a well-defined perovskite lattice with hexagonal R-3m symmetry, indicating high crystallinity and structural integrity after integration with MXene, where the hexagonal perovskite–MXene interface optimizes lattice symmetry and charge exchange pathways to support efficient catalytic reactions. The polarization curves (Figure 9K) reveal that the LMN heterostructure requires only 279 mV of overpotential to deliver 10 mA cm^{-2}, demonstrating that the perovskite–MXene coupling effectively enhances charge transport and interfacial reaction kinetics under solar illumination. The corresponding Tafel plots (Figure 9L) show a reduced slope of 74.3 mV dec^{-1}, indicating that the strong interfacial electronic interaction between the perovskite and MXene layers accelerates oxygen evolution kinetics and ensures superior catalytic efficiency and long-term stability.

3.2.2. Ni-Series Perovskite Oxides

Ni-based perovskite oxides leverage the Ni^{3+}/Ni^{4+} redox couple, high O 2p–Ni 3d covalency, and tunable e_g occupancy to realize favorable scaling of intermediate binding and rapid hole transport under OER-relevant potentials, while offering compositional routes to stabilize active high-valent states. In archetypes such as $LaNiO_3$, $SrNiO_3$, $BaNiO_{3-\delta}$, and A-site solid solutions, partial substitution by alkaline-earth cations raises the average Ni valence toward $Ni^{3.5+}$–Ni^{4+}, compresses Ni–O bond lengths, and widens the 3d–2p bandwidth, effects that elevate p-type conductivity and place the e_g filling near unity, a regime correlated with low OER overpotentials and enhanced turnover. Octahedral tilt patterns and tolerance-factor-controlled symmetry govern crystal-field splitting and charge-transfer energy, thereby modulating vacancy formation enthalpy and oxygen exchange kinetics that dictate whether adsorbate evolution or lattice-oxygen participation predominates. Under anodic bias in alkaline media, surface reconstruction typically generates NiOOH-rich layers coherently coupled to an oxygen-deficient perovskite subsurface; this graded interface increases active-site density and facilitates proton-coupled electron transfer, yet excessive A-site leaching or overoxidation can induce amorphization and performance decay. Rational design emphasizes co-doping at the B site with Fe or Co to tune covalency and suppress deleterious oxygen release, heteroanion regulation with limited F, S, or P incorporation to restrain overreconstruction, and strain or epitaxial control to adjust Ni–O hybridization and vacancy diffusivity without sacrificing conductivity [211]. For bifunctional devices, coupling Ni perovskites with conductive scaffolds or integrating metallic Ni/NiOx nanophases can accelerate alkaline HER by improving water dissociation and electron delivery, while core–shell or layered heterostructures protect the perovskite framework at high current densities. Within these structure–property principles, Ni-series perovskite oxides provide a versatile platform in which valence chemistry, defect landscapes, and interfacial dynamics can be co-optimized to achieve intrinsically active and durable electrocatalysis.

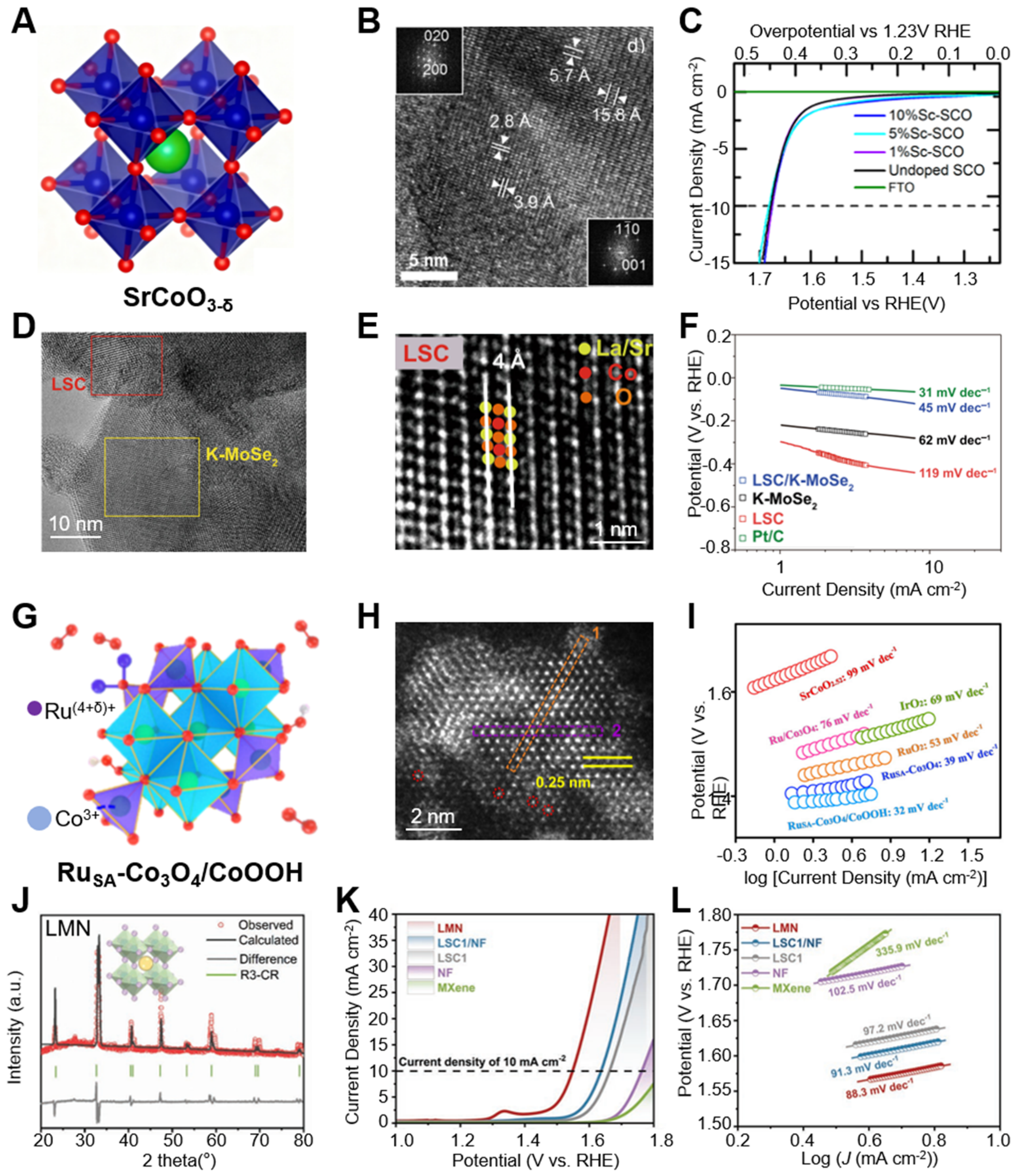

Figure 9. Structural modulation of Co-based perovskite oxides strengthens lattice distortion–activity coupling, directly linking crystal structure to enhanced electrocatalytic performance. (**A**) Crystal structure of cubic $SrCoO_{3-\delta}$. (**B**) HRTEM image and corresponding FFT patterns confirming the coexistence of orthorhombic and cubic $SrCoO_{3-\delta}$ domains. (**C**) LSV curves of Sc-doped $SrCoO_{3-\delta}$ with enhanced OER activity [152]. Reproduced with permission from Ref. [152]. Copyright 2016, American Chemical Society. (**D**) HRTEM image of the LSC/K-$MoSe_2$ interface. (**E**) HAADF-STEM image of LSC with 4 Å lattice spacing. (**F**) Tafel plots showing enhanced HER activity of LSC/K-$MoSe_2$ [189]. Reproduced with permission from Ref. [189]. Copyright 2021, Springer Nature. (**G**) Schematic illustration of Ru single-atom anchored spinel–perovskite Ru_{sa}–Co_3O_4/CoOOH interface derived from perovskite oxide. (**H**) HAADF-STEM image showing atomic Ru incorporation at the perovskite–spinel boundary. (**I**) Tafel plots confirming enhanced OER activity from perovskite–spinel coupling [27]. Reproduced with permission from Ref. [27]. Copyright 2024, Royal Society of Chemistry. (**J**) XRD pattern confirming the R-3m phase of LMN perovskite. (**K**) LSV curves showing enhanced OER activity of LMN at 10 mA cm^{-2}. (**L**) Tafel plots indicating improved kinetics of the LMN–MXene heterostructure [163]. Reproduced with permission from Ref. [163]. Copyright 2023, Wiley-VCH GmbH.

Building on the preceding discussion of Ni-based perovskites, this section further investigates the effect of crystal symmetry evolution on catalytic efficiency. Fan et al. prepared a series of $La_{0.7}Sr_{0.3}Fe_{1-x}Ni_xO_{3-\delta}$ perovskites through a glycine–nitrate combustion method, achieving a gradual transition from the rhombohedral to cubic structure as the Ni content increased [39]. The HRTEM image and FFT pattern in Figure 10A clearly display the well-ordered cubic lattice of LSFN-0.4 along the [001] zone axis, confirming the formation of a highly symmetrical phase with uniform atomic arrangement that inherently promotes better electronic conduction. The crystal structure comparison in Figure 10B reveals that Ni substitution straightens the TM–O–TM bond angles and enhances orbital overlap, strengthening electronic coupling and improving bulk conductivity, which collectively underpin the superior charge-transfer efficiency observed in the EIS results of Figure 10C, where the cubic LSFN-0.4 exhibits markedly lower resistance and faster interfacial electron transport. This progressive enhancement of structural symmetry and charge transport manifests in the IR-corrected OER polarization curves of Figure 10D, where LSFN-0.4 achieves an overpotential of 320 mV at 10 mA cm^{-2} and a Tafel slope of 35 mV dec^{-1}, demonstrating that the cubic phase formed via Ni incorporation provides intrinsic advantages for highly efficient and stable OER catalysis. Building on the compositional modulation achieved in La–Sr–Fe–Ni systems, Wu et al. employed a microwave shock strategy to achieve ultrafast phase engineering of 2D $LaNiO_3$ perovskites, enabling structural transformation within seconds and stabilizing a highly ordered cubic phase [148]. As shown in Figure 10E, this rapid heating–cooling process effectively reconstructs the lattice, generating uniform atomic ordering and enlarged interlayer spacing that promote efficient electron delocalization. The schematic in Figure 10F reveals that the expanded interlayer distance reduces charge-transfer energy and strengthens Ni 3d–O 2p orbital hybridization, thereby improving charge mobility and facilitating surface redox reactions. The Tafel plots in Figure 10G further demonstrate that the cubic $LaNiO_3$ phase achieves a low Tafel slope of 33.1 mV dec^{-1} and a small onset potential, indicative of accelerated electron transfer and enhanced reaction kinetics. These results underscore that microwave-induced phase reconstruction, by enhancing lattice symmetry and electronic coupling, provides an effective pathway for optimizing the intrinsic activity and stability of perovskite electrocatalysts. Extending the understanding of phase-controlled $LaNiO_3$ systems, Sharma et al. employed a pulsed laser deposition method to fabricate epitaxial $LaNiO_{3-\delta}$ thin films with controlled (001), (110), and (111) crystal orientation**s**, allowing precise adjustment of surface atomic configurations [182]. The structural representation in Figure 10I shows that the (111)-oriented film possesses nonadjacent Ni–O planes, forming an open lattice configuration that promotes efficient adsorption and activation of oxygen intermediates. The cyclic voltammetry profiles in Figure 10J exhibit a distinct Ni redox transition near 1.4 V vs. RHE on the (111) facet, suggesting its stronger tendency to form catalytically active NiOOH species under operating potentials. The polarization and stability results in Figure 10K indicate that the (111) facet delivers a low overpotential of 0.45 V at 1 mA cm^{-2} and maintains consistent performance during repeated galvanostatic holds. These findings demonstrate that facet-controlled epitaxial growth, through the regulation of atomic arrangement and lattice symmetry, significantly enhances electron transport, surface reactivity, and structural stability, providing deeper insight into the crystallographic optimization of perovskite oxide electrocatalysts. Building on the facet-dependent modulation of $LaNiO_{3-\delta}$ thin films, Forslund et al. synthesized a series of $La_{0.5}Sr_{1.5}Ni_{1-x}Fe_xO_{4\pm\delta}$ compounds with a well-defined tetragonal I4/mmm structure via a modified Pechini route, enabling precise control over cation distribution and structural uniformity [36]. As shown in Figure 10L, the 2 × 2 × 1 unit cell reveals the ordered stacking of perovskite and rock-salt layers with evenly distributed La in the [001] AO planes, while the electron diffraction pattern in Figure 10M confirms the absence of cation or anion ordering, evidencing high crystallinity and phase purity. The cyclic voltammetry curves in Figure 10N exhibit a distinct anodic shift of the $Ni^{2+/3+}$ redox peak with increasing Fe content, indicating that Fe incorporation effectively adjusts the Ni–O–Fe electronic interaction and enhances charge-transfer capability. The OER polarization data in Figure 10O demonstrate that the optimized $LSNF_{30}$ composition achieves an overpotential of 360 mV at 10 mA cm^{-2} and a Tafel slope of 44 mV dec^{-1}, highlighting that Fe substitution within the layered RP framework enhances orbital hybridization, electronic conductivity, and lattice stability, thereby promoting efficient and durable oxygen evolution catalysis.

3.2.3. Fe-Series Perovskite Oxides

Fe-series perovskite oxides exhibit significant catalytic performance in electrocatalytic water splitting, driven by their unique crystal structure and chemical properties. These oxides adopt the ABO_3-type structure, where larger cations, such as La^{3+} or Sr^{2+}, occupy the A-site, and iron (Fe^{3+} or Fe^{2+}) occupies the B-site. Iron ions possess distinctive electronic structures and oxidation-reduction properties, which play a critical role in catalysis during water splitting reactions [212]. In Fe-series perovskite oxides, the valence state change of Fe (Fe^{3+}/Fe^{2+}) is one of the key factors influencing electrocatalytic performance. During the catalytic process, Fe^{3+} can undergo electron transfer and react with reactants in water, facilitating the OER. Additionally, the lattice constant of Fe-based perovskites typically ranges from 3.85 Å to 3.90 Å, exhibiting moderate lattice symmetry and a relatively loose lattice structure, which favors the formation of oxygen vacancies and increases the number of active catalytic sites. From a materials science perspective, the crystal structure of Fe-series perovskite oxides offers significant advantages for electrocatalysis. The coordination environment of Fe ions at the B-site can be modified by doping A-site cations or through local lattice distortions, thus affecting the oxidation-reduction activity of Fe. In water splitting reactions, Fe-perovskite oxides increase catalytic activity by creating more oxygen vacancies and enhancing surface defect density [213]. Oxygen vacancies not only improve charge transfer properties but also enhance the adsorption and dissociation of reaction intermediates, thereby lowering reaction energy barriers [214]. Furthermore, the oxidation-reduction performance of Fe ions plays a pivotal role in water splitting, accelerating the dissociation of water molecules and promoting OER. Fe-series perovskite oxides demonstrate high catalytic stability and corrosion resistance over a wide pH range, making them suitable for long-term use in practical applications. By optimizing the electron density distribution in the crystal structure and adjusting the coordination environment of the B-site metal, Fe-series perovskite oxides enhance their electrocatalytic performance, providing robust support for efficient water splitting.

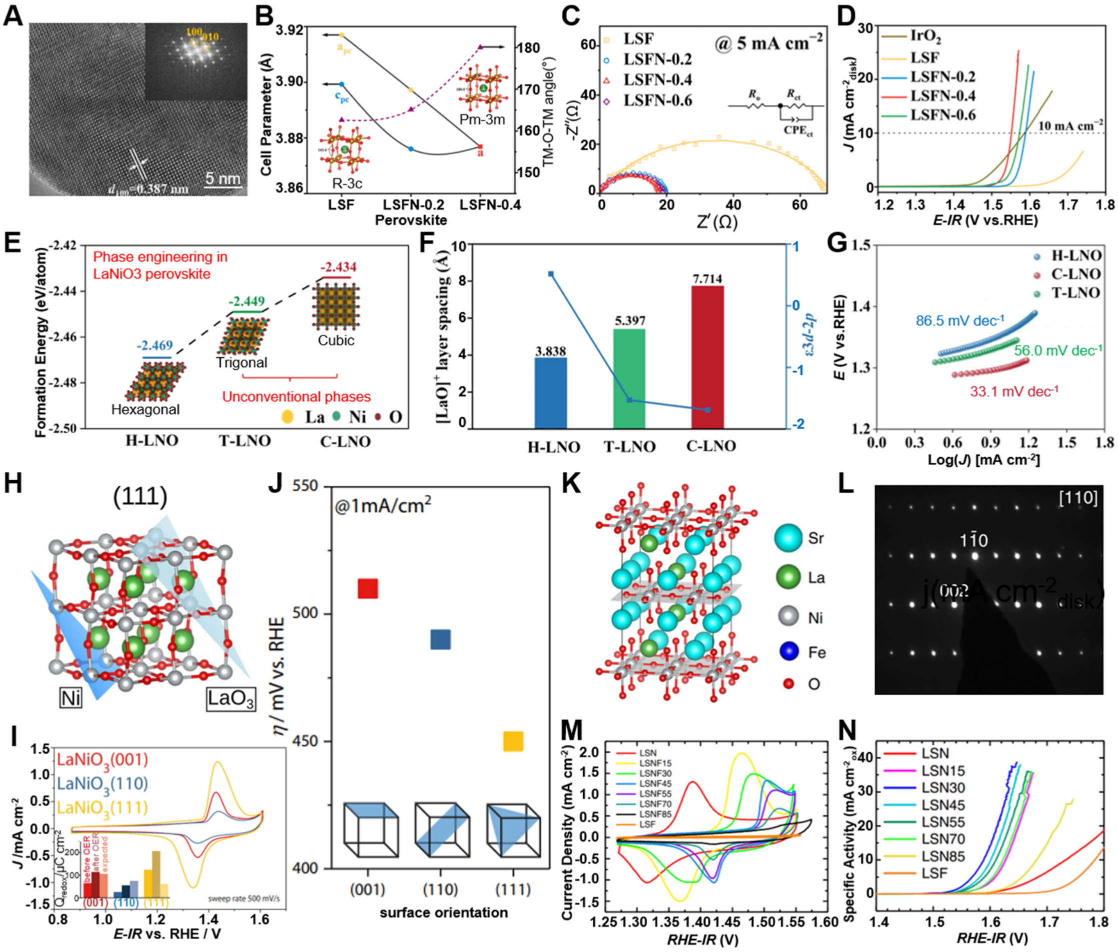

Figure 10. Structural and phase regulation of Ni-based perovskite oxides optimizes electronic configuration and lattice distortion, thereby enhancing their intrinsic electrocatalytic activity for overall water splitting. (**A**) HRTEM image of LSFN-0.4 perovskite showing clear lattice fringes. (**B**) Crystal structure evolution from rhombohedral to cubic phase upon Ni doping. (**C**) Nyquist plots showing reduced charge-transfer resistance of LSFN-0.4. (**D**) LSV curves confirming enhanced OER activity of LSFN-0.4 [39]. Reproduced with permission from Ref. [39]. Copyright 2021, Elsevier. (**E**) Phase evolution of $LaNiO_3$ perovskite from hexagonal to trigonal and cubic structures. (**F**) Variation in $[LaO]^+$ layer spacing and Ni 3d–O 2p hybridization among different phases. (**G**) Tafel plots confirming enhanced catalytic kinetics of cubic $LaNiO_3$.[148] Reproduced with permission from Ref. [148]. Copyright 2024, Wiley-VCH GmbH. (**H**) Atomic structure of $LaNiO_3$ perovskite with exposed (111) facet. (**I**) Cyclic voltammetry curves of $LaNiO_3$ thin films with (001), (110), and (111) orientations. (**J**) Overpotentials at 1 mA cm^{-2} showing that the (111) facet exhibits the highest OER activity [182]. Reproduced with permission from Ref. [182]. Copyright 2023, Springer Nature. (**K**) Crystal structure of layered $La_{0.5}Sr_{1.5}Ni_{1-x}Fe_xO_{4+\delta}$ perovskite illustrating Ruddlesden–Popper stacking. (**L**) Electron diffraction pattern along [110] confirming ordered lattice of $LSNF_{30}$. (**M**) Cyclic voltammetry curves showing Fe substitution–induced redox enhancement. (**N**) LSV plots revealing improved OER activity of Fe-doped LSNF perovskite.[36] Reproduced with permission from Ref. [36]. Copyright 2018, Springer Nature.

Building upon the intrinsic redox adaptability and oxygen-vacancy tunability of Fe-based perovskite oxides, further enhancement of their electrocatalytic performance has been achieved through precise structural and compositional engineering. Xu et al. synthesized Si-doped $SrFeO_{3-\delta}$ perovskites ($SrFe_{1-x}Si_xO_{3-\delta}$) via a conventional solid-state reaction, obtaining a cubic crystalline phase that exhibited distinct structural and electronic advantages for the oxygen evolution reaction [154]. As illustrated in Figure 11A, Si incorporation induced a tetragonal-to-cubic phase transition, accompanied by modulation of Fe–O coordination and oxygen-vacancy distribution, which collectively optimized the Fe oxidation state and enhanced charge-transfer dynamics, thereby accelerating oxygen evolution kinetics. The HR-TEM and SAED analyses (Figure 11B) confirmed the formation of the highly ordered cubic $SrFe_{0.9}Si_{0.1}O_{3-\delta}$ lattice, featuring well-defined (110) and (001) lattice fringes and distinct diffraction patterns. Correspondingly, the Tafel plots (Figure 11C) revealed that the cubic SFSi catalyst possessed a significantly lower Tafel slope (58 mV dec^{-1}) and nearly threefold higher OER activity compared to the undoped $SrFeO_{3-\delta}$, underscoring that Si-induced crystallographic transformation effectively optimizes lattice symmetry and electronic configuration to promote superior electrocatalytic performance. Similarly, Zhao et al. prepared double perovskite $PrBa_{0.5}Sr_{0.5}Co_{1.5}Fe_{0.5}O_{5+\delta}$ (PBSCF) nanofibers via a precise electrospinning–calcination route, successfully forming a well-defined orthorhombic layered double perovskite structure that exhibits superior catalytic activity and exceptional structural robustness toward the oxygen evolution reaction [179]. As shown in Figure 11D, the incorporation of Sr and Fe into the $PrBaCo_2O_{5+\delta}$ (PBC) lattice and the ordered A-site cation arrangement along the ***c***-axis induce lattice modulation and oxygen-vacancy redistribution, generating a highly stable orthorhombic framework that facilitates efficient electron and ion transport while enhancing charge-transfer kinetics and lattice integrity. The unit-cell schematic (Figure 11E) further reveals the alternating Pr/Ba/Sr and Co/Fe–O layers, confirming the ordered double-perovskite configuration that stabilizes the lattice and optimizes the oxidation states of the B-site cations. The high-resolution TEM image (Figure 11F) demonstrates that after prolonged ultrasonic treatment and 12 h of chronopotentiometric testing at 10 mA cm^{-2}, the PBSCF-III nanofiber maintained its ordered orthorhombic structure without surface amorphization, underscoring the critical role of crystallographic integrity and double-perovskite ordering in achieving durable and high-performance Fe-based electrocatalysts. In continuation of the lattice modulation observed in PBSCF double perovskites, Weng et al. fabricated epitaxial $SrFeO_{3-\delta}$ single-crystal thin films with distinct topotactic phases using pulsed laser deposition (PLD) to elucidate the relationship between lattice structure and electronic configuration in oxygen evolution catalysis [186]. As shown in Figure 11G, the atomic schematic of the infinite-layer $SrFeO_{2.0}$ (IL-SFO) film grown on the $SrTiO_3$ (001) substrate displays a planar FeO_4 coordination and an ordered oxygen-deficient lattice formed through controlled topotactic reduction, yielding a highly crystalline phase with tunable Fe–O bonding geometry that enables precise coordination tailoring and orientation control to regulate the electronic structure and reaction pathway. The linear sweep voltammetry (LSV) curves (Figure 11H) demonstrate that within the $SrFeO_{3-\delta}$ series, the brownmillerite $SrFeO_{2.5}$ (BM-SFO) phase achieves the most favorable OER performance, characterized by a low overpotential of 390 mV at 1 mA cm^{-2} and a small Tafel slope, attributed to its ordered oxygen-vacancy channels that facilitate efficient charge and ion transport. Furthermore, the orientation-dependent analysis (Figure 11I), closely related to the atomic configuration shown in Figure 11G, reveals that the (111)-oriented BM-SFO thin film exhibits the highest catalytic activity, as the alignment of Fe–O tetrahedra and oxygen-vacancy planes along this orientation enhances e_g orbital occupancy and Fe–O hybridization, thereby establishing a direct link between atomic coordination, crystallographic orientation, and oxygen evolution efficiency. In continuation of the orientation-dependent modulation demonstrated in $SrFeO_{3-\delta}$ thin films, Hua et al. designed a La/Ca co-doped perovskite nanorod catalyst with a stable cubic structure, formulated as $La_{0.5}(Ba_{0.4}Sr_{0.4}Ca_{0.2})_{0.5}Co_{0.8}Fe_{0.2}O_{3-\delta}$ (L-0.5), to enable efficient overall water splitting under alkaline conditions [157]. As illustrated in Figure 11J, the STEM-HAADF and HRTEM images reveal highly crystalline L-0.5 nanorods exhibiting distinct lattice fringes and ordered atomic arrangements characteristic of the cubic Pm-3m phase, confirming uniform A-site cation distribution and robust structural coherence. The optimized cubic lattice enhances e_g orbital occupancy, maintains balanced oxygen vacancies, and promotes rapid charge and ion transport, collectively contributing to superior intrinsic activity. The IR-corrected LSV curves (Figure 11K) further demonstrate that the L-0.5/rGO hybrid catalyst delivers remarkable HER performance, characterized by low overpotential and rapid kinetics comparable to Pt-based catalysts. These findings emphasize that preserving a well-ordered cubic framework and homogeneous cation arrangement is essential for achieving high charge-transfer efficiency and long-term catalytic durability in Fe-based perovskite electrocatalysts.

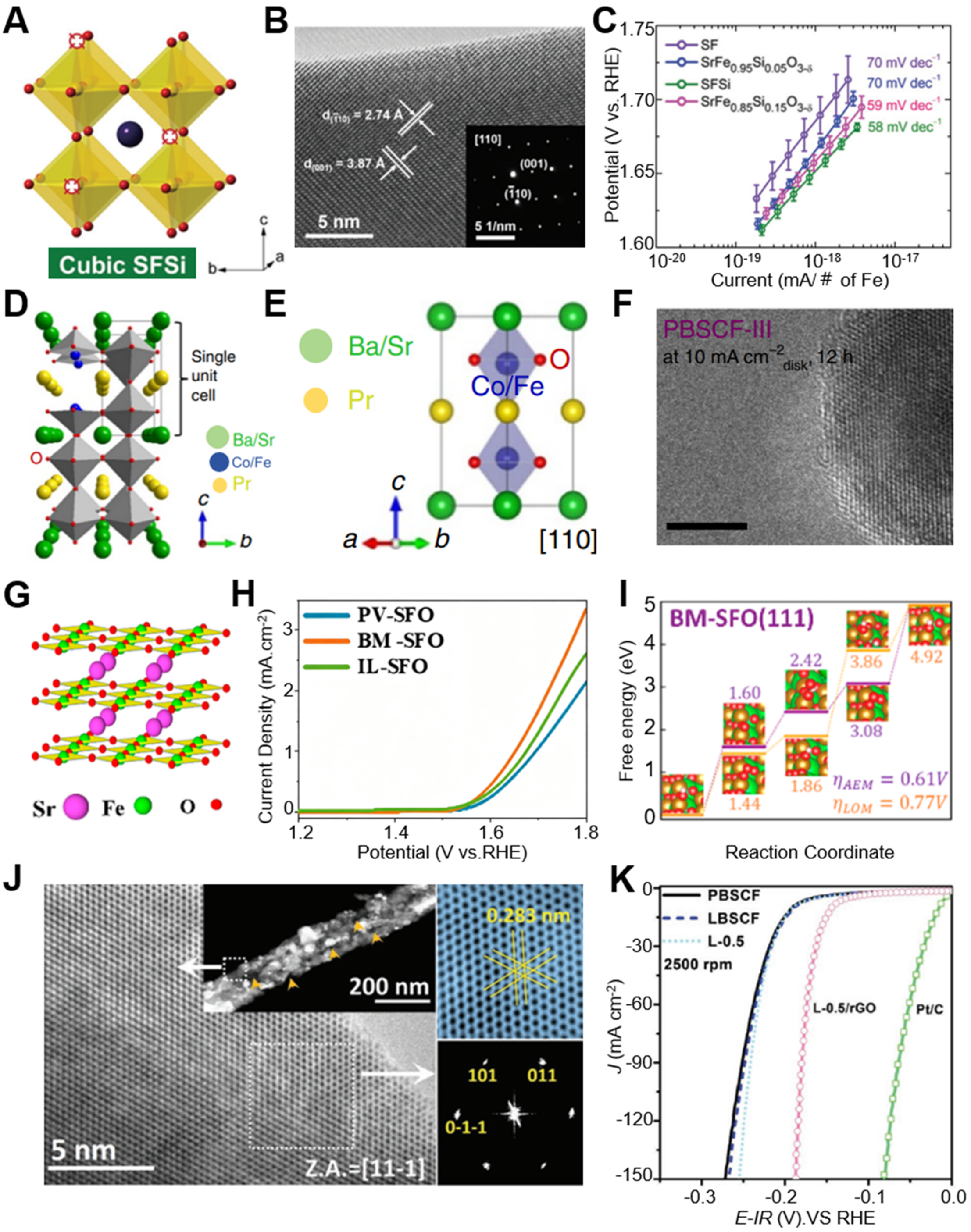

Figure 11. Structural tuning of Fe-based perovskite oxides enhances lattice oxygen activity and boosts electrocatalytic performance. (**A**) Cubic structure of Si-doped SrFe$_{0.9}$Si$_{0.1}$O$_{3-\delta}$ perovskite. (**B**) HR-TEM and SAED confirm cubic phase with (110) and (001) planes. (**C**) SFSi shows a smaller Tafel slope (58 mV dec^{-1}) and improved OER activity [154]. Reproduced with permission from Ref. [154]. Copyright 2018, WILEY-VCH Verlag GmbH & Co. KGaA. (**D**) Crystal structure of double perovskite PrBa$_{0.5}$Sr$_{0.5}$Co$_{1.5}$Fe$_{0.5}$O$_{5+\delta}$ (PBSCF) with ordered A-site cations and corner-sharing Co/FeO$_6$ octahedra. (**E**) Atomic model along [110] showing layered arrangement of Pr and Ba/Sr planes. (**F**) HRTEM image of PBSCF-III after 12 h OER at 10 mA cm^{-2} confirming preserved lattice order [179]. Reproduced with permission from Ref. [179]. Copyright 2017, Springer Nature. (**G**) Crystal structure of brownmillerite SrFeO$_{2.5}$ with alternating FeO$_6$/FeO$_4$ layers. (**H**) LSV curves of PV-, BM-, and IL-SFO showing enhanced OER activity for BM-SFO. (**I**) Free-energy profile of BM-SFO (111) revealing lower overpotential via lattice oxygen pathway [186]. Reproduced with permission from Ref. [186]. Copyright 2023, American Chemical Society. (**J**) HRTEM image of perovskite nanostructures with clear lattice fringes and FFT confirming crystallinity along [1$\bar{1}$1]. (**K**) LSV curves showing superior HER performance of L-0.5/rGO compared with L-0.5, PBSF, and LBSF [157]. Reproduced with permission from Ref. [157]. Copyright 2017, WILEY-VCH Verlag GmbH & Co. KGaA.

3.2.4. Mn- and Cr-Series Perovskite Oxides

Mn-based perovskite oxides derive catalytic behavior from the Mn^{3+}/Mn^{4+} redox couple, Jahn–Teller activity of high-spin Mn^{3+}, and a defect chemistry that readily furnishes oxygen vacancies while preserving appreciable p-type transport. In systems typified by $LaMnO_{3-\delta}$, $CaMnO_{3-\delta}$, $SrMnO_{3-\delta}$, and Ba-substituted analogues, octahedral tilt patterns and A-site size modulate Mn–O bond lengths, crystal-field splitting, and the balance between cooperative Jahn–Teller distortion and itinerancy, which in turn govern e_g occupancy and the energetics for forming OER intermediates. Increased average Mn valence toward $Mn^{3.5+}$–Mn^{4+} narrows the charge-transfer gap and strengthens O 2p–Mn 3d hybridization, improving hole conductivity and lowering barriers for *OH and *O formation, while moderate nonstoichiometry introduces labile vacancies that accelerate hydroxide adsorption and oxygen exchange [215]. Under anodic polarization in alkaline media, surfaces frequently reconstruct into MnOOH or mixed $MnO_x(OH)_y$ layers coherently coupled to an oxygen-deficient perovskite subsurface; this graded interface elevates active-site density and enables partial lattice-oxygen participation when covalency and vacancy concentration cross critical thresholds, although excessive oxidation can trigger Mn dissolution and amorphization. Performance optimization centers on stabilizing high-valent Mn without suppressing transport by A-site tuning to adjust tolerance factor and vacancy thermodynamics, B-site alloying with Ni, Co, or Fe to regulate bandwidth and suppress deep-trap states, and strain or epitaxial control to temper Jahn–Teller distortion while enhancing oxygen diffusivity. Within such constraints, Mn-series perovskites offer a cost-effective route to robust OER catalysts that balance intrinsic activity with acceptable durability, and they can serve as bifunctional components when coupled to HER-active phases that assist water dissociation and electron delivery [216].

Following the general discussion of Mn-based perovskite systems, attention has been directed toward tailoring lattice distortion and vacancy ordering to optimize catalytic behavior. Wang et al. used a reductive annealing approach to prepare a layered double perovskite $NdBaMn_2O_{5.5}$, which converts the disordered cubic $Nd_{0.5}Ba_{0.5}MnO_{3-\delta}$ into an ordered orthorhombic phase with alternating Nd–O and Ba–O layers [171]. As illustrated in Figure 12A, this ordered structure, composed of alternating MnO_6 octahedra and MnO_5 square pyramids, induces distinct Mn^{3+}/Mn^{4+} coordination and strong lattice distortion that promote Mn–O covalency and accelerate charge transfer. The high-resolution TEM image in Figure 12B reveals a well-defined crystalline lattice and clear vacancy ordering, confirming the structural stability under electrochemical conditions. The OER polarization curves in Figure 12C show that this optimized phase exhibits an intrinsic activity over twenty times higher than RuO_2 at 1.7 V vs. RHE, demonstrating the significant advantage of vacancy-ordered layered structures for achieving high-efficiency and durable bifunctional water splitting. Building on the vacancy ordering achieved in layered Mn perovskites, Ji et al. utilized a sol–gel synthesis method to prepare a Ca-doped high-entropy perovskite $La_{0.6}Ca_{0.4}(CrMnFeCo_2Ni)O_3$, which crystallizes into a single-phase cubic framework exhibiting uniform cation dispersion and enhanced structural stability [155]. As illustrated in Figure 12D, the selected-area electron diffraction pattern presents sharp diffraction rings, confirming the high crystallinity and ordered lattice symmetry of the synthesized oxide. The high-resolution TEM image in Figure 12E reveals distinct lattice fringes corresponding to the (100) and (110) planes, reflecting coherent crystallinity and minimal defect propagation across the lattice. The polarization LSV curves in Figure 12F demonstrate that this optimized phase delivers a low overpotential of approximately 340 mV at 10 mA cm^{-2} and maintains excellent operational stability, indicating that Ca incorporation and high configurational entropy synergistically regulate lattice distortion and oxygen-vacancy concentration to enhance charge transport and sustain long-term electrocatalytic efficiency. Building on the structural modulation achieved in Ca-doped high-entropy Mn-based perovskites**,** Zhang et al. prepared tetragonal $LaMn_{0.5}Ni_{0.5}O_{3-\delta}$ (t-LMON) nanocrystals through a sol–gel calcination strategy, enabling precise control over cation distribution and structural distortion [169]. As shown in Figure 12G, the high-resolution TEM image exhibits distinct and periodic lattice fringes characteristic of the tetragonal phase, confirming well-defined crystallinity and coherent lattice ordering. The corresponding SAED pattern in Figure 12H presents sharp and regularly arranged diffraction spots, further validating the long-range structural order and uniform orientation of t-LMON grains. The OER polarization curves in Figure 12I reveal that this tetragonal perovskite achieves a substantially lower overpotential and improved kinetic response compared with IrO_2, underscoring that the lattice distortion intrinsic to the tetragonal phase strengthens Mn/Ni–O hybridization, optimizes e_g orbital occupancy, and facilitates charge transfer, thereby enhancing oxygen-evolution activity and ensuring structural stability under operational conditions.

Cr-based perovskite oxides exhibit catalytic characteristics dictated by the Cr^{3+}/Cr^{4+} redox manifold, strong crystal-field stabilization of $t_{2}g^{3}$ configurations, and comparatively strong Cr–O bonds that raise vacancy formation enthalpy while conferring notable structural resilience. Representative compositions such as $LaCrO_3$, $CaCrO_3$, $SrCrO_3$, and aliovalently doped derivatives display lower intrinsic p-type conductivity than Ni- or Co-based analogues, yet benefit from high lattice stability and resistance to overreconstruction under OER bias [217].

Electronic structure features, including a deeper O 2p band center and greater charge-transfer energy, favor adsorbate evolution pathways over extensive lattice-oxygen participation, placing a premium on optimizing intermediate binding at surface Cr sites through covalency enhancement rather than exploiting aggressive oxygen nonstoichiometry. Design strategies that elevate activity include A-site substitution with Sr or Ba to increase tolerance factor and bandwidth, limited B-site alloying with Fe, Ni, or Co to raise covalency and introduce itinerant carriers without compromising the Cr–O framework, and heteroanion regulation that tailors surface acidity and inhibits deleterious phase change. Under alkaline operation, surface layers often stabilize as CrOOH-like terminations with restrained A-site leaching, yielding steady catalytic kinetics at moderate overpotentials and sustained operation at high pH. When integrated into heterostructures that supply conductive scaffolds and water dissociation promoters, Cr-series perovskites contribute exceptional durability and corrosion resistance, enabling device architectures in which activity is co-delivered by adjunct phases while the perovskite core preserves mechanical and chemical integrity at elevated current densities.

Building on prior insights into Cr-based perovskite oxides, entropy engineering offers further structural optimization. Kante et al. synthesized an epitaxial high-entropy perovskite oxide film, $LaCr_{0.2}Mn_{0.2}Fe_{0.2}Co_{0.2}Ni_{0.2}O_{3-\delta}$, via pulsed-laser deposition, achieving a single-phase (001)-oriented crystalline structure with exceptional lattice coherence and compositional uniformity [156]. As illustrated in Figure 12J, the STEM image reveals a sharply defined interface between the P-HEO layer and the $SrTiO_3$ substrate, confirming coherent epitaxial growth and high crystallinity. The magnified TEM view in Figure 12K further displays uniformly distributed atomic columns and homogeneous elemental dispersion, verifying that configurational entropy effectively stabilizes the ordered perovskite lattice. The cyclic voltammetry data in Figure 12L show that the P-HEO achieves an outstanding OER performance, delivering up to 17-fold higher current density than $LaNiO_3$ and over 680-fold higher than $LaCrO_3$ at an overpotential of 450 mV, with a Tafel slope of 51 mV dec^{-1}. These results demonstrate that multicationic synergy within the Cr-based perovskite lattice enhances B–O covalency, accelerates charge transfer, and yields superior catalytic stability under alkaline conditions.

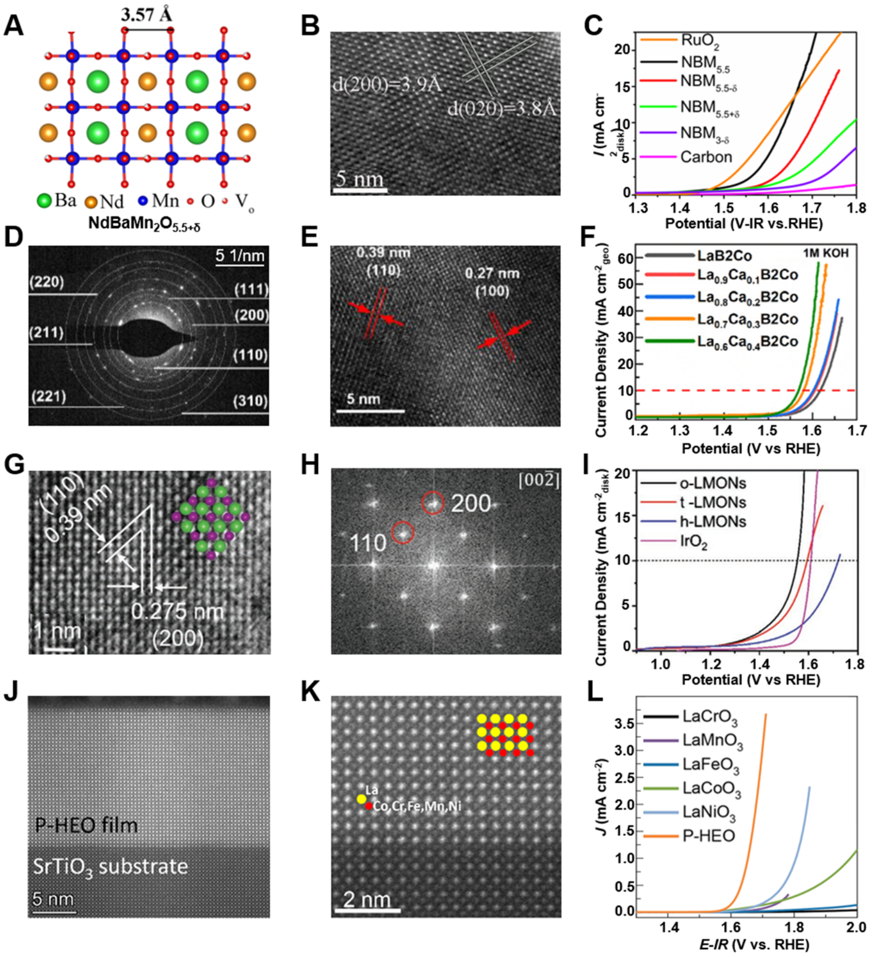

Figure 12. Phase tuning of Mn- and Cr-based perovskite oxides enhances lattice distortion and improves electrocatalytic activity. (**A**) Crystal structure of layered double perovskite $NdBaMn_2O_{5.5+\delta}$ with ordered oxygen vacancies in Nd–O layers. (**B**) HRTEM image confirming orthorhombic lattice structure and high crystallinity. (**C**)

LSV curves showing enhanced OER activity of $NBM_{5.5}$ over oxygen-deficient and oxygen-rich counterparts [171]. Reproduced with permission from Ref. [171]. Copyright 2018, American Chemical Society. (**D**) SAED pattern of $La_{0.6}Ca_{0.4}$ $(CrMnFeCo_2Ni)O_3$ showing cubic perovskite diffraction rings. (**E**) HRTEM image revealing (110) and (100) lattice fringes of 0.39 nm and 0.27 nm. (**F**) LSV curves of $La_{1-x}Ca_xB_2Co$ series, with $La_{0.6}Ca_{0.4}B_2Co$ showing the best OER activity in 1 M KOH [155]. Reproduced with permission from Ref. [155]. Copyright 2024, Elsevier. (**G**) HRTEM lattice fringes of orthorhombic $LaMnO_3$ nanosheets, 0.39 nm (110) and 0.275 nm (200) spacing. (**H**) SAED pattern of o-LMONs along [002] orientation, characteristic of ordered perovskite lattice. (**I**) Polarization curves of o-, t-, and h-phase $LaMnO_3$, enhanced OER activity of orthorhombic phase [169]. Reproduced with permission from Ref. [169]. Copyright 2021, Wiley-VCH GmbH. (**J**) Cross-sectional STEM image of epitaxial P-HEO film on $SrTiO_3$ substrate with coherent lattice. (**K**) Atomic-resolution HAADF-STEM image showing uniformly distributed multication B-site. (**L**) OER polarization curves of $LaBO_3$ and P-HEO, enhanced activity of high-entropy perovskite film [156]. Reproduced with permission from Ref. [156]. Copyright 2023, American Chemical Society.

4. Summary, Challenges, and Perspectives

This review examines perovskite oxides for electrocatalytic water splitting with emphasis on how crystalline phase governs performance through lattice symmetry, oxygen-defect thermodynamics, and electronic structure. The analysis first establishes fundamental mechanisms and phase-resolved structural characteristics, then quantifies phase effects on OER and HER kinetics, including the roles of oxygen vacancy distribution, e_g occupancy, metal–oxygen covalency, and surface reconstruction. A comparative survey of A-site families is presented in the sequence La-series, Sr-series, Ba-series, Ca-series, and Gd-series, highlighting tolerance factor control, octahedral tilt patterns, charge-compensation pathways, and their impact on B-site valence and vacancy formation. B-site transition-metal families are subsequently evaluated in the sequence Co-series, Ni-series, Fe-series, Mn-series, and Cr-series, delineating how redox manifolds and orbital configurations regulate intermediate binding and charge-transfer kinetics. A statistical synopsis of reported catalysts consolidates performance parameters across crystal phases and compositions, revealing consistent correlations between near-cubic symmetry, high-valent B-site states, and optimized vacancy chemistries and the attainment of low overpotentials with competitive durability. Collectively, these results provide design guidance for phase engineering, A/B-site modulation, and interface control aimed at high-efficiency perovskite electrocatalysts.

Despite substantial advances, critical challenges continue to limit translation of perovskite oxides to robust water-splitting devices. The first centers on phase controllability and metastability under operando conditions. Narrow synthesis windows, coupled with tolerance-factor-driven octahedral tilts and defect equilibria, often yield mixed phases or vacancy-ordered intermediates that drift during polarization. Topotactic transformations between perovskite and brownmillerite frameworks tune activity but complicate reproducibility, and phase boundaries introduced by strain or nanostructuring can trigger unintended reconstructions that obscure intrinsic kinetics.

A second challenge lies in governing oxygen-defect chemistry with spatiotemporal precision. Oxygen vacancy concentration, distribution, and mobility co-evolve with B-site valence and metal–oxygen covalency, shaping the balance between adsorbate-evolving pathways and lattice-oxygen participation. Insufficient control invites parasitic oxygen release, deep traps, or electronic localization that elevates overpotentials. Quantitative descriptors linking δ, e_g filling, charge-transfer energy, and oxygen-exchange coefficients to intermediate binding remain incomplete, and deterministic routes to imprint defect gradients or ordered vacancy networks at device-relevant thickness are still nascent.

The third challenge concerns durability and interfacial integrity at high current density. A-site leaching, carbonate uptake in alkaline media, and thickening oxyhydroxide skins can erode crystallographic coherence and conductivity, while repeated redox cycling induces microcracking and loss of percolation in porous electrodes. Stable operation demands suppression of corrosive dissolution, maintenance of electronic and ionic pathways after reconstruction, and compatibility with concentrated electrolytes and gas evolution. Achieving these simultaneously with scalable synthesis, ink processability, and mechanical robustness defines the near-term barrier to deployment.

While substantial progress has been achieved in elucidating correlations between crystallographic symmetry, oxygen defect chemistry, and electrocatalytic performance, future efforts should increasingly emphasize actionable design principles that translate symmetry concepts into practical catalyst engineering. In this context, crystal phase and symmetry engineering emerge as powerful levers to regulate oxygen defect energetics in perovskite oxides. Such control can be realized through several experimentally accessible strategies, including strain engineering via epitaxial growth or interfacial coupling, systematic modulation of A and B-site ionic radii to tune the tolerance factor, and deliberate manipulation of oxygen chemical potential through synthesis conditions or electrochemical polarization. Collectively, these approaches enable the stabilization of metastable or symmetry lowered phases that are otherwise inaccessible under equilibrium conditions, thereby creating expanded design space for optimizing oxygen vacancy formation energies, migration barriers, and surface reactivity. Crucially, crystallographic symmetry and oxygen defect chemistry should be regarded as dynamic descriptors that continuously evolve under realistic electrocatalytic operating conditions, rather than as static attributes defined solely by ex situ characterization. The integration of *in situ* and operando techniques,such as operando X-ray diffraction, X-ray absorption spectroscopy, Raman spectroscopy, and environmental transmission electron microscopy with theoretical modeling provides a critical framework for capturing symmetry evolution, lattice distortion, and oxygen vacancy dynamics in real time. When combined with density functional theory and ab initio thermodynamic analyses, these methodologies can establish quantitative relationships among applied potential, local chemical environment, symmetry modulation, and defect energetics, thereby advancing a predictive understanding of structure activity relationships in perovskite electrocatalysts. From an application oriented perspective, a central challenge lies in preserving symmetry derived defect advantages under industrially relevant current densities, where large overpotentials, localized heating, and vigorous gas evolution can drive surface reconstruction, vacancy over accumulation, or irreversible phase transformations. Such processes may induce symmetry collapse or defect saturation, ultimately degrading catalytic activity and long term stability. Addressing these issues will require the development of symmetry stabilized catalyst architectures, operando informed design rules, and durability centered evaluation protocols that explicitly account for dynamic structural evolution. Bridging the gap between fundamental symmetry defect chemistry and scalable electrocatalytic deployment thus represents a critical frontier for the rational design of next generation perovskite water splitting catalysts.

Author Contributions

L.Z.: Conceptualization, formal analysis, data curation, writing—original draft; J.F.: conceptualization, formal analysis, data curation, writing—original draft; K.Z.: formal analysis, data curation, software, writing—original draft; L.G.: conceptualization, data curation; W.X.: funding acquisition; H.W.: formal analysis, software, writing—review & editing; J.W.: conceptualization, formal analysis, funding acquisition, supervision, validation, writing—review & editing. All authors have read and agreed to the published version of the manuscript.

Funding

The authors acknowledge financial support from the National Natural Science Foundation of China (52203070), the Natural Science Foundation of Hubei Province (2025AFB863), and the Opening Project of Hubei Key Laboratory of Biomass Fibers and Eco-Dyeing & Finishing (STRZ202518).

Institutional Review Board Statement

Not applicable.

Informed Consent Statement

Not applicable.

Data Availability Statement

The data are available from the corresponding author on reasonable request.

Conflicts of Interest

The authors declare no conflict of interest.

Use of AI and AI-Assisted Technologies

No AI tools were utilized for this paper.

References

1. Wang, L.; Yuan, Z.-Y. Elevating Electrode Catalyst Stabilization for Long-Term Intermittent Alkaline Seawater Electrolysis. *Smart Mater. Devices* **2025**, *1*, 202527.
2. Zheng, Y.; Ma, M.; Shao, H. Recent Advances in Efficient and Scalable Solar Hydrogen Production through Water Splitting. *Carbon Neutrality* **2023**, *2*, 23.

3. Cai, J.; Wu, Z.; Wang, S.; et al. Exploring Advanced Microwave Strategy for the Synthesis of Two-Dimensional Energy Materials. *Appl. Phys. Rev.* **2024**, *11*, 041320–041331.
4. Li, N.; Cheng, C.; Wang, Y.; et al. Layered Perovskite Materials for Photocatalytic Overall Water Splitting: Recent Advances, Enhanced Strategies, and Future Challenges. *EcoEnergy* **2025**, *3*, e70023.
5. Zhou, P.; Zhao, X.; Song, Y.; et al. pH-Dependent Electrochemical Oxidation of 5-Hydroxymethylfurfural: Reaction Mechanism, Catalyst Design, and Reactor Design Across Alkaline to Acidic Media. *Smart Mol.* **2025**, e70027. https://doi.org/10.1002/smo2.70027.
6. Moon, J.; Beker, W.; Siek, M.; et al. Active Learning Guides Discovery of a Champion Four-Metal Perovskite Oxide for Oxygen Evolution Electrocatalysis. *Nat. Mater.* **2024**, *23*, 108–115.
7. Jiang, C.; He, H.; Guo, H.; et al. Transfer Learning Guided Discovery of Efficient Perovskite Oxide for Alkaline Water Oxidation. *Nat. Commun.* **2024**, *15*, 6301.
8. Rong, C.; Dastafkan, K.; Wang, Y.; et al. Breaking the Activity and Stability Bottlenecks of Electrocatalysts for Oxygen Evolution Reactions in Acids. *Adv. Mater.* **2023**, *35*, 2211884.
9. Xiao, Z.; Xiao, X.; Kong, L.B.; et al. Preparation of MXene-Based Hybrids and Their Application in Neuromorphic Devices. *Int. J. Extrem. Manuf.* **2024**, *6*, 022006.
10. Wang, Y.; Wang, L.; Zhang, K.; et al. Electrocatalytic Water Splitting over Perovskite Oxide Catalysts. *Chin. J. Catal.* **2023**, *50*, 109–125.
11. Sun, X.; Yuan, Y.; Liu, S.; et al. Recent Advances in Perovskite Oxides for Oxygen Evolution Reaction: Structures, Mechanisms, and Strategies for Performance Enhancement. *Adv. Funct. Mater.* **2025**, *35*, 2416705.
12. Bai, Z.; Wang, Z.; Wang, T.; et al. Cation-Vacancy Engineering Modulated Perovskite Oxide for Boosting Electrocatalytic Conversion of Polysulfides. *Adv. Funct. Mater.* **2025**, *35*, 2419105.
13. Li, Z.; Li, M.; Zhu, Z. Perovskite Cathode Materials for Low-Temperature Solid Oxide Fuel Cells: Fundamentals to Optimization. *Electrochem. Energy Rev.* **2022**, *5*, 263–311.
14. Sun, H.; Xu, X.; Song, Y.; et al. Recent Progress in $Sr_2Fe_{1.5}Mo_{0.5}O_{6-\delta}$-Based Multifunctional Materials for Energy Conversion and Storage. *Adv. Funct. Mater.* **2024**, *34*, 2411622.
15. Li, K.; Liu, Z.; Han, X.; et al. Local Defect Engineering Tailored Core-Shell Crystalline Perovskite Oxide@Amorphous Hydroxide Heterostructures Activating Dual-Active Sites for High-Performance Zinc-Air Battery Cathodes. *J. Energy Chem.* **2025**, *111*, 190–201.
16. Wang, X.; Yuan, Z.-Y. Key Requirements for Photocatalysts and Reactor Architectures Toward Large-Scale Hydrogen Generation. *Smart Mater. Devices* **2025**, *1*, 202528.
17. Sun, Y.; Li, R.; Chen, X.; et al. A-Site Management Prompts the Dynamic Reconstructed Active Phase of Perovskite Oxide OER Catalysts. *Adv. Energy Mater.* **2021**, *11*, 2003755.
18. Wan, J.; Wu, Z.; Fang, G.; et al. Microwave-Assisted Exploration of the Electron Configuration-Dependent Electrocatalytic Urea Oxidation Activity of 2D Porous $NiCo_2O_4$ Spinel. *J. Energy Chem.* **2024**, *91*, 226–235.
19. Chu, L.; Shen, H.; Wei, H.; et al. Morphology Engineering of ZnO Micro/Nanostructures Under Mild Conditions for Optoelectronic Application. *Int. J. Miner. Metall. Mater.* **2025**, *32*, 498–503.
20. Du, D.; Zheng, R.; He, M.; et al. A-Site Cationic Defects Induced Electronic Structure Regulation of $LaMnO_3$ Perovskite Boosts Oxygen Electrode Reactions in Aprotic Lithium–Oxygen Batteries. *Energy Storage Mater.* **2021**, *43*, 293–304.
21. Wei, L.; Dai, J.; Qin, S.; et al. Two-Dimensional Materials for High-Current-Density Seawater Electrolysis. *Green Chem.* **2025**, *27*, 8755–8776.
22. Kadi, H.; Bo, L.; Ziqi, T.; et al. Multiscale Simulation in Fuel Cell and Electrolyzer Systems: A Review of Methods, Applications, and Future Prospects. *Sustain. Eng. Novit.* **2025**, *1*, 5.
23. Tian, H.; Zhang, H.; Zhu, Z.; et al. Near-Unity Solar Reflectance and Mid-Infrared Transparency via Microwave-Engineered 2D Y_2O_3 for Passive Radiative Cooling. *J. Mater. Chem. A* **2025**, *13*, 39330–39339.
24. Yao, Q.; Liu, P.; Yang, F.; et al. Ferroelectric Polarization in $Bi_{0.9}Dy_{0.1}FeO_3$/g-C_3N_4 Z-Scheme Heterojunction Boosts Photocatalytic Hydrogen Evolution. *Sci. China Mater.* **2024**, *67*, 3160–3167.
25. Wang, S.; Zhang, T.; Zhang, H.; et al. Multifunctional Polyimide Performance Prediction Based on Explainable Machine Learning. *Smart Mol.* **2025**, *3,* e70020.
26. Li, K.; Li, Y.; Han, X.; et al. Quenching-Induced Surface Reconstruction of Perovskite Oxides Activating Bifunctional Sites Towards Oxygen Electrodes for Recharge Zinc–Air Batteries. *Energy Storage Mater.* **2025**, *78*, 104289.
27. Hao, Y.-R.; Xue, H.; Sun, J.; et al. Achieving Superior Oxygen Evolution of Perovskite via Phase Transition and Electrochemical Reconstruction Strategy. *Energy Environ. Sci.* **2024**, *17*, 4044–4054.
28. Ke, L.; Pang, S.; Long, C.; et al. Quenching-Induced Surface Reconstruction of Perovskite Oxide for Rapid and Durable Oxygen Catalysis. *Chem. Eng. J.* **2023**, *463*, 142509.
29. Qin, S.; Dai, J.; Wang, M.; et al. Unleashing the Potential of Metastable Materials in Electrocatalytic Water Splitting. *ACS Mater. Lett.* **2025**, *7*, 524–543.

30. Xu, K.; Li, M.; Qin, A.; et al. Temperature Self-Regulation, Energy Storage, and Fire Safety Intelligent Wood for Safe and Energy-Efficient Buildings. *EcoEnergy* **2025**, *3,* e70019.
31. Liu, Y.; Liu, J.; Hao, L.; et al. Incorporating Crystalline Smart Materials to Fabricate 4D Printed Photomechanical Actuators with Photovoltaic Performance. *Smart Mol.* **2025**, e70026. https://doi.org/10.1002/smo2.70026.
32. Dai, J.; Xian, J.; Liu, K.; et al. Unconventional Metastable Cubic 2D $LaMnO_3$ for Efficient Alkaline Seawater Oxygen Evolution. *Chin. J. Catal.* **2025**, *74*, 228–239.
33. Ge, Y.; Yong, M.; Zeng, X.; et al. Biomass-Derived Materials for Advanced Vanadium Redox Flow Batteries. *Mater. Futures* **2025**, *4*, 042104.
34. Wang, Y.; Li, P.; Liu, B.; et al. Solid Polymer Electrolytes: Ion Conduction Enhancement and Comprehensive Frontiers. *Mater. Futures* **2025**, *4*, 042103.
35. Lee, J.G.; Hwang, J.; Hwang, H.J.; et al. A New Family of Perovskite Catalysts for Oxygen-Evolution Reaction in Alkaline Media: $BaNiO_3$ and $BaNi_{0.83}O_{2.5}$. *J. Am. Chem. Soc.* **2016**, *138*, 3541–3547.
36. Forslund, R.P.; Hardin, W.G.; Rong, X.; et al. Exceptional Electrocatalytic Oxygen Evolution via Tunable Charge Transfer Interactions in $La_{0.5}Sr_{1.5}Ni_{1-x}Fe_xO_{4\pm\delta}$ Ruddlesden-Popper Oxides. *Nat. Commun.* **2018**, *9*, 3150.
37. Tan, Y.; Jin, H.; Mao, S.S.; et al. Surface Hydrophobicity-Hydrophilicity Switching Induced Interface Heat and Water Transfer Enhancement for High-Efficiency Solar Steam Generation. *Carbon Neutrality* **2023**, *2*, 11.
38. Wu, Z.; Xian, J.; Dai, J.; et al. Microwave-Pulse Synthesis of Tunable 2D Porous Nickel-Enriched $LaMn_xNi_{1-x}O_3$ Solid Solution for Efficient Electrocatalytic Urea Oxidation. *J. Mater. Chem. A* **2024**, *12*, 7047–7057.
39. Fan, L.; Rautama, E.L.; Lindén, J.; et al. Two Orders of Magnitude Enhancement in Oxygen Evolution Reactivity of $La_{0.7}Sr_{0.3}Fe_{1-x}Ni_xO_{3-\delta}$ by Improving the Electrical Conductivity. *Nano Energy* **2022**, *93*, 106794.
40. Enoch, C.M.; Ingavale, S.; Marbaniang, P.; et al. Molten Salt-Directed Synthesis of Strontium Manganese Perovskite Oxide: An Active Electrocatalyst for the Oxygen Reduction Reaction and Oxygen Evolution Reaction. *J. Mater. Chem. A* **2023**, *11*, 21780–21792.
41. Wan, J.; Hu, R.; Li, J.; et al. A Universal Construction of Robust Interface between 2D Conductive Polymer and Cellulose for Textile Supercapacitor. *Carbohydr. Polym.* **2022**, *284*, 119230.
42. Hong, W.T.; Stoerzinger, K.A.; Lee, Y.-L.; et al. Charge-Transfer-Energy-Dependent Oxygen Evolution Reaction Mechanisms for Perovskite Oxides. *Energy Environ. Sci.* **2017**, *10*, 2190–2200.
43. Liu, X.; de Camargo Branco, D.; An, L.; et al. Ultrafast Laser Shock Straining in Chiral Chain 2D Materials: Mold Topology-Controlled Anisotropic Deformation. *Nano Micro Lett.* **2025**, *18*, 83.
44. Yan, Y.; Zhao, C.; Hui, J.; et al. Molecular Nonchemically Amplified Resists Based on Spirobixanthene Backbone: Sulfoxime Oxime Esters versus Sulfonium Salts. *Smart Mol.* **2025**, e70028. https://doi.org/10.1002/smo2.70028.
45. Wexler, R.B.; Gautam, G.S.; Stechel, E.B.; et al. Factors Governing Oxygen Vacancy Formation in Oxide Perovskites. *J. Am. Chem. Soc.* **2021**, *143*, 13212–13227.
46. Wan, J.; Zhang, G.; Jin, H.; et al. Microwave-Assisted Synthesis of Well-Defined Nitrogen Doping Configuration with High Centrality in Carbon to Identify the Active Sites for Electrochemical Hydrogen Peroxide Production. *Carbon* **2022**, *191*, 340–349.
47. Liu, D.; Zhou, P.; Bai, H.; et al. Development of Perovskite Oxide-Based Electrocatalysts for Oxygen Evolution Reaction. *Small* **2021**, *17*, 2101605.
48. Wan, J.; Huang, L.; Wu, J.; et al. Rapid Synthesis of Size-Tunable Transition Metal Carbide Nanodots Under Ambient Conditions. *J. Mater. Chem. A* **2019**, *7*, 14489–14495.
49. Zhao, J.-W.; Li, Y.; Luan, D.; et al. Structural Evolution and Catalytic Mechanisms of Perovskite Oxides in Electrocatalysis. *Sci. Adv.* **2024**, *10*, eadq4696.
50. Ruiying, F.; Lianchao, W.; Xutian, Y.; et al. Defects-Engineered Metal-Organic Frameworks for Supercapacitor Platform. *Sustain. Eng. Novit.* **2025**, *1*, 2.
51. Li, W.; Jiang, K.; Li, Z.; et al. Origin of Improved Photoelectrochemical Water Splitting in Mixed Perovskite Oxides. *Adv. Energy Mater.* **2018**, *8*, 1801972.
52. Li, S.-F.; Zhang, B.-Q.; Wang, Y.-Q.; et al. Enhancing Oxygen Evolution Reaction Performance of Ruddlesden–Popper Perovskite Oxide through Heteroatom Incorporation. *Chem. Eng. J.* **2024**, *491*, 151912.
53. Yu, N.; Ma, Y.; Ren, J.-K.; et al. High Negative Voltage Activating Perovskite Oxide with Bi-Vacancy Synergistic Regulation for Water Oxidation. *Chem. Eng. J.* **2023**, *478*, 147415.
54. Liu, W.; Kawano, K.; Kamiko, M.; et al. Effects of *A*-site Cations in Quadruple Perovskite Ruthenates on Oxygen Evolution Catalysis in Acidic Aqueous Solutions. *Small* **2022**, *18*, 2202439.
55. Wang, L.; Yang, Z.; Bowden, M.E.; et al. Hole-Trapping-Induced Stabilization of Ni^{4+} in $SrNiO_3$/$LaFeO_3$ Superlattices. *Adv. Mater.* **2020**, *32*, 2005003.

56. Nguyen, T.X.; Lee, C.-H.; Sun, J.-H.; et al. Synergistic Modulation of Electronic Structure in High Entropy Perovskite Oxide for Enhanced Bifunctional Oxygen Evolution/Reduction Reactions and Its Mechanistic Insights via In-Situ Analyses and Density Functional Theory Calculation. *Chem. Eng. J.* **2025**, *511*, 161731.
57. Yan, X.; Qi, J.; Wang, H.; et al. Tuning Interlayer and Mixed Vanadium Valences of V_2O_5 via Organic and Inorganic Guests Co-Intercalation Enables Boosted Aqueous Zinc-Ion Storage. *Carbon Neutralization* **2025**, *4*, e70082.
58. Hou, W.; Feng, P.; Guo, X.; et al. Catalytic Mechanism of Oxygen Vacancies in Perovskite Oxides for Lithium–Sulfur Batteries. *Adv. Mater.* **2022**, *34*, 2202222.
59. Wu, C.; Sun, Y.; Wen, X.; et al. Adjusting Oxygen Vacancies in Perovskite $LaCoO_3$ by Electrochemical Activation to Enhance the Hydrogen Evolution Reaction Activity in Alkaline Condition. *J. Energy Chem.* **2023**, *76*, 226–232.
60. Zhu, K.; Wu, T.; Li, M.; et al. Perovskites Decorated with Oxygen Vacancies and Fe–Ni Alloy Nanoparticles as High-Efficiency Electrocatalysts for the Oxygen Evolution Reaction. *J. Mater. Chem. A* **2017**, *5*, 19836–19845.
61. Cai, Z.; Kuru, Y.; Han, J.W.; et al. Surface Electronic Structure Transitions at High Temperature on Perovskite Oxides: The Case of Strained $La_{0.8}Sr_{0.2}CoO_3$ Thin Films. *J. Am. Chem. Soc.* **2011**, *133*, 17696–17704.
62. Lopes, P.P.; Chung, D.Y.; Rui, X.; et al. Dynamically Stable Active Sites from Surface Evolution of Perovskite Materials during the Oxygen Evolution Reaction. *J. Am. Chem. Soc.* **2021**, *143*, 2741–2750.
63. Feng, Y.; Wang, M.; Zhang, H.; et al. Engineering Electrocatalytic Structures Through Molten Salt-Mediated Mechanistic Control. *EcoEnergy* **2025**, *3*, e70022.
64. Guo, H.; Yang, Y.; Yang, G.; et al. Ex Situ Reconstruction-Shaped Ir/CoO/Perovskite Heterojunction for Boosted Water Oxidation Reaction. *ACS Catal.* **2023**, *13*, 5007–5019.
65. Kuanhong, C.; Guangshu, Y.; Mingxuan, L.; et al. Organoselenium Catalyzed Reaction: Sustainable Chemistry from Laboratory to Industry. *Sustain. Eng. Novit.* **2025**, *1*, 1.
66. Du, T.; Zheng, S.; Wu, C.; et al. Zeolite-Based Advanced Battery Separators: Synergistic Innovations in Structure Performance Application. *Carbon Neutralization* **2025**, *4*, e70068.
67. Hu, Y.; Wei, L.; Chen, H.; et al. Quantifying Dynamic Changes of Oxygen Nonstoichiometry and Formation of Surface Phases of $SrCoO_x$ Electrocatalysts by Operando Characterizations. *ACS Nano* **2025**, *19*, 13999–14009.
68. Fabbri, E.; Nachtegaal, M.; Binninger, T.; et al. Dynamic Surface Self-Reconstruction is the Key of Highly Active Perovskite Nano-Electrocatalysts for Water Splitting. *Nat. Mater.* **2017**, *16*, 925–931.
69. Wang, B.; Wu, X.; Jia, S.; et al. Ultrahigh Specific Surface Area Mesoporous Perovskite Oxide Nanosheets with Rare-Earth-Enhanced Lattice Oxygen Participation for Superior Water Oxidation. *J. Mater. Sci. Technol.* **2025**, *227*, 255–261.
70. Boucly, A.; Artiglia, L.; Fabbri, E.; et al. Direct Evidence of Cobalt Oxyhydroxide Formation on a $La_{0.2}Sr_{0.8}CoO_3$ Perovskite Water Splitting Catalyst. *J. Mater. Chem. A* **2022**, *10*, 2434–2444.
71. Cao, L.; Petracic, O.; Wei, X.-K.; et al. Migration Kinetics of Surface Ions in Oxygen-Deficient Perovskite During Topotactic Transitions. *Small* **2021**, *17*, 2104356.
72. Seo, M.H.; Park, H.W.; Lee, D.U.; et al. Design of Highly Active Perovskite Oxides for Oxygen Evolution Reaction by Combining Experimental and ab Initio Studies. *ACS Catal.* **2015**, *5*, 4337–4344.
73. Hao, W.; Huang, G.; Ma, X.; et al. Economical Iron-Based Catalyst Electrode for Highly Stable Catalytic Industrial-Scale Overall Seawater Splitting. *Carbon Neutrality* **2024**, *3*, 37.
74. Xu, Z.; Men, X.; Shan, Y.; et al. Electronic Reconfiguration Induced by Neighboring Exchange Interaction at Double Perovskite Oxide Interface for Highly Efficient Oxygen Evolution Reaction. *Chem. Eng. J.* **2022**, *432*, 134330.
75. Yutong, F.; Jiao, D.; Mingjie, W.; et al. Unraveling Metastable Perovskite Oxides Insights from Structural Engineering to Synthesis Paradigms. *Microstructures* **2025**, *5*, 2025068.
76. Han, R.; Shang, Y.-H.; Yang, Y. Corrigendum: Metallic Glass Roadmap. *Mater. Futures* **2025**, *4*, 049501.
77. Pittkowski, R.; Divanis, S.; Klementová, M.; et al. Engendering Unprecedented Activation of Oxygen Evolution via Rational Pinning of Ni Oxidation State in Prototypical Perovskite: Close Juxtaposition of Synthetic Approach and Theoretical Conception. *ACS Catal.* **2021**, *11*, 985–997.
78. Yongfei, Y.; Guangyu, F.; Miao, F.; et al. Leveraging Novel Microwave Techniques for Tailoring the Microstructure of Energy Storage Materials. *Microstructures* **2024**, *4*, 2024035.
79. Shang, C.; Xiao, X.; Xu, Q. Coordination Chemistry in Modulating Electronic Structures of Perovskite-Type Oxide Nanocrystals for Oxygen Evolution Catalysis. *Coord. Chem. Rev.* **2023**, *485*, 215109.
80. Wang, F.; Zhang, C.; Yang, H. Mixed B-site Ruddlesden-Popper Phase $Sr_2(Ru_xIr_{1-x})O_4$ Enables Enhanced Activity for Oxygen Evolution Reaction. *J. Energy Chem.* **2022**, *70*, 623–629.
81. Zhu, F.; Hou, M.; Du, Z.; et al. Steam-Promoted Symmetry Optimizations of Perovskite Electrodes for Protonic Ceramic Cells. *Energy Environ. Sci.* **2024**, *17*, 7782–7791.
82. Heo, Y.; Choi, S.; Bak, J.; et al. Symmetry-Broken Atom Configurations at Grain Boundaries and Oxygen Evolution Electrocatalysis in Perovskite Oxides. *Adv. Energy Mater.* **2018**, *8*, 1802481.

83. Ye, Z.; Zhang, M.; Deng, J.; et al. An Emerging Liquid-Crystalline Conducting Polymer Thermoelectrics: Opportunities and Challenges. *Nano-Micro Lett.* **2025**, *18*, 82.
84. Li, X.; Wang, X.; Ding, J.; et al. Engineering Active Surface Oxygen Sites of Cubic Perovskite Cobalt Oxides toward Catalytic Oxidation Reactions. *ACS Catal.* **2023**, *13*, 6338–6350.
85. Wei, Y.; Hu, Y.; Da, P.; et al. Triggered Lattice-Oxygen Oxidation with Active-Site Generation and Self-Termination of Surface Reconstruction During Water Oxidation. *Proc. Natl. Acad. Sci. USA* **2023**, *120*, e2312224120.
86. Dai, Y.; He, H.; Ouyang, M.; et al. *In-Operando* X-Ray Imaging for Sobering Examination of Aqueous Zinc Metal Batteries. *Nano Micro Lett.* **2025**, *18*, 85.
87. Dai, J.; Wang, M.; Tian, H.; et al. Microwave Shock-Driven Thermal Engineering of Unconventional Cubic 2D $LaMnO_3$ for Efficient Oxygen Evolution. *J. Mater. Chem. A* **2025**, *13*, 31002–31012.
88. Wang, W.; Yang, Y.; Huan, D.; et al. An Excellent OER Electrocatalyst of Cubic $SrCoO_{3-\delta}$ Prepared by a Simple F-Doping Strategy. *J. Mater. Chem. A* **2019**, *7*, 12538–12546.
89. Bak, J.; Bae, H.B.; Chung, S.-Y. Atomic-Scale Perturbation of Oxygen Octahedra via Surface Ion Exchange in Perovskite Nickelates Boosts Water Oxidation. *Nat. Commun.* **2019**, *10*, 2713.
90. Hong, Y.; Byeon, P.; Bak, J.; et al. Local-Electrostatics-Induced Oxygen Octahedral Distortion in Perovskite Oxides and Insight into the Structure of Ruddlesden–Popper Phases. *Nat. Commun.* **2021**, *12*, 5527.
91. Du, S.B.; Wang, J.; Ma, F.T.; et al. Correlation of Composition, Crystal Structure, Reducibility and Catalytic Oxidation Activity on La-Mn-Ni-O System. *Acta Phys. Chim. Sin.* **1992**, *8*, 630–635.
92. Qin, S.; Dai, J.; Tian, H.; et al. 3D Printing Driving Innovations in Extreme Low-Temperature Energy Storage. *Virtual Phys. Prototyp.* **2025**, *20*, e2459798.
93. Bai, J.; Cheng, W.; Wang, T.; et al. Synergistic Regulation of Lithium Nucleation and Anion-Rich Solvation Structure via Silver Trifluoroacetate Additive for Stable Lithium Metal Anodes. *Smart Mater. Devices* **2025**, *1*, 202534.
94. Etani, H.; Yamada, I.; Ohgushi, K.; et al. Suppression of Intersite Charge Transfer in Charge-Disproportionated Perovskite $YCu_3Fe_4O_{12}$. *J. Am. Chem. Soc.* **2013**, *135*, 6100–6106.
95. Song, J.; Zhu, S.C.; Ning, D.; et al. Defect Chemistry and Transport Properties of Perovskite-Type Oxides $La_{1-x}Ca_xFeO_{3-\delta}$. *J. Mater. Chem. A* **2021**, *9*, 974–989.
96. Olszewska, A.; Du, Z.; Świerczek, K.; et al. Novel $ReBaCo_{1.5}Mn_{0.5}O_{5+\delta}$ (Re: La, Pr, Nd, Sm, Gd and Y) Perovskite Oxide: Influence of Manganese Doping on the Crystal Structure, Oxygen Nonstoichiometry, Thermal Expansion, Transport Properties, and Application as a Cathode Material in Solid Oxide Fuel Cells. *J. Mater. Chem. A* **2018**, *6*, 13271–13285.
97. Jiang, H.; Xian, J.; Hu, R.; et al. Microwave Discharge for Rapid Introduction of Bimetallic-Synergistic Configuration to Conductive Catecholate Toward Long-Term Supercapacitor. *Chem. Eng. J.* **2023**, *455*, 140804.
98. Liu, L.-B.; Tang, Y.-F.; Liu, S.; et al. Unraveling the Trade-Off Between Oxygen Vacancy Concentration and Ordering of Perovskite Oxides for Efficient Lattice Oxygen Evolution. *Adv. Energy Mater.* **2025**, *15*, 2402967.
99. Feng, X.; Fan, Y.; Nomura, N.; et al. Graphene Promoted Oxygen Vacancies in Perovskite for Enhanced Thermoelectric Properties. *Carbon* **2017**, *112*, 169–176.
100. Feng, Z.; Hong, W.T.; Fong, D.D.; et al. Catalytic Activity and Stability of Oxides: The Role of Near-Surface Atomic Structures and Compositions. *Acc. Chem. Res.* **2016**, *49*, 966–973.
101. Wan, J.; Fang, G.; Mi, S.; et al. Metastable 2D Amorphous Nb_2O_5 for Aqueous Supercapacitor Energy Storage. *Chem. Eng. J.* **2024**, *488*, 150912.
102. Yang, H.; Zhu, L.; Li, W.; et al. Lignocellulose-Mediated Gel Polymer Electrolytes Toward Next-Generation Energy Storage. *Nano Micro Lett.* **2025**, *18*, 84.
103. Zuo, S.; Wang, C.; Xia, Z.; et al. Combined Exsolution and Electrodeposition Strategy for Enhancing Electrocatalytic Activity of Ti-Based Perovskite Oxides in Oxygen and Hydrogen Evolution Reactions. *Adv. Sci.* **2025**, *12*, 2410535.
104. Zhang, S.; Wan, Y.; Xu, Z.; et al. Bismuth Doped $La_{0.75}Sr_{0.25}Cr_{0.5}Mn_{0.5}O_{3-\delta}$ Perovskite as a Novel Redox-Stable Efficient Anode for Solid Oxide Fuel Cells. *J. Mater. Chem. A* **2020**, *8*, 11553–11563.
105. Xu, X.; Pan, Y.; Zhong, Y.; et al. New Undisputed Evidence and Strategy for Enhanced Lattice-Oxygen Participation of Perovskite Electrocatalyst through Cation Deficiency Manipulation. *Adv. Sci.* **2022**, *9*, 2200530.
106. Li, L.; Dong, Z.; Xia, T.; et al. A Series of Bifunctional $ReBaCo_2O_{5+\delta}$ Perovskite Catalysts Towards Intermediate-Temperature Oxygen Reduction Reaction and Oxygen Evolution Reaction. *Chem. Eng. J.* **2023**, *468*, 143762.
107. Nguyen, L.T.; Cava, R.J. Hexagonal Perovskites as Quantum Materials. *Chem. Rev.* **2021**, *121*, 2935–2965.
108. Zhao, C.; Zhang, X.; Yu, M.; et al. Cooperative Catalysis Toward Oxygen Reduction Reaction under Dual Coordination Environments on Intrinsic $AMnO_3$-Type Perovskites via Regulating Stacking Configurations of Coordination Units. *Adv. Mater.* **2020**, *32*, 2006145.
109. Yang, X.; Fernández–Carrión, A.J.; Geng, X.; et al. B-site Deficient Hexagonal Perovskites: Structural Stability, Ionic Order-Disorder and Electrical Properties. *Prog. Solid State Chem.* **2024**, *74*, 100459.

110. Huang, J.; Tian, H.; Zhang, H.; et al. Two-Dimensional Materials for Enhanced Mid-Infrared Thermal Management. *2D Mater.* **2025**, *12*, 032003.
111. Fop, S.; Skakle, J.M.S.; McLaughlin, A.C.; et al. Oxide Ion Conductivity in the Hexagonal Perovskite Derivative $Ba_3MoNbO_{8.5}$. *J. Am. Chem. Soc.* **2016**, *138*, 16764–16769.
112. Stitzer, K.E.; Darriet, J.; zur Loye, H.C. Advances in the Synthesis and Structural Description of 2H-Hexagonal Perovskite-Related Oxides. *Curr. Opin. Solid State Mater. Sci.* **2001**, *5*, 535–544.
113. Tang, Z.; Zhang, X.; Huang, D.; et al. Critical Thickness and Its Role in the Spheroidization of Natural Flake Graphite. *Carbon Neutralization* **2026**, *5*, e70079.
114. Huang, Y.; Xiao, H.; He, B.; et al. Probing Trace Pt Incorporated $SrIrO_3$ Perovskite for Efficient and Stable Acidic Water Oxidation. *J. Energy Chem.* **2024**, *99*, 325–334.
115. Wachi, K.; Makizawa, M.; Aihara, T.; et al. Oxygen Defect Engineering of Hexagonal Perovskite Oxides to Boost Catalytic Performance for Aerobic Oxidation of Sulfides to Sulfones. *Adv. Funct. Mater.* **2025**, *35*, 2425452.
116. Fan, M.; Tian, H.; Wu, Z.; et al. Microwave Shock Synthesis of Porous 2D Non-Layered Transition Metal Carbides for Efficient Hydrogen Evolution. *SusMat* **2025**, *5*, e252.
117. Zhou, B.W.; Zhang, J.; Ye, X.B.; et al. Octahedral Distortion and Displacement-Type Ferroelectricity with Switchable Photovoltaic Effect in a $3d^3$-Electron Perovskite System. *Phys. Rev. Lett.* **2023**, *130*, 146101.
118. Christy, M.; Choi, S.; Kwon, J.; et al. The Perfect Imperfections of Perovskite Oxide Catalysts in the Aspect of Defect Equilibria. *Small Sci.* **2025**, *5*, 2400386.
119. Cohen, R.E. Origin of Ferroelectricity in Perovskite Oxides. *Nature* **1992**, *358*, 136–138.
120. Cohen, N.; Diéguez, O. Supertetragonal Phases of Perovskite Oxides: Insights from Electronic Structure Calculations. *Isr. J. Chem.* **2020**, *60*, 833–841.
121. Xu, Z.; Qin, W.; Nisar, M.; et al. Phonon Scattering Engineering via Yb Doping in $SnSe_2$ for Substantially Lowered Thermal Conductivity and Enhanced Thermoelectric Performance. *Carbon Neutralization* **2026**, *5*, e70083.
122. Martin, A.; Khansur, N.H.; Urushihara, D.; et al. Effect of Li on the Intrinsic and Extrinsic Contributions of the Piezoelectric Response in $Li_x(Na_{0.5}K_{0.5})_{1-x}NbO_3$ Piezoelectric Ceramics Across the Polymorphic Phase Boundary. *Acta Mater.* **2024**, *266*, 119691.
123. Martirosyan, M.; Passuti, S.; Masset, G.; et al. Nanoscale Characterization of Atomic Positions in Orthorhombic Perovskite Thin Films. *Small* **2025**, *21*, e02538.
124. Roh, C.J.; Jung, M.-C.; Kim, J.R.; et al. Polar Metal Phase Induced by Oxygen Octahedral Network Relaxation in Oxide Thin Films. *Small* **2020**, *16*, 2003055.
125. Ding, X.; Yang, B.; Leng, H.; et al. Crystal Symmetry Engineering in Epitaxial Perovskite Superlattices. *Adv. Funct. Mater.* **2021**, *31*, 2106466.
126. Wang, G.J.; Xu, T.; Wen, S.; et al. Structure-Dependent Electrocatalytic Activity of $La_{1-x}Sr_xMnO_3$ for Oxygen Reduction Reaction. *Sci. China Chem.* **2015**, *58*, 871–878.
127. Xu, R.; Zhu, Z.; Zhang, H.; et al. Synergistic Material–Structure Engineering for Mid-Infrared Thermal Management in Textiles. *Small* **2025**, *21*, e09257.
128. Fu, J.; Zuo, R. Structural Evidence for the Polymorphic Phase Boundary in $(Na,K)NbO_3$ Based Perovskites Close to the Rhombohedral-Tetragonal Phase Coexistence Zone. *Acta Mater.* **2020**, *195*, 571–578.
129. Zhou, J.S.; Goodenough, J.B. Universal Octahedral-Site Distortion in Orthorhombic Perovskite Oxides. *Phys. Rev. Lett.* **2005**, *94*, 065501.
130. Tahini, H.A.; Tan, X.; Schwingenschlögl, U.; et al. Formation and Migration of Oxygen Vacancies in $SrCoO_3$ and Their Effect on Oxygen Evolution Reactions. *ACS Catal.* **2016**, *6*, 5565–5570.
131. Wang, Q.; Gu, Y.; Zhu, W.; et al. Noble-Metal-Assisted Fast Interfacial Oxygen Migration with Topotactic Phase Transition in Perovskite Oxides. *Adv. Funct. Mater.* **2021**, *31*, 2106765.
132. Li, Z.; Mao, X.; Feng, D.; et al. Prediction of Perovskite Oxygen Vacancies for Oxygen Electrocatalysis at Different Temperatures. *Nat. Commun.* **2024**, *15*, 9318.
133. Yang, Y.; Lu, J.; Zhang, X.; et al. Symmetry-Induced Modulation of Proton Conductivity in Y-Doped $Ba(Zr,Ce)O_3$: Insights from Raman Spectroscopy. *J. Mater. Chem. A* **2024**, *12*, 12599–12608.
134. Huang, J.; Tian, H.; Zhang, H.; et al. Engineering Materials and Structural Paradigms for Mid-Infrared Thermal Management. *Mater. Today Energy* **2025**, *52*, 101944.
135. Prosandeev, S.; Wang, D.; Ren, W.; et al. Novel Nanoscale Twinned Phases in Perovskite Oxides. *Adv. Funct. Mater.* **2013**, *23*, 234–240.
136. Chen, L.; Yuan, Z.-Y. Electrocatalytic Alcohol and Aldehyde Oxidation: Advances in Catalysts and Reaction Mechanisms for Sustainable Chemical Synthesis. *Smart Mater. Devices* **2025**, *2*, 202531.
137. Surta, T.W.; Whittle, T.A.; Wright, M.A.; et al. One Site, Two Cations, Three Environments: S^2 and s^0 Electronic Configurations Generate Pb-Free Relaxor Behavior in a Perovskite Oxide. *J. Am. Chem. Soc.* **2021**, *143*, 1386–1398.

138. Peña, M.A.; Fierro, J.L.G. Chemical Structures and Performance of Perovskite Oxides. *Chem. Rev.* **2001**, *101*, 1981–2018.
139. Hu, R.; Jiang, H.; Xian, J.; et al. Microwave-Pulse Sugar-Blowing Assisted Synthesis of 2D Transition Metal Carbides for Sustainable Hydrogen Evolution. *Appl. Catal. B: Environ.* **2022**, *317*, 121728.
140. Li, W.; Chen, L.; Wang, D.; et al. Defect Engineering via Ag and Na Co-Doping in Wide-Bandgap CIGS: From Interfacial Suppression to Bulk Enhancement. *Mater. Futures* **2025**, *4*, 045105.
141. Cheng, Y.; Wang, Y.; Shi, Z.; et al. Recent Progress in Advanced Design of Iridium-Based and Ruthenium-Based Perovskite Catalysts for Acidic Oxygen Evolution Reaction. *EcoEnergy* **2025**, *3*, 131–155.
142. Zhou, H.; Zou, W.; Gu, S.; et al. Multimodal Intelligence in Chemical Discovery: Integrating Interpretable ML, Autonomous Robotics, and Edge Computing. *Sustain. Eng. Novit.* **2025**, *1*, 4.
143. Li, J.; Du, Y.; Wang, K. Exceptionally Durable CO_2 Photoreduction Mediated by Defect-Engineered $CaIn_2S_4$ Nanoflowers. *EcoEnergy* **2025**, *3*, e70020.
144. Li, H.; Chen, Y.; Seow, J.Z.Y.; et al. Surface Reconstruction of Perovskites for Water Oxidation: The Role of Initial Oxides' Bulk Chemistry. *Small Sci.* **2022**, *2*, 2100048.
145. Jung, J.-I.; Park, S.; Kim, M.-G.; et al. Tunable Internal and Surface Structures of the Bifunctional Oxygen Perovskite Catalysts. *Adv. Energy Mater.* **2015**, *5*, 1501560.
146. Riva, M.; Kubicek, M.; Hao, X.; et al. Influence of Surface Atomic Structure Demonstrated on Oxygen Incorporation Mechanism at a Model Perovskite Oxide. *Nat. Commun.* **2018**, *9*, 3710.
147. Fang, G.; Ma, X.; Hu, R.; et al. Horizontally Oriented 2D Skin Structures on Fiber Interface for Long-Life Flexible Energy Storage Devices. *Chem. Eng. J.* **2025**, *509*, 161557.
148. Wu, Z.; Fan, M.; Jiang, H.; et al. Harnessing the Unconventional Cubic Phase in 2D $LaNiO_3$ Perovskite for Highly Efficient Urea Oxidation. *Angew. Chem. Int. Ed.* **2025**, *64*, e202413932.
149. Xu, X.; Su, C.; Zhou, W.; et al. Co-Doping Strategy for Developing Perovskite Oxides as Highly Efficient Electrocatalysts for Oxygen Evolution Reaction. *Adv. Sci.* **2016**, *3*, 1500187.
150. Yu, Z.-Y.; Duan, Y.; Kong, Y.; et al. General Synthesis of Tube-Like Nanostructured Perovskite Oxides with Tunable Transition Metal–Oxygen Covalency for Efficient Water Electrooxidation in Neutral Media. *J. Am. Chem. Soc.* **2022**, *144*, 13163–13173.
151. Hu, R.; Wei, L.; Xian, J.; et al. Microwave Shock Process for Rapid Synthesis of 2D Porous $La_{0.2}Sr_{0.8}CoO_3$ Perovskite as an Efficient Oxygen Evolution Reaction Catalyst. *Acta Phys. Chim. Sin.* **2023**, *39*, 2212025.
152. Wygant, B.R.; Jarvis, K.A.; Chemelewski, W.D.; et al. Structural and Catalytic Effects of Iron- and Scandium-Doping on a Strontium Cobalt Oxide Electrocatalyst for Water Oxidation. *ACS Catal.* **2016**, *6*, 1122–1133.
153. Kim, U.; Lee, S.; Koo, D.; et al. Crystal Facet and Electronic Structure Modulation of Perovskite Oxides for Water Oxidation. *ACS Energy Lett.* **2023**, *8*, 1575–1583.
154. Xu, X.; Chen, Y.; Zhou, W.; et al. Earth-Abundant Silicon for Facilitating Water Oxidation over Iron-Based Perovskite Electrocatalyst. *Adv. Mater. Interfaces* **2018**, *5*, 1701693.
155. Ji, X.; Yang, F.; Du, Y.; et al. Highly Active and Durable $La_{0.6}Ca_{0.4}(CrMnFeCo_2Ni)O_3$ High Entropy Perovskite Oxide as Electrocatalyst for Oxygen Evolution Reaction in Alkaline Media. *J. Mater. Sci. Technol.* **2024**, *168*, 71–78.
156. Kante, M.V.; Weber, M.L.; Ni, S.; et al. A High-Entropy Oxide as High-Activity Electrocatalyst for Water Oxidation. *ACS Nano* **2023**, *17*, 5329–5339.
157. Hua, B.; Li, M.; Zhang, Y.-Q.; et al. All-In-One Perovskite Catalyst: Smart Controls of Architecture and Composition Toward Enhanced Oxygen/Hydrogen Evolution Reactions. *Adv. Energy Mater.* **2017**, *7*, 1700666.
158. Li, S.; Xia, T.; Dou, Y.; et al. Phosphatizing Engineering of Perovskite Oxide Nanofibers for Hydrogen Evolution Reaction to Achieve Extraordinary Electrocatalytic Performance. *Adv. Funct. Mater.* **2022**, *32*, 2112164.
159. Hua, B.; Li, M.; Pang, W.; et al. Activating p-Blocking Centers in Perovskite for Efficient Water Splitting. *Chem* **2018**, *4*, 2902–2916.
160. Dai, J.; Zhu, Y.; Tahini, H.A.; et al. Single-Phase Perovskite Oxide with Super-Exchange Induced Atomic-Scale Synergistic Active Centers Enables Ultrafast Hydrogen Evolution. *Nat. Commun.* **2020**, *11*, 5657.
161. Xu, X.; Pan, Y.; Zhong, Y.; et al. From Scheelite $BaMoO_4$ to Perovskite $BaMoO_3$: Enhanced Electrocatalysis Toward the Hydrogen Evolution in Alkaline Media. *Compos. Part B Eng.* **2020**, *198*, 108214.
162. Zhang, L.; Jang, H.; Li, Z.; et al. $SrIrO_3$ Modified with Laminar Sr_2IrO_4 as a Robust Bifunctional Electrocatalyst for Overall Water Splitting in Acidic Media. *Chem. Eng. J.* **2021**, *419*, 129604.
163. Lu, Y.; Zhang, H.; Wang, Y.; et al. Solar-Driven Interfacial Evaporation Accelerated Electrocatalytic Water Splitting on 2D Perovskite Oxide/MXene Heterostructure. *Adv. Funct. Mater.* **2023**, *33*, 2215061.
164. Wang, Y.; Lu, Q.; Ge, X.; et al. Molecular-Level Proton Acceptor Boosts Oxygen Evolution Catalysis to Enable Efficient Industrial-Scale Water Splitting. *Green Energy Environ.* **2024**, *9*, 344–355.
165. Liu, Q.; Shen, F.; Song, G.; et al. Tailoring Ion Ordering in Perovskite Oxide for High-Temperature Oxygen Evolution Reaction. *Angew. Chem. Int. Ed.* **2023**, *62*, e202307057.

166. Zhao, J.-W.; Yue, K.; Zhang, H.; et al. The Formation of Unsaturated IrO_x in $SrIrO_3$ by Cobalt-Doping for Acidic Oxygen Evolution Reaction. *Nat. Commun.* **2024**, *15*, 2928.
167. Xian, J.; Jiang, H.; Wu, Z.; et al. Microwave Shock Motivating the Sr Substitution of 2D Porous $GdFeO_3$ Perovskite for Highly Active Oxygen Evolution. *J. Energy Chem.* **2024**, *88*, 232–241.
168. Retuerto, M.; Pascual, L.; Calle-Vallejo, F.; et al. Na-Doped Ruthenium Perovskite Electrocatalysts with Improved Oxygen Evolution Activity and Durability in Acidic Media. *Nat. Commun.* **2019**, *10*, 2041.
169. Li, Q.; Wu, J.B.; Wu, T.; et al. Phase Engineering of Atomically Thin Perovskite Oxide for Highly Active Oxygen Evolution. *Adv. Funct. Mater.* **2021**, *31*, 2102002.
170. Kim, J.; Yin, X.; Tsao, K.-C.; et al. $Ca_2Mn_2O_5$ as Oxygen-Deficient Perovskite Electrocatalyst for Oxygen Evolution Reaction. *J. Am. Chem. Soc.* **2014**, *136*, 14646–14649.
171. Wang, J.; Gao, Y.; Chen, D.; et al. Water Splitting with an Enhanced Bifunctional Double Perovskite. *ACS Catal.* **2018**, *8*, 364–371.
172. Tang, L.; Chen, Z.; Zuo, F.; et al. Enhancing Perovskite Electrocatalysis through Synergistic Functionalization of B-site Cation for Efficient Water Splitting. *Chem. Eng. J.* **2020**, *401*, 126082.
173. Cui, X.; Li, W.; Liu, Y.; et al. Ultrafast Nanomanufacturing via High-Temperature Shock of $La_{0.6}Sr_{0.4}CoO_3$ Catalysts for Overall Water Splitting. *J. Mater. Sci. Technol.* **2024**, *191*, 1–7.
174. Zhai, T.; Wang, H.; Beaudoin, S.R.; et al. Perovskite Catalysts for Pure-Water-Fed Anion-Exchange-Membrane Electrolyzer Anodes: Co-Design of Electrically Conductive Nanoparticle Cores and Active Surfaces. *J. Am. Chem. Soc.* **2025**, *147*, 15448–15458.
175. You, M.; Gui, L.; Ma, X.; et al. Electronic Tuning of $SrIrO_3$ Perovskite Nanosheets by Sulfur Incorporation to Induce Highly Efficient and Long-Lasting Oxygen Evolution in Acidic Media. *Appl. Catal. B Environ.* **2021**, *298*, 120562.
176. You, M.; Xu, Y.; He, B.; et al. Realizing Robust and Efficient Acidic Oxygen Evolution by Electronic Modulation of 0D/2D CeO_2 Quantum Dots Decorated $SrIrO_3$ Nanosheets. *Appl. Catal. B Environ.* **2022**, *315*, 121579.
177. Zhao, L.; Tao, Z.; You, M.; et al. Partial Exsolution Enables Superior Bifunctionality of Ir@$SrIrO_3$ for Acidic Overall Water Splitting. *Adv. Sci.* **2024**, *11*, 2309750.
178. Sun, N.; Lai, Z.; Ding, W.; et al. Alkali Metals Activated High Entropy Double Perovskites for Boosted Hydrogen Evolution Reaction. *Adv. Sci.* **2024**, *11*, 2406453.
179. Zhao, B.; Zhang, L.; Zhen, D.; et al. A Tailored Double Perovskite Nanofiber Catalyst Enables Ultrafast Oxygen Evolution. *Nat. Commun.* **2017**, *8*, 14586.
180. Yagi, S.; Yamada, I.; Tsukasaki, H.; et al. Covalency-Reinforced Oxygen Evolution Reaction Catalyst. *Nat. Commun.* **2015**, *6*, 8249.
181. Gunkel, F.; Jin, L.; Mueller, D.N.; et al. Ordering and Phase Control in Epitaxial Double-Perovskite Catalysts for the Oxygen Evolution Reaction. *ACS Catal.* **2017**, *7*, 7029–7037.
182. Füngerlings, A.; Wohlgemuth, M.; Antipin, D.; et al. Crystal-Facet-Dependent Surface Transformation Dictates the Oxygen Evolution Reaction Activity in Lanthanum Nickelate. *Nat. Commun.* **2023**, *14*, 8284.
183. Fan, Y.; Ye, X.; Zhou, J.; et al. Combined *In Situ* X-Ray Spectroscopic and Theoretical Study on Trimetal Synergistic Enhancement of Water Oxidation. *Adv. Energy Mater.* **2025**, *15*, 2404599.
184. Weber, M.L.; Lole, G.; Kormanyos, A.; et al. Atomistic Insights into Activation and Degradation of $La_{0.6}Sr_{0.4}CoO_{3-\delta}$ Electrocatalysts under Oxygen Evolution Conditions. *J. Am. Chem. Soc.* **2022**, *144*, 17966–17979.
185. Sun, J.; Du, L.; Sun, B.; et al. A Bifunctional Perovskite Oxide Catalyst: The Triggered Oxygen Reduction/Evolution Electrocatalysis by Moderated Mn-Ni Co-Doping. *J. Energy Chem.* **2021**, *54*, 217–224.
186. Weng, Z.; Huang, H.; Li, X.; et al. Coordination Tailoring of Epitaxial Perovskite-Derived Iron Oxide Films for Efficient Water Oxidation Electrocatalysis. *ACS Catal.* **2023**, *13*, 2751–2760.
187. Yang, Y.; Chen, Y.; Yan, Y.; et al. Metal-Oxygen Octahedra Regulation of Iridium-Based Perovskites for Efficient and Durable Acidic Water Oxidation. *Adv. Funct. Mater.* **2025**, *35*, 2506467.
188. Zhu, Y.; Zhou, W.; Zhong, Y.; et al. A Perovskite Nanorod as Bifunctional Electrocatalyst for Overall Water Splitting. *Adv. Energy Mater.* **2017**, *7*, 1602122.
189. Oh, N.K.; Seo, J.; Lee, S.; et al. Highly Efficient and Robust Noble-Metal Free Bifunctional Water Electrolysis Catalyst Achieved via Complementary Charge Transfer. *Nat. Commun.* **2021**, *12*, 4606.
190. Hu, C.; Hong, J.; Huang, J.; et al. Surface Decoration Accelerates the Hydrogen Evolution Kinetics of a Perovskite Oxide in Alkaline Solution. *Energy Environ. Sci.* **2020**, *13*, 4249–4257.
191. Wang, L.; Stoerzinger, K.A.; Chang, L.; et al. Tuning Bifunctional Oxygen Electrocatalysts by Changing the A-Site Rare-Earth Element in Perovskite Nickelates. *Adv. Funct. Mater.* **2018**, *8*, 1803712.
192. Zhang, X.; Tang, C.; Yang, Y.; et al. Novel High-Entropy Air Electrodes Enhancing Electrochemical Performances of Reversible Protonic Ceramic Cells. *Adv. Funct. Mater.* **2025**, *35*, 2421083.

193. Nguyen, T.X.; Liao, Y.-C.; Lin, C.-C.; et al. Advanced High Entropy Perovskite Oxide Electrocatalyst for Oxygen Evolution Reaction. *Adv. Funct. Mater.* **2021**, *31*, 2101632.
194. Zhou, L.; Feng, D.; Li, Z.; et al. High-Spin-State Engineering in High-Entropy Perovskite Oxides via Crystal Phase Modulation for Paired Electrochemical Nitrate Reduction and Sulfur Ion Oxidation. *Adv. Funct. Mater.* **2025**, e14375. https://doi.org/10.1002/adfm.202514375
195. Satpathy, S.; Popović, Z.S.; Vukajlović, F.R. Electronic Structure of the Perovskite Oxides: $La_{1-x}Ca_xMnO_3$. *Phys. Rev. Lett.* **1996**, *76*, 960–963.
196. Zhang, Y.; Lu, H.; Li, X.; et al. Engineering the Oxygen Vacancies in Perovskite Oxides for Electricity Generation from Water Evaporation. *Adv. Mater.* **2025**, *38*, e14202.
197. Fang, G.; Liu, K.; Fan, M.; et al. Unveiling the Electron Configuration-Dependent Oxygen Evolution Activity of 2D Porous Sr-Substituted $LaFeO_3$ Perovskite through Microwave Shock. *Carbon Neutralization* **2023**, *2*, 709–720.
198. Jiang, H.; Li, J.; Xiao, Z.; et al. The Rapid Production of Multiple Transition Metal Carbides via Microwave Combustion Under Ambient Conditions. *Nanoscale* **2020**, *12*, 16245–16252.
199. Pan, Y.; Xu, X.; Zhong, Y.; et al. Direct Evidence of Boosted Oxygen Evolution Over Perovskite by Enhanced Lattice Oxygen Participation. *Nat. Commun.* **2020**, *11*, 2002.
200. Koo, B.; Kim, K.; Kim, J.K.; et al. Sr Segregation in Perovskite Oxides: Why It Happens and How It Exists. *Joule* **2018**, *2*, 1476–1499.
201. Ingavale, S.; Gopalakrishnan, M.; Enoch, C.M.; et al. Strategic Design and Insights into Lanthanum and Strontium Perovskite Oxides for Oxygen Reduction and Oxygen Evolution Reactions. *Small* **2024**, *20*, 2308443.
202. Qin, Y.; Fang, F.; Xie, Z.; et al. La,Al-Codoped $SrTiO_3$ as a Photocatalyst in Overall Water Splitting: Significant Surface Engineering Effects on Defect Engineering. *ACS Catal.* **2021**, *11*, 11429–11439.
203. Kim, B.-J.; Abbott, D.F.; Cheng, X.; et al. Unraveling Thermodynamics, Stability, and Oxygen Evolution Activity of Strontium Ruthenium Perovskite Oxide. *ACS Catal.* **2017**, *7*, 3245–3256.
204. Chen, C.F.; King, G.; Dickerson, R.M.; et al. Oxygen-Deficient $BaTiO_{3-x}$ Perovskite as an Efficient Bifunctional Oxygen Electrocatalyst. *Nano Energy* **2015**, *13*, 423–432.
205. Zhu, Y.; Liu, D.; Jing, H.; et al. Oxygen Activation on Ba-Containing Perovskite Materials. *Sci. Adv.* **2022**, *8*, eabn4072.
206. Porokhin, S.V.; Nikitina, V.A.; Aksyonov, D.A.; et al. Mixed-Cation Perovskite $La_{0.6}Ca_{0.4}Fe_{0.7}Ni_{0.3}O_{2.9}$ as a Stable and Efficient Catalyst for the Oxygen Evolution Reaction. *ACS Catal.* **2021**, *11*, 8338–8348.
207. Lee, J.; Kim, S.; Kim, Y.B.; et al. Multiple Variations in $LaCoO_3$ by Ca Substitution Activate Oxygen Evolution Reaction. *Chem. Eng. J.* **2025**, *520*, 165615.
208. Ma, X.; Wu, Z.; Tian, H.; et al. Durable Coaxial Fiber-Based Underwater Strain Sensor with Reversible Dry–Wet Transition. *InfoMat* **2025**, *7*, e70030.
209. Xu, X.; Pan, Y.; Ge, L.; et al. High-Performance Perovskite Composite Electrocatalysts Enabled by Controllable Interface Engineering. *Small* **2021**, *17*, 2101573.
210. Lei, J.; Wang, Z.; Zhang, Y.; et al. Understanding and Resolving the Heterogeneous Degradation of Anion Exchange Membrane Water Electrolysis for Large-Scale Hydrogen Production. *Carbon Neutrality* **2024**, *3*, 25.
211. Zhou, W.; Xu, F.; Tan, J.; et al. An Angstrom-Scale Protective Skin Grown *In Situ* on Perovskite Oxide to Enhance Stability in Water. *Angew. Chem. Int. Ed.* **2025**, *64*, e202417360.
212. Yu, J.; Liu, Q.; Wang, S.; et al. Spin-State Tuning in $PrFeO_{3-\delta}$ Perovskite for High-Temperature Oxygen Evolution Reaction. *J. Am. Chem. Soc.* **2025**, *147*, 33086–33096.
213. Wang, W.; Xu, M.; Xu, X.; et al. Perovskite Oxide Based Electrodes for High-Performance Photoelectrochemical Water Splitting. *Angew. Chem. Int. Ed.* **2020**, *59*, 136–152.
214. Yuan, R.-h.; He, Y.; He, W.; et al. Bifunctional Electrocatalytic Activity of $La_{0.8}Sr_{0.2}MnO_3$-Based Perovskite with the A-Site Deficiency for Oxygen Reduction and Evolution Reactions in Alkaline Media. *Appl. Energy* **2019**, *251*, 113406.
215. Qian, X.; He, J.; Mastronardo, E.; et al. Outstanding Properties and Performance of $CaTi_{0.5}Mn_{0.5}O_{3-\delta}$ for Solar-Driven Thermochemical Hydrogen Production. *Matter* **2021**, *4*, 688–708.
216. Zhao, Y.; Liu, T.; Shi, Q.; et al. Perovskite Oxides $La_{0.4}Sr_{0.6}Co_xMn_{1-x}O_3$ (x = 0, 0.2, 0.4) as an Effective Electrocatalyst for Lithium—Air Batteries. *Green Energy Environ.* **2018**, *3*, 78–85.
217. Sung, M.-C.; Lee, G.-H.; Kim, D.-W. Efficient Li_2O_2 Oxidation Kinetics of Perovskite-Type Lanthanum Chromium-Based Oxide by Promoter Interface Formation for Lithium-Oxygen Batteries. *Energy Storage Mater.* **2023**, *60*, 102829.